Faculté de génie

Département de génie chimique

Effet de la fluidodynamique des bulles et des gouttes sur la recombinaison du lithium et l'énergie consommée à l'intérieur d'une cellule électrolytique avec diaphragme utilisée pour la production de lithium

Effect of Bubbles and Liquid Drops Fluid Dynamics on the Lithium Recombination and Energy Consumed inside a Lithium Electrolytic Cell with Diaphragm

Thèse de doctorat
Spécialité : génie chimique

MSc. Juan Manuel Melendez

Jury : Prof. Martin Désilets (directeur)
Prof. Gaétan Lantagne (codirecteur)
Prof. Ryan Gosselin
Dr. Sandor Poncsak
Prof. Bernard Marcos

Sherbrooke (Québec) Canada   December 2022

Résumé

Le lithium métallique, qui est un métal critique et stratégique pour la production mondiale des dispositifs de stockage d'énergie, est principalement produit par électrolyse en sels fondus. Pour augmenter l'efficacité de ce procédé, il est de la plus haute importance d'empêcher la recombinaison du lithium pendant le processus afin d'éviter le gaspillage d'énergie. Afin d'optimiser les procédés d'électrolyse du lithium pour obtenir un métal de haute pureté avec le moins d'énergie possible, la recombinaison du lithium généré à la cathode avec le chlore généré à l'anode a été étudiée comme une conséquence de la dynamique des fluides des gouttes de lithium. Cette recherche se concentre sur le comportement des principales variables impliquées dans la réaction à l'intérieur d'une cellule expérimentale de production de Li du point de vue du transfert de masse, de l'électrochimie et de la dynamique des fluides. Des simulations ont été effectuées pour une électrolyse durant un intervalle de temps de 600 s en utilisant une approche prenant en compte la nature turbulente de l'écoulement avec la méthode k-ε pour résoudre l'écoulement biphasique couplé au processus d'électrolyse du lithium. Pour analyser l'influence de la dynamique du fluide près de la cathode en relation avec la quantité de lithium recombiné, deux configurations géométriques, utilisant un diaphragme non poreux, ont été évaluées, y compris l'incorporation d'un déflecteur au fond de la cellule. Le déflecteur a réduit la quantité de lithium recombiné de 7 %, et le diaphragme non poreux avec une inclinaison de 87° a réduit la masse totale de lithium recombiné de 77 %, bien qu'il ait augmenté la consommation d'énergie de 10 % par rapport au cas de base d'un diaphragme vertical. Pour réduire la quantité d'énergie consommée, et la masse recombinée de lithium, l'utilisation d'un diaphragme rainuré et d'électrodes rotatives a aussi été étudiée. Le diaphragme avec des rainures a été évalué avec différents angles d'inclinaison. Dans les cas d'électrodes rotatives, cinq vitesses angulaires sans diaphragme ont été analysées. La résistance du film anodique a également été ajoutée au modèle numérique par le biais d'une équation représentant la fraction volumique du gaz en fonction du temps. Le diaphragme vertical avec rainures permet de réduire de 26,7 % la consommation d'énergie par rapport à la conception verticale non poreuse, mais augmente de quatre fois la quantité de lithium recombiné dans le processus. Pour diminuer cette recombinaison, le diaphragme à rainures a été incliné vers l'anode. Un angle vertical de 85° permet de réduire l'énergie consommée de 23,5 % avec approximativement la même masse de lithium recombiné par rapport à la conception verticale non poreuse. L'utilisation d'une cathode rotative à une vitesse angulaire de 0,25 rad/s entraîne une diminution de 40 % de la consommation d'énergie ainsi qu'une diminution de 87,4 % de la reconversion du lithium métallique, par rapport du diaphragme vertical non poreux.

Mots clés: dynamique des fluides avec bulles et gouttelettes, processus électrochimique, dynamique des fluides sur la surface de la cathode, lithium recombiné, conception de diaphragme non poreux et rainuré.

Abstract

Metallic lithium is a critical and strategic metal for the world's production of energy storage devices, and it is produced mainly from molten salt electrolysis processes. To increase the efficiency of such processes, it is of utmost importance to prevent lithium recombination to avoid energy waste. To optimize the lithium electrolytic processes and obtain a high purity metal with the least amount of energy, the recombination of lithium has been studied as a consequence of the lithium drops fluid dynamics. This research studies the behavior of the main variables involved in the reaction inside a Li-production experimental cell from the mass transfer, electrochemical and fluid dynamics standpoints. The behavior of an experimental electrochemical cell was simulated for 600 s time period using a turbulent (k-ε) approach to solve the two-phase flow. In order to analyze the influence of the cathode fluid dynamics in relation with the amount of recombined lithium, two configurations of the non-porous diaphragm were evaluated, including the incorporation of a baffle at the bottom of the cell. The baffle reduced the amount of recombined lithium by 7 %, and the non-porous diaphragm with an inclination of 87° reduced the total recombined mass by 77 %, although it increased the energy consumption by 10 % with respect to the base case of a vertical diaphragm. A grooved diaphragm and rotating electrodes were also used to reduce the energy consumed. The inclination angle of the diaphragm with grooves has been evaluated for three different configurations, while the rotating electrode condition was studied for five different angular velocities without a diaphragm. The anodic film resistance was also added in the numerical model through an empirical equation of gas volume fractions as a function of the time. It allowed for a better combination between fluid dynamics and the electrochemical field. The vertical diaphragm with grooves produced a reduction of 26.7 % in energy consumption in comparison with the vertical non-porous design but increased by four times the amount of recombined lithium in the process. The grooved diaphragm was inclined toward the anode to decrease the lithium recombination. A vertical angle of 85° also helped to reduce the energy consumed by 23.5 % with approximately the same recombined lithium mass compared to the vertical non-porous design. Using a rotating cathode with an angular velocity of 0.25 rad/s resulted in a 40 % reduction in energy consumption; in addition, it decreased by 87.4 % the metallic Li reconversion in comparison with the vertical non-porous diaphragm design.

Keywords: Bubble fluid dynamic, electrochemical process, fluid dynamics on the cathode surface, lithium liquid recombination, diaphragm non-porous and grooved design.

Acknowledgments

Table of Contents

List of Figures

List of Tables

1 Introduction.

1.1 Importance of the research subject.

According to the latest Conference of the Parties (COP26), the world needs to rapidly replace fossil fuels with clean energy to reduce the amount of CO_2 in the atmosphere and thus reduce global warming [1]. One of the principal sources of CO_2 emissions are internal combustion engines (ICE) vehicles, which are being replaced by electric vehicles (EVs). However, the substitution has been difficult due to the limitations and problems caused by the storage of electric energy. On the one hand, the battery with the highest storage capacity is based on the lithium-ion technology. On the other hand, this technology is dangerous because of the use of flammable electrolyte apart from lithium ion phosphate batteries which are inherently safe [2]. A solution to this problem is to develop the solid stated batteries (SSBs), where the anode is composed of solid metallic lithium. Furthermore, the SSBs can achieve a volumetric energy density up to 70 % greater than today's lithium-ion batteries that use conventional graphite anodes, making them the ideal batteries for future EVs [2]–[4]. One advantage of SSBs is that they do not require expensive cooling systems due to the absence of a flammable electrolyte. They have displayed better functionality at higher temperatures due to the increased conductivity of the electrolyte. Placke et al. (2017) [5] have predicted that the current lithium-ion batteries could reach a maximum energy density of 300 Wh/kg after 2025, while metallic lithium SSBs would reach a maximum of 480 Wh/kg. In 2021, St-Onge *et al*. [6] developed an improved lithium SSBs, proving that batteries of the same size could contain much more energy in the future.

From the above considerations, it is important to produce solid lithium with environment-friendly processes, where energetic optimization will be a principal factor. Developing new techniques and designs of electrolytic cells for lithium production can achieve that energy optimization. Amouzegar *et al*. (1996) [7] studied the production of metallic lithium from molten salts using an experimental electrolytic cell (EEC), based on the following electrochemical reactions:

$$\text{Anode (Oxidation): } 2Cl^- \rightleftharpoons Cl_{2\,(g)} + 2e^-$$

$$\text{Cathode (Reduction): } 2Li^+ + 2e^- \rightleftharpoons 2Li_{(l)}$$

$$\text{Total Reaction: } 2Li^+ + 2Cl^- \rightleftharpoons 2Li_{(l)} + Cl_{2\,(g)}$$
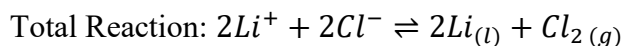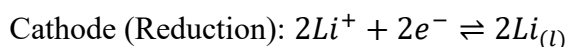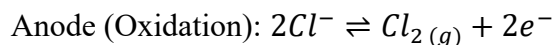
Hydro-Quebec developed the design of the EEC (see Fig. 1.1) in the form of a batch reactor. At the top of the cell, nitrogen is added as an inert gas used to remove chlorine gas from inside the cell. Oliaii *et al*. (2017-18) and Litrico *et al*. (2018) [8]–[10] partially simulated the fluid dynamic coupled to the electrochemical field in that EEC. They all have taken into account the detrimental effect of chlorine bubble production that brings an additional resistance to the mass and charge transfer taking place in the electrolyte solution and limiting the electrochemical reactions on the anode surface.
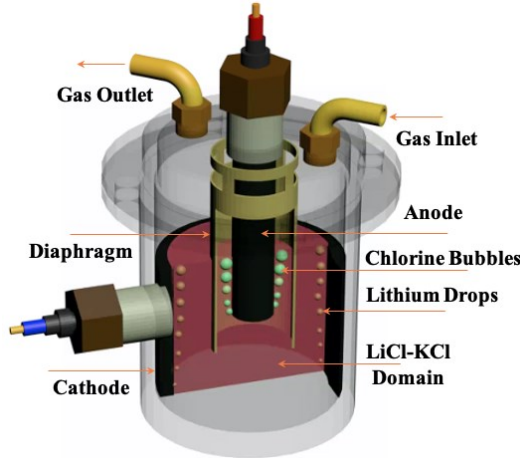
Fig. 1.1 Experimental lithium electrolytic cell.

Optimizing the electrolytic cell for lithium production using molten salts involves finding a solution to chlorine bubble production at the anode surface. These bubbles create a resistance to mass transfer, resulting in high energy consumption [11]–[14]. Previous studies have shown the importance to simulate the effect of mass transfer across the anodic boundary layer, where bubbles of Cl_2 are produced, which must be improved to optimize lithium production. This research work has added the anodic film resistance using an anodic boundary layer to improve the model. It also considers the production of liquid lithium droplets at the cathode surface. The main differences between previous research works with this project are underlined in Table 1.1.

Table 1.1. Literature review comparison.

Literature Review	Electrolysis and Phases	Diaphragm	Anode Surface Phenomena			Electrolyte Solution			Cathode Surface Phenomena		
			ECH	BFor	VEL	ABL	MAT	MOT	ECH	DFor	VEL
Oliaii *et al.* (2017) [8]	Li - One	Non porous	Tafel	VOC	Flat Plate	BRC	NPE	NS k-ε	LBV	No	No
Oliaii *et al.* (2018) [9]	Li - Two	Porous	Tafel	VOC	FAL	BRC	NPE	NS k-ε	LBV	No	No
Litrico *et al.* (2018) [10]	Li - Two	No	Tafel	VOC	FAL	No	NPE	NS k-ε	LBV	No	No
Zhao *et al.* (2020) [15]	Li - Two	No	PCD	CMB	FAL	No	NPE	NS k-ε	PCD	No	No
El-Askary *et al.* (2015) [16]	H2O - Two	No	BV	HBM	FAL	MLB	HBM	NS k-ε	BV	No	No
Riegel *et al.* (1998) [17]	H2O - Two	No	BV	HBM	EMC	No	HBM	NS k-ε	BV	No	No
Takamure *et al.* (2020) [18]	H2O - Two	No	PCD	FAL	EMC	EMC	HBM	NS k-ε	PCD	No	No
Pan *et al.* (2020) [19]	H2O -Air	No	No	No	No	NS k-ε Fluid Dynamics			No	No	No
This Project	Li - Two	Non porous	Tafel	CMB	CMB	CMB	NPE	NS k-ε	LBV	LMB	LMB

ECH : Electrochemical Field; **BFor - DFor** : Bubble and Drop Formation; **VEL** : Flow Velocity; **ABL** : Anode Boundary Layer; **MAT - MOT** : Mass and Momentum Transfer; **VOC** : Vogt Correlation; **BRC** : Bruggeman Correlation; **NPE** : Eq. Nernst-Planck; **NS k-ε** : Turbulent k-ε Navier-Stokes Equation; **BV - LBV** : Butler-Volmer and Linearized Equation; **FAL** : Faraday Law; **PCD** : Primary Current Distribution; **HBM - CMB - LMB** : Mass Balance of Water, Chlorine and Lithium; **MLB** : Mixing Length Boundary; **EMC** : Empirical Correlation.

1.2 General objective.

This project aims to optimize lithium production, analyzing the impact of cell design on lithium mass recombined and energy costs through the chlorine bubbles and lithium liquid drops fluid dynamics. This analysis relies on the intimate coupling of the conservation equations (momentum, mass, and charges) representing the most important phenomena occurring inside the molten salt lithium.

1.2.1 Primary objective.

The primary objective is to develop a mathematical model representing the bubbles and lithium liquid drop production in the electrolytic solution, coupling the mass, energy, and momentum transfer. Also, the mathematical model includes bubbles generation through a constant density of nucleation sites. The force balance (buoyancy, interfacial and drag forces) on the bubble defines the detachment process. The bubbles play an essential role in the mass transfer inside the electrolytic solution. The mass conservation equation considers the effect of bubbles' transport phenomena inside the solution including its effect on the electrical resistance, creating a strong coupling between the Faraday's law and the Butler-Volmer equation. Furthermore, after the detachment stage, the bubbles induce a fluid movement in the electrolytic solution causing natural convection that affects all other transfer processes. The momentum transfer equation includes all those processes of transfer. Fig. 1.2 illustrates the main physical and chemical phenomena (bubbles, fluid dynamics, electrochemical reactions, and mass transfer) developed in the mathematical model.
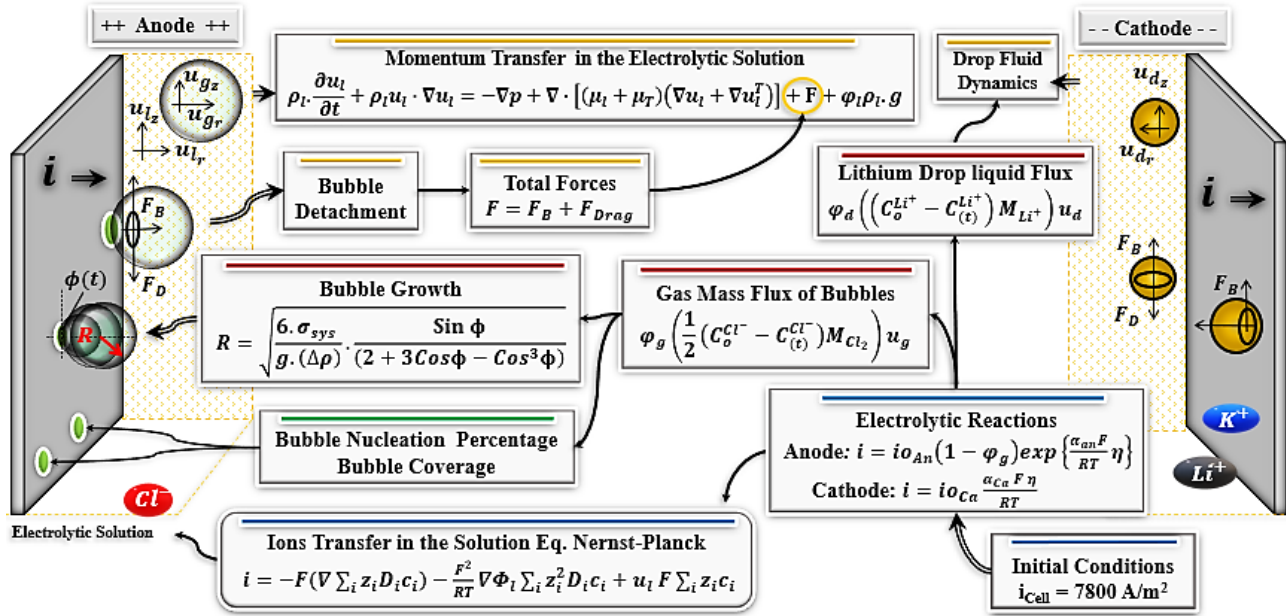
Fig. 1.2 Diagram of the main phenomena considered in the mathematical model of this project.

1.2.2 Secondary objective.

The validation to this research project is shown in Fig. 1.3. The validation is using data from different applications such as water and magnesium electrolysis. We use the dimensionless parameters of fluid dynamics such as the drag coefficient for the validation.
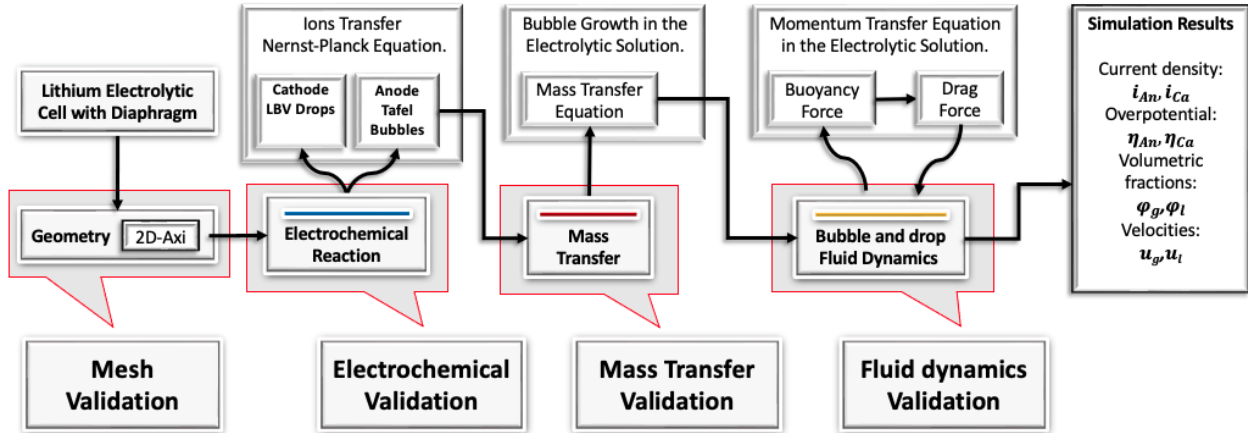
Fig. 1.3 Diagram representing the validation of the main phenomena.

After having defined the mathematical model that represents the effect of each bubble stage on the transfer of mass, energy and momentum in an electrolytic solution, the following validation steps are taken:

1. To validate the triangular mesh of the numerical model, we used the experimental and simulation data taken from the literature review.
2. The optimal number of nodes is established for this project using the software Comsol Multiphysics®.

1.2.3 Tertiary objective.

Once the numerical model is validated, the next step is to evaluate the metal production process to seek the parameters that affect the energy consumption and metal productivity using different designs (diaphragm, baffles) and operation conditions (rotating electrodes) in electrolytic cells.

1.2.3.1 Non-porous diaphragm.

For this part, we propose two new configurations of the non-porous diaphragm and evaluate the influence of the cathode fluid dynamics on the amount of recombined lithium and energy consumption:

1) a conical configuration with a bottom diaphragm radius (R_{DB}) of 39 mm designated as the configuration > 90°, and

2) a conical configuration with a bottom diaphragm with R_{DB} = 29 mm, designated as the configuration < 90° (see Fig. 1.4).

To optimize the fluid dynamics of the cathode domain, we added a small baffle at the bottom of the electrolytic cell at a fixed position. For the non-porous diaphragm, we proposed the following steps:

1. Check the turbulence regime by means of the Grashof number.
2. To analyze the relation between gas and liquid velocity behavior with time.
3. Describe the change of potential as a function of volume fraction.
4. Describe the behavior of electrolyte velocity in the cathode domain.
5. Determine the total mass of Li produced and the mass of recombined lithium.
6. Describe the effects of electrolyte velocity in function of recombined Li mass.
7. Compute the total energy consumed in the process.
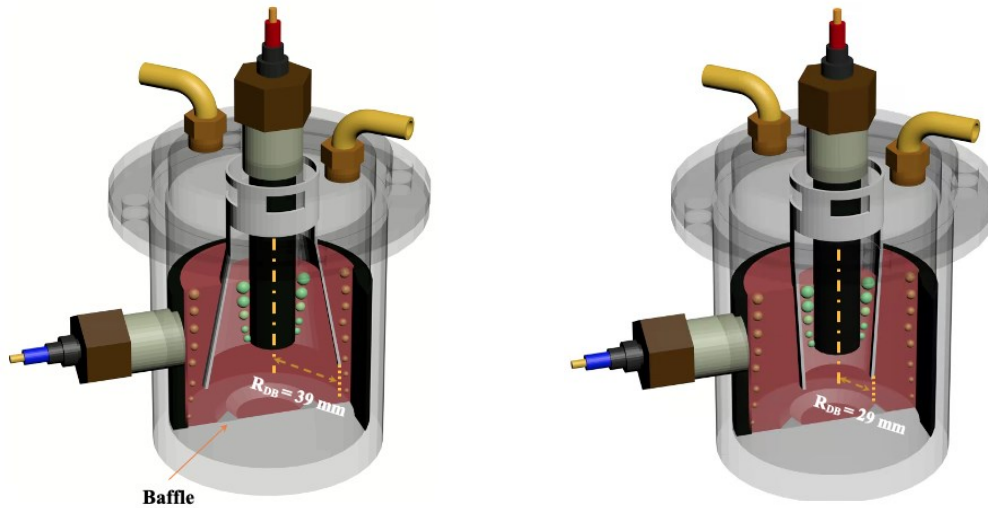
Fig. 1.4 The diaphragm configuration for the two different bottom diaphragm radii.

1.2.3.2 The grooved diaphragm and rotating electrodes.

In this second section, we added the anodic boundary layer to study the film resistance on the anode surface, and we looked at the impact of the rotating movement of each electrode. Fig. 1.5 shows the grooved diaphragm and the rotating electrode designs in the lithium electrolytic cell. The grooves are evenly spaced and located at the bottom section of the diaphragm. On one hand, it permitted the separation of the anolyte and catholyte fluid dynamics. On the other side, it helped to increase mass transport at the bottom of the diaphragm and thus reduces the energy consumption. We removed the diaphragm of the geometry for the rotating electrode simulations, to reduce the resistance against the current transfer in the electrolyte, and to analyse how the lithium production could be affected in a process where a continuous inlet with an angular flow of the electrolyte solution is injected. In this section, we proposed the following steps:

For grooved diaphragm:

1. Determine the boundary layer thickness and the anodic film overpotential in function of time.
2. Determine the average velocity in the cathode and anode domains.
3. Determine the lithium and chlorine mass close to the vertical diaphragm surface.
4. Compare the current density magnitude on the anode surface using a vertical non-porous, to the current density obtained on a grooved diaphragm.
5. Compute the potential and overpotentials along the anode height for a vertical non-porous, and for a grooved diaphragm.
6. Determine the recombined lithium mass for the two configurations: the vertical non-porous and grooved diaphragm.
7. Calculate the energy consumed using a vertical non-porous, and grooved diaphragm.
8. Compute the mass of recombined lithium in the anode domain for the following bottom diaphragm radius of $R_{DB} = 25$ and 29 mm.
9. Determine the energy consumed for the same bottom diaphragm radius of $R_{DB} = 25$ and 29 mm.

For rotating electrodes:

10. Calculate the cell potential and film overpotential for different anodic angular velocities.
11. Determine the recombined lithium mass for different electrode rotation speeds.
12. Compute the energy consumed for different electrode rotation speeds.
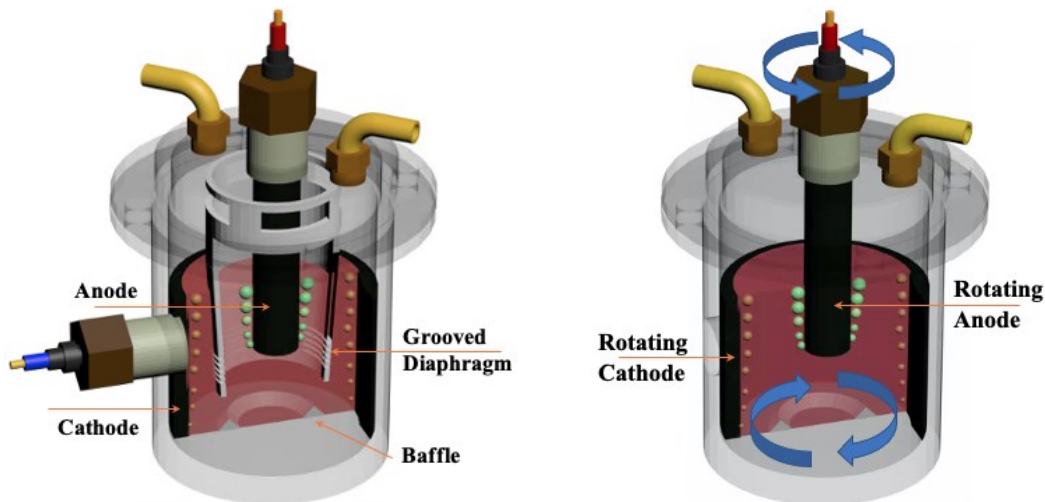
Fig. 1.5 The grooved diaphragm (left) and rotating electrodes (right) configurations.

1.3 The research work description.

Transient simulations of the lithium electrolysis cell have been solved for a time period of 600 s, a period long enough to reach a pseudo steady state regime. For the initial parameters

of this simulation, we use values published by Oliaii *et al.* (2017) and by Zhao *et al.* (2020) [8]-[15]. Lithium electrolysis simulations were conducted with Comsol Multiphysics® using the Eulerian Bubbly Flow Model to represent the momentum transfer produced by the bubbles inside the electrolytic solution at the anode [20]. The Eulerian Mixture Model was used to predict the fluid dynamics of lithium liquid drops produced at the cathode surface [21]. The Electrochemical Model based on the Tertiary Current Distribution (TCD) has been used to simulate the electrochemical reactions at the surface of the electrodes and the ion mass transfer inside the electrolyte [22]. The geometry of the computation domain of lithium electrolytic cell is taken from Oliaii *et al.* (2017) [8], as shown in Fig. 1.6.

According to Lovering (1982), it is important to take into account the presence of the diaphragm, which is used to separate the chlorine gas from the liquid lithium and to prevent the recombination of these products, such as is shown in Fig. 1.6 [23]. In this simulation, it takes the form of a non-porous smooth flat surface that is located in the anode-cathode gap and extends below the bottom of the anode.
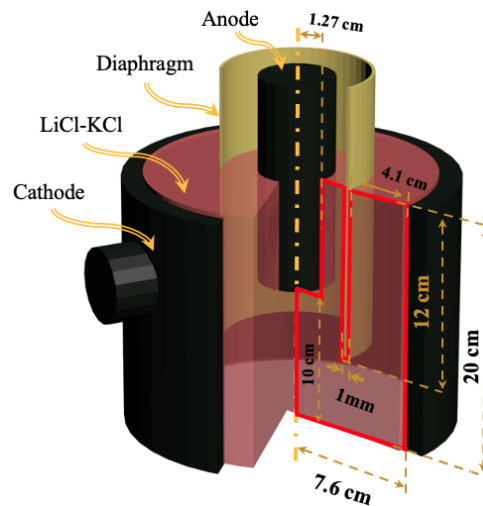
Fig. 1.6 Geometry of the computational domain (red line).

1.4 Hypothesis.

The assumptions made in this project allow us to develop the numerical algorithm and analyse the different fields affected by the evolution of the bubbles and liquid drops inside the electrolytic cell. All assumptions regarding mass, energy, and momentum transfer are presented in the following part.

1.4.1 General hypothesis.

There is a direct relation between the formation and displacement of the chlorine bubbles and the lithium drops in the electrolytic solution that affects the lithium production and the energy consumed in the process.

1.4.2 Specific hypotheses.

1.4.2.1 Mass transfer.

- The bubble formation starts when the electrolytic solution is saturated with gas; hence, there is no gas diffusion process inside the electrolytic solution for all-time simulation.
- We considered the bubble and drop shapes as a trunked sphere on the surfaces of the electrodes.
- The size of each bubble and liquid drop is defined through a balance of external force applied on their surface.
- The mass transfer on the free surface of the electrolytic solution is neglected.

1.4.2.2 Momentum transfer.

- The pressure in the system is considered constant at 1 atm.
- The chlorine gas density is estimated using ideal gas behavior.
- The momentum conservation equation describes the movement in the electrolytic solution.
- The boundary layer defines the bubble velocity in the electrolytic solution.
- We neglected the Lorentz force produced by an electromagnetic field and its effect on the flow.
- The gas movement into the bubble is neglected.
- The hydrodynamic properties of the LiCl-KCl molten salt solution are close to water properties.

1.4.2.3 Heat transfer.

- Temperature is constant (723 K) in the electrolytic solution.

1.4.2.4 Electrolytic process.

- The bubbles are electrical insulators.
- The electrical conductivity changes with the ion concentration in the electrolytic solution.
- Using the linearized Butler-Volmer equation, we defined the current density on the cathode as a linear function with the overpotential.

2 State of the art.

To understand the originality and the scope of each of the objectives of this research project, it is necessary to show in the literature review the following information:

- The different stages of bubble formation in the electrolytic solution.
- The main relation between all phenomena developed in the electrolyte.
- The numerical algorithm with bubble formation, momentum, and mass transfer.

2.1 The stages of bubble formation.

The bubble formed in a lithium electrolytic cell is a way to validate the fluid dynamics developed in the cell. We took the different stages of bubble formation from the theories developed according to the phases of the system, and according to the external forces acting on the bubble surface.

In this research project, nucleation stage in its initial phase is represented by a percentage of chlorine gas on the anode surface. Subsequently, this gas percentage will be calculated by the classical nucleation theory (CNT).

After the nucleation of the bubble, its growth is a function of the contact angle, which changes in function of time. For this stage, in this work, the bubble volume was simulated by using a constant contact angle reported by previous works [24]. The growth and displacement of the bubble in the electrolyte solution has been simulated considering that the electrolyte is saturated with chlorine gas. This means that there is no mass transfer between the bubble and the electrolyte solution. Then, a mass transfer model analysed in this literature review will be shown to simulate its effect on the energy consumption.

In this simulation, the effect of bubble breakup is initially neglected. However, the model for that bubble stage is developed in this literature review, which it will be added later to analyse its effect on the amount of recombined lithium.

2.1.1 Bubble nucleation.

To determine the nucleation rate of bubbles in a system, it is necessary to know whether it is a homogeneous nucleation (in the bulk of the solution) or a heterogeneous nucleation (on a solid surface). Subsequently, the free energy of Gibbs for the formation of all the nuclei could be calculated. We develop this section in four parts, which are as follows:

- The theory that allows us to calculate the energy required for the formation of all the bubble nuclei.
- The thermodynamic equations defining heterogeneous nucleation on the electrode surface.

- The equation defining the rate of nucleation as a function of time-dependent variables.
- The numerical method that allows us to locate the position of each nucleus on the electrode surface.

The nucleation of bubbles on the anodic surface of a lithium electrolytic cell has not been developed and validated in previous published work. However, the thermodynamic equations that define the nucleation process are the same for the formation of crystalline nuclei, condensed micro-drops or micro-bubbles formed in a solution. In this section of the literature review, we show the nucleation models published by principal researchers in the field, regardless of whether they have worked with a crystalline nucleus, condensed micro-drops or vapour micro-bubble.

The nuclei or clusters are defined as the minimum number of molecules to form a bubble, drop, crystal or particle, and the nucleation is the formation process of all nuclei. Winter *et al*. (2010) [25] remarked that in the classical nucleation theory, the formation of a (spherical) nucleation seed in the bulk can be explained with two competing factors: a volumetric term, which seeks to expand the seed, and an opposing surface term, as shown in the following equation:

$$E = -Volume \times \Delta\mu + Surface \times \sigma \qquad\qquad 2.1.1$$

Where E is the free energy of nucleus formation, σ the surface tension, and $\Delta\mu$ is the potential chemical difference.

According with Kalikmanov, (2013) [26] the Nucleation refers to the situation when a system (parent phase) is put into a metastable state. Experimentally, it can be achieved in a number of ways, for example by forming crystalline nuclei by evaporating its parent phase. In this work, nucleation and related phenomena will refer to the liquid-gas transition. It is important to show the main nucleation approach that will be used in this research project.

There are several nucleation theories; they depend on the assumptions established to develop the equation representing the phenomenon. The most important ones related to this project are described as follows:

2.1.1.1   Classical nucleation theory (CNT).

Horsch *et al*., 2008 [27] consider this theory more precise and accurate at low temperature, but it has different variations and can also be used at high temperature conditions. The tool most often used in the nucleation studies is the phenomenological CNT, formulated in the first half of the twentieth century by Volmer in 1936. Its cornerstone is the capillarity approximation considering a condensation cluster, however small, as a macroscopic bubble of the evaporated phase. The core assumptions of the classical approach are: (i) low enough temperature below critical temperature (Tc) and (ii) low enough supersaturation of a metastable phase. Kashchiev (1982) [28] considers a general form of the Gibbs free energy of (n) cluster formation:

$$\Delta G^{hom}(n, \Delta\mu) = -n\Delta\mu + F_s(n, \Delta\mu) \qquad\qquad 2.1.2$$

Where $\Delta\mu$ is the potential chemical difference. Central to nucleation theory is the expression for the free energy of nucleus formation $\Delta G^{hom}(n, \Delta\mu)$ and its determination is the core step for the construction of any nucleation-condensation model. The macroscopic change of free energy associated with the formation of a nucleus consisting of i atom or monomers (the formation energy for brevity) always contains the volume term and the surface energy term $F_s(n, \Delta\mu)$. In homogeneous nucleation theory, the $\Delta G^{hom}(n, \Delta\mu)$ can be written down as:

$$\Delta G^{hom}(n, \Delta\mu) = F_s(n, \Delta\mu) - \left[\frac{\Delta\mu}{k_B T}\right] i = F_s(n, \Delta\mu) - Ln\,(\xi + 1)\,i \qquad\qquad 2.1.3$$

$$\xi = \frac{n_1}{n_{1e} - 1},\, n_{1e} = \frac{\theta_{1e}}{\Omega},\, \theta_{1e} = exp\left[\frac{-2T_c}{T}\right] \qquad\qquad 2.1.4$$

Where k_B is the Boltzmann constant, ξ the supersaturation factor, n_1 metastable phase concentration, n_{1e} the equilibrium concentration, θ_{1e} the equilibrium densities, Ω the elementary volume and T, T_c the system temperature and critical temperature respectively. The entire system is isothermal, with all nuclei having the same temperature T which is equal to the gas temperature. This is usually ensured by the presence of a passive gas or the thermostatic effect of the substrate, which is kept constant during the entire growth process.

2.1.1.2 The heterogeneous nucleation of bubbles on a solid surface.

According to Vehkamäki (2006) [29], in the classical nucleation theory, the cluster is modelled as a semi-sphere, and the interaction between the cluster and the underlying surface is described with a contact angle (ϑ), an angle between the underlying surface and the tangent of the cluster surface at the point where these surfaces meet, see Fig. 2.1
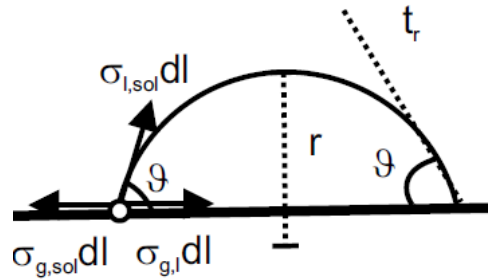
Fig. 2.1 A cluster on a planar particle. The tangent of the cluster surface is marked with t_r, r is the cluster radius, and ϑ is the contact angle. Forces $\sigma_{l,sol}dl, \sigma_{g,l}dl$, and $\sigma_{g,sol}dl$ arising from the surface tension between solid sol, liquid l and vapour g acting on a surface line element of length dl are also shown.

The contact angle is related to the surface tension between liquid and solid, $\sigma_{l,sol}$, vapour and liquid, $\sigma_{g,l}$, and vapour and solid $\sigma_{g,sol}$, according to *Young's equation*:

$$Cos\ \vartheta = \frac{\sigma_{g,sol} - \sigma_{l,sol}}{\sigma_{g,l}} \qquad 2.1.5$$

Also, Vehkamäki has considered that the thermodynamics and kinetics of heterogeneous nucleation is the same as for homogeneous nucleation, with the only differences in the surface energy and geometric terms.

$$\Delta G^{het} = f_\varphi \Delta G^{hom} = f_\varphi \frac{4\pi (r^*)^2 \sigma_{g,l}}{3} \qquad 2.1.6$$

$$r^* = \frac{2\sigma_{g,l}}{P_B - P_{ext}} \qquad 2.1.7$$

Where ΔG^{hom} and ΔG^{het} are the free energy of formation of the homogeneous and heterogeneous nuclei respectively, r^* is the critical radius of cluster in the same conditions (the critical radius is the minimum radius that a nucleus or cluster can have, after reaching the number of atoms necessary for its formation), P_B is the internal pression of the bubble, P_{ext} is the hydrostatic and atmospheric pression at the place where the bubble is formed. Another radius that we need to know in the CNT is the bubble radius in function of time. That radius is defined in the next equation:

$$R_B = 2\beta (D\ t)^{1/2} \qquad 2.1.8$$

Where R_B is the bubble radius, D diffusivity, t time, and β the saturation coefficient. the geometric factor f_φ can be written in terms of the ratio of radii $X = r^*/R_B$ and cosine of the contact angle as seen in Eq. 2.1.9:

$$f_\varphi = \frac{1}{2}\left\{ 1 + \left(\frac{1 - X Cos\ \vartheta}{d_x}\right) + X^3\left[1 - 3\left(\frac{X - Cos\ \vartheta}{d_x}\right) + \left(\frac{X - Cos\ \vartheta}{d_x}\right)^3\right] \right.$$
$$\left. + 3Cos\ \vartheta X^2 \left(\frac{X - Cos\ \vartheta}{d_x} - 1\right)\right\} \qquad 2.1.9$$

For all values of X and $Cos\ \vartheta$, the geometric factor is lower than one, $0 < f_\varphi \leq 1$.

2.1.1.3   Bubble nucleation rate.

The heterogeneous nucleation of bubbles depends on the dynamics of the electrolysis process, and it is influenced by the electrolytic reaction and by the mass transfer, which can be the limiting step. For this reason, it is essential to understand the different theories and research on this subject. Vehkamäki (2006) [29] has developed an equation to calculate the nucleation rate that can be written as:

$$J_{het} = \frac{\left|\lambda_l^{het}\right|}{2\pi k_B T} F_{het}^e exp\left(\frac{\Delta G^{het}}{k_B T}\right) \frac{1}{\sqrt{\left|det\left(\frac{W_{het}^*}{2\pi k_B T}\right)\right|}} \qquad 2.1.10$$

The components of the matrix W_{het}^* are the second derivatives of the heterogeneous free energy of formation with respect to the numbers of molecules in the cluster, and λ_l^{het} is the negative eigenvalue of product matrix $(R_{het}^*)(W_{het}^*)$. R_{het}^* is the heterogeneous growth matrix,

whose components give the rate at which monomers of different types collide with the critical cluster. F_{het}^e is the normalization factor in the cluster size distribution. In the heterogeneous case, the cluster distribution can be approximated by the sum of monomer concentrations on the surfaces of pre-existing particles in the equilibrium vapour ($C_{i,mon}^{e,het}$).

$$F_{het}^e = \sum_i C_{i,mon}^{e,het} \quad and \quad C_{i,mon}^{e,het} = x_{i,g} \frac{2r_x}{v_x} \qquad 2.1.11$$

Where $x_{i,g}$ represents the monomer molar fraction in the gas, r_x is the radius of the monomer cluster, and v_x is the partial gas volume.

2.1.1.4   Direct computer simulations to represent a bubble set.

For the nucleus distribution on the anode surface, we will use the Monter Carlos Method (MCM). Kalikmanov (2013) [26] has proposed a simulation of nucleation on a molecular level by Monte Carlos method, a technique that complements theoretical and experimental studies and as such may be regarded as a virtual (computer) experiment. Vehkamäki (2006) [29] suggests that the simulation methods are roughly divided into three categories: Density method (MD), MCM, and search for the minimum energy configurations. Also, there exist some variations of the MCM used in nucleation studies. They are based on calculating statistical averages of cluster properties in different sets, depending on which control parameters (temperature, pressure, total energy, volume, chemical potential) are kept constant in the studied system.

The MCM is based on the random generation of atom coordinates in a simulation box. Kalikmanov (2013) [26] considers that the MCM is sampling the configurational space of the system. This method considers a thermodynamic statistical ensemble (Number particle-Volume-Temperature or NVT ensemble) that represents the possible states of a mechanical system in thermal equilibrium with an electrolytic solution at a fixed temperature. The system can exchange only energy with the solution, in consequence the states of the system will differ in total energy to each time instant.Vehkamäki (2006) [29] presented the principal equations and procedures to simulate homogenous nuclei. The Kalikmanov (2013) [26] procedure and equations were took to represent the heterogeneous nucleation locations, where the potential energy $U(r^N)$ of a given configuration $r^N \equiv (r^1, \ldots, r^N)$ are developed. The average value of an arbitrary function of coordinates $X(r^N)$ is given by the integral

$$\langle X(r^N) \rangle = \int X(r^N) w(r^N) dr^N \qquad 2.1.12$$

Where $w(r^N)$ is the Boltzmann probability density function of a given state r^N:

$$w(r^N) = \frac{1}{Q_N} e^{-\beta . U(r^N)} \qquad 2.1.13$$

$$Q_N = \int e^{-\beta . U(r^N)} dr^N \qquad 2.1.14$$

Where β is the term $\frac{1}{k_B T}$ and the function $w(r^N)$ is positive and normalised to unity $\int w(r^N) dr^N = 1$. From the standpoint of probability theory, Eq. 2.1.12 defines the mathematical expectation of $X(r^N)$. To have an idea of the mathematical methods proposed by Kalikmanov (2013) [26], imagine that we have a digital camera that can instantaneously take photos of the system, so that we can use this camera to scan and memorize the $3D$ coordinates of all N molecules in the volume V. This can be repeated M times per second. Then, the computer memory will contain the set of coordinates $(r^N)_1, (r^N)_2, \ldots, (r^N)_M$, where M is a number of configurations. The average observed value of X

$$AVRG(X) = \frac{1}{M} \sum_{k=1}^{M} X[(r^N)_k] \qquad 2.1.15$$

Gives an estimate of the *true (exact)* value $\langle X(r^N) \rangle$ given by Eq. 2.1.12, which cannot be calculated. The mean-square deviation

$$\sigma^2 = \frac{1}{M} \sum_{k=1}^{M} X^2[(r^N)_k] - [AVRG(X)]^2 \qquad 2.1.16$$

Characterizes the accuracy of our statistical averaging. In MCM, the integral (2.1.12) is approximated by Kalikmanov (2013).

$$\langle X(r^N) \rangle = AVRG(X) \left[1 \pm \frac{\sigma}{\sqrt{M}} \right] \qquad 2.1.17$$

Note that σ becomes independent of the number of observations for large M, implying that the error of approximation (Eq. 2.1.17) is inversely proportional to the square root of the number of observations, which is typical for mathematical statistics.

2.1.2 Bubble growth.

Cluster growth theory in this project starts from the critical nucleation size. Vehkamäki (2006) [29] presented a numerical model using a growth coefficient that is function of the equilibrium concentration and the nucleus geometry. This method was also used by Van der Linde *et al*. (2017) [30]. In this research project, it is important to define the main equations used to represent bubble growth in the electrolytic solution, and to analyse the change of the principal variables such as the over potential or the current density.

2.1.2.1 Vehkamäki growth coefficients.

Vehkamäki (2006) [29] assumes that the growth of the micro-drop is occurring by vapour molecules hitting with its surface. Then, the growth coefficients β_i^{het} (units/s) (components of matrix R_{het}^*) are given by the monomer or cluster flux per unit area, and are represented by the Eq. 2.1.18

$$\beta_i^{het} = C_{i,mon}^{e,het} \delta_i L^* v_{i,diff} \exp\left(\frac{-\Delta e_{i,diff}}{k T_0}\right) \qquad 2.1.18$$

Where δ_i is the average jump distance of adsorbed molecules on the cluster surface, L^* is the length of the contact line between the cluster and the solution, and it can be determined by the next equation:

$$L^* = 2\pi R_B \sin\vartheta \qquad 2.1.19$$

the $v_{i,diff}$ is the frequency related to vibrations leading to diffusion jumps and $\Delta e_{i,diff}$ is the activation energy for surface diffusion. Then, the frequency of diffusion jumps is given by $v_{i,diff} exp\left(\frac{-\Delta e_{i,diff}}{kT_0}\right)$. Vehkamäki (2006) [29] considers that the growth rate due to direct vapour deposition is typically orders of magnitude smaller than the rate of surface diffusion, and thus it is enough to use the surface diffusion growth coefficients.

2.1.3 Bubble detachment.

The detachment process is defined by all the volumetric and superficial forces that act on the bubble, in a gas-liquid system. These forces are included in the momentum transfer equation, in a source term representing external forces (see Eq. 2.2.3).

In this project, it is assumed that the volume of chlorine bubbles is a trunked sphere, as shown in Fig. 2.2, in which the volume changes with the variation of the contact angle (ϕ) on the electrode surface.
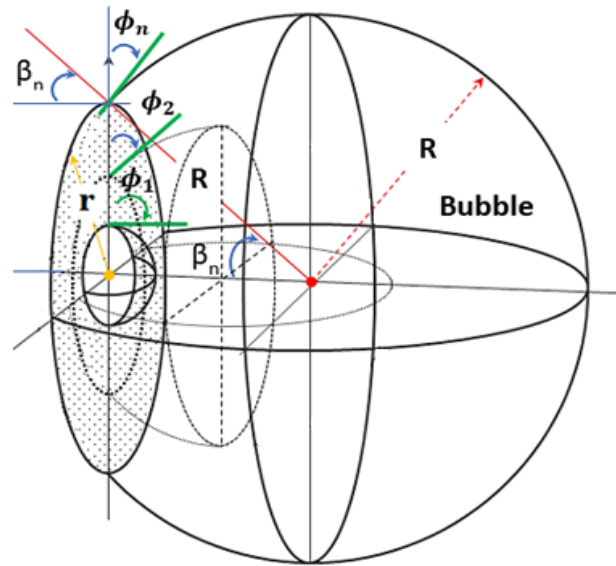
Fig. 2.2 The bubble volume in function of contact angle.

A force balance is computed on the bubble using Eq. 2.1.20 - 2.1.22.

$$V_{gas} = \frac{\pi}{3}R^3(2 + 3Cos\phi - Cos^3\phi) \qquad 2.1.20$$

$$F_{Bouyancy} + F_{Interfacial} = W_{bubble} \Rightarrow \rho_{Liq}gV_{gas} + \sigma_{sys}2\pi\, r = \rho_{gas}V_{gas}\, g \qquad 2.1.21$$

$$\Rightarrow V_{gas} = \frac{\sigma_{sys} 2\pi (R Sin\,\phi)}{g(\Delta\rho)} \qquad 2.1.22$$

Combining Eqs. 2.1.20 and 2.1.22, the bubble radius is a function of the contact angle, such as is shown in the Eq. 2.1.23.

$$R_{Bub} = \sqrt{\frac{6.\sigma_{sys}}{g.(\Delta\rho)} \frac{Sin\,\phi}{(2 + 3Cos\phi - Cos^3\phi)}} \qquad 2.1.23$$

where σ_{sys} is the interfacial tension, g the gravity and $\Delta\rho$ the difference between liquid density (ρ_l) and gas density (ρ_g).

Two forces are considered in this research work such as the drag force (F_{Drag}, Eq. 2.1.24), with a drag coefficient (C_D) based on the Schiller-Naumann correlation (see Eq. 2.1.25), and the Buoyancy force ($F_{Bouyancy}$, Eq. 2.1.26).

$$F_{Drag} = f_D = -\frac{3}{4}\frac{C_D}{d_{Bub}} \varphi_g \rho_l |\boldsymbol{u}_l - \boldsymbol{u}_g|(\boldsymbol{u}_l - \boldsymbol{u}_g) \qquad 2.1.24$$

$$C_D = \frac{24}{Re_{Bubble}}(1 + 0.15(Re_{Bubble}^{0.687})) \text{ with } Re_{Bubble} < 1000 \qquad 2.1.25$$

$$F_{Bouyancy} = \frac{1}{3}\pi R_{Bub}^3 (2 - 3Cos\phi + Cos^3\phi)(\rho_l - \rho_g)g \qquad 2.1.26$$

where d_{Bub} is the bubble diameter.

2.1.4 Bubble breakup.

The breaking of the surface of the bubble can be influenced by the properties of the gas as well as the medium where it has been formed, according to the fluid dynamics or thermodynamic properties. Clift et al. (1978) [31] present several numerical models that define this stage of the bubble. The model of bubble breakup that was taken for this project is the breakup of the bubble in the anodic boundary layer. It allows us to determine the effect of bubble breakup on the film overpotential of the boundary layer which prevents the transfer of the current density in the electrolyte solution:

2.1.4.1 Breakup due to velocity gradient.

This model is based on the behavior of a drop or bubble in a shear field that tends to rotate and deform the bubble. If the velocity gradients are large enough, interfacial tension forces are no longer able to maintain the fluid particle intact, and it ruptures into two or more smaller particles. Observations of drop and bubble breakup have also been obtained in hyperbolic flows. Fig. 2.3 shows tracings of photographs showing the effect of increasing shear rate.

Theoretical predictions related to the orientation and deformation of fluid particles in shear and hyperbolic flow fields are restricted to low Reynolds numbers and small deformations. The fluid particle may be considered initially spherical with radius r^*.
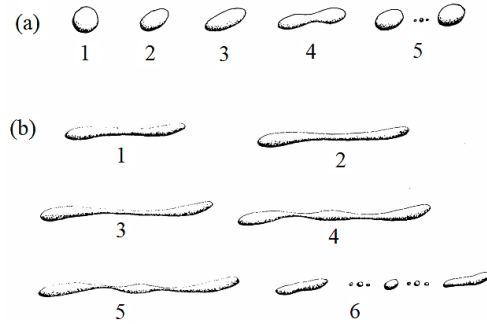
Fig. 2.3 Breakup of liquid drops in simple shear velocity gradient G increases in each sequence, from Clift et al. (1978).

Considering that the surrounding fluid is initially at rest, and that the fluid is impulsively given a constant velocity gradient G at time $t = 0$, the particle undergoes damped shape oscillations, finally deforming into an ellipsoid with axes in the ratio $E^{-1/2}: 1: E^{1/2}$, where:

$$\frac{1-E}{1+E} = \frac{5(19k+16)}{4(k+1)\sqrt{(19k)^2+\left(20/N\right)^2}} \text{ where } k = \frac{V}{d_A^3} \text{ and } N = r^*G\mu\sigma^{-1} \qquad 2.1.27$$

Where E is the aspect ratio averaged over shape oscillation ($E = b/a$, b is the sphere perimeter and a is the sphere radius), k the volumetric shape factor, V the sphere volume, d_A the sphere diameter, N the dimensionless velocity gradient, r^* the critical radius, μ, μ_P are the continuous and disperse phase viscosity and σ the interfacial or surface tension. The relaxation time for the oscillations is approximately:

$$\tau_r = r^*G\mu_P\sigma^{-1} \qquad 2.1.28$$

2.2 Transfer phenomena in bubble system.

Transfer phenomena are driven by variations in space and in time for the main variables and properties of a medium. The most important phenomena in the engineering are the transfer of heat, mass and momentum. For this project, only mass and momentum transfer inside the electrolytic solution will be considered, due to the high demand on computational resources of the simulation.

2.2.1 Mass transfer.

There are two types of mass transfer considered in this project. The first is the transfer of ions into the electrolyte solution using the Nernst-Planck equation (see the electrolytic phenomena section), and the second is the transfer of the chlorine gas bubble into the electrolyte solution. To represent the mass transfer of the gas bubble in the electrolyte solution will allow

us to analyse its effect on the resistance of the bubble to the passage of current in the boundary layer. The model presented below will allow us to develop the mass transfer of the chlorine bubble.

2.2.1.1 The bubble mass transfer.

The mass transfer inside a bubble system is developed by Bird (2007) (see Fig. 2.4), where the rate at which gas bubbles of A are absorbed by liquid B is estimated as the gas bubbles rise at their terminal velocity v_t through a clean quiescent liquid [32].

Bird (2007) consider the gas bubbles of moderate size, rising in a liquid free of surface-active agents, inside which a toroidal circulation is occurring, as shown in Fig. 2.4. The liquid moves downward relative to each rising bubble, enriched in species A near the interface in the manner of a falling film.
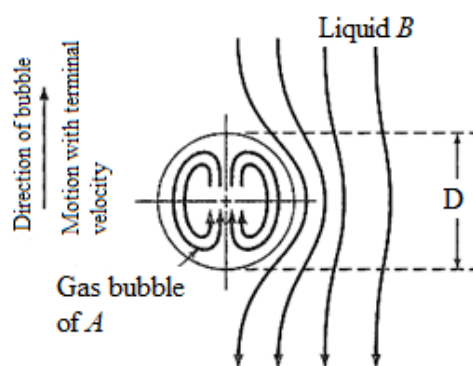
Fig. 2.4 Absorption of gas A into liquid B [32].

Hence the depth of penetration of the dissolved gas into the liquid is slight in the bulk, because of the motion of the liquid relative to the bubble and because of the typically low liquid-phase diffusivity $\mathcal{D}$. Thus, as a rough approximation, we can use Eq. 2.2.1 to estimate the rate of gas absorption, where D is the instantaneous bubble diameter. This gives an estimate of the molar absorption rate, averaged over the bubble surface, as:

$$(N_A)_{avg} = \sqrt{\frac{4\mathcal{D}_{AB}v_t}{\pi D}}\, C_{A0} \qquad\qquad 2.2.1$$

In this equation, C_{A0} is the concentration of gas A in liquid B at the interfacial temperature and partial pressure of gas A.

2.2.2 Momentum transfer.

In the electrolytic cell, the movement of fluid and bubbles in the solution are characterised by the momentum equation (Bird (2007) [32]). In this equation, three mechanisms are present: diffusion, convection and external forces process. Continuity (Eq. 2.2.2) and momentum (Eq. 2.5.3) equations must be solved to determine for the velocity field in the electrolytic solution.

$$\frac{\partial \rho}{\partial t} = -\nabla \cdot \rho \boldsymbol{v} \qquad\qquad 2.2.2$$

$$\frac{\partial (\rho \boldsymbol{v})}{\partial t} + \nabla \cdot \rho \boldsymbol{v}\boldsymbol{v} = -\nabla P - \nabla \cdot \tau + \rho \mathbf{g} + \sum \mathbf{F_{ext}} \qquad\qquad 2.2.3$$

Where ρ is the density of the solution, t the time, v the velocity vector, P the pressure, τ the fluid tensor, g the gravity acceleration and $\mathbf{F_{ext}}$ all the external forces that are acting on the fluid.

2.2.3 Electrolytic phenomena.

According with Oldham *et al.* 2012 [33] the transfer of mass inside an electrolytic solution is peculiar because an additional transfer mechanism is present: ions can be transferred due to migration, charged species being influence by the electrical field inside the cell. Moreover, the buoyancy, magnetic forces are the main sources of force at the origin of mass transfer in this ionic system.

2.2.3.1 Mass transfer in the electrolytic cell.

The Nernst-Planck equation is considering all three mass transfer mechanisms described above, the flux N_i of each i species in an electrochemical cell being calculated by:

$$N_i = c_i V - D_i \nabla c_i - \frac{z_i F}{RT} D_i c_i \nabla \Phi \qquad\qquad 2.2.4$$

Where z_i, c_i and D_i are respectively charge, concentration and diffusivity and V is the mean velocity, F the Faraday constant, R the universal gas constant, T the system temperature and finally Φ the potential field. The first, second and third term on the right side are respectively the convection, diffusion and migration of the i species. Applying the mass conservation law, it ends up to:

$$\frac{\partial c_i}{\partial t} = \nabla . N_i + R_i' \qquad\qquad 2.2.5$$

In the Eq. 2.2.5, homogeneous reactions are considered by the R_i' term, which is the net production or consumption rate of species i. The same set of equations must be written for every component. On the other hand, the mass transfer equation depends on electric field and current distribution which are coupled through the migration mechanism. The current density is expressed below making use of the Nernst-Planck equation:

$$i = -F \left(\nabla \sum_i z_i D_i c_i \right) - \frac{F^2}{RT} \nabla \Phi_l \sum_i z_i^2 D_i c_i + VF \sum_i z_i c_i \qquad\qquad 2.2.6$$

According to the Nernst-Planck equation, the unknown variables are the concentration of each species, electric potential and electrolyte velocity.

2.2.3.2   Butler-Volmer equation.

This equation, which represents the rate of the electrochemical surface reaction, links the current density and to the local overpotential. Starting with a reaction where O is the oxidant and R is the reductant like:

$$O + ne^- \leftrightarrow R \qquad\qquad 2.2.7$$

The Butler-Volmer (B-V) results to be:

$$i = i_0 \left[\exp\left\{ \beta_a n \frac{F}{RT} \eta \right\} - \exp\left\{ -\beta_c n \frac{F}{RT} \eta \right\} \right] \qquad\qquad 2.2.8$$

Where β_c, β_a are the transfer coefficients of reduction and oxidation reactions respectively, n is the number of electrons, i_0 the exchange current density and η the overpotential. The B-V equation (Eq. 2.2.8) shows the relation between the reactions overpotential and current density.

Typically, for other boundaries, the net current is zero representing electrically insulated boundaries. Due to the presence of an extreme nonlinearity in the B-V equation, various simplifications can be done whenever it is possible. Those simplifications allow the use of Tafel equation. At the anode, a high polarization approximation can be used when the reaction is slow. By doing so, only the exponential term related to oxidation is kept while the other part of the equation can be neglected. In this case, the equation is rewritten as:

$$\eta = \frac{RT}{\alpha F} \ln\left(\frac{i}{i_0}\right) \qquad\qquad 2.2.9$$

2.3 Previous research works on bubble in electrochemical field.

It is important to remark that the literature review on the research work on bubbles in electrolytic cells will be developed in more detail in chapters 3 and 4 of this project, depending on the specific objectives of each chapter. This section presents important research works for the electrochemical and fluid dynamics field. It shows the principal equations and the experimental data that defined the different bubble stages, as well as their effect on the fluid dynamics of the electrolytic solution. Furthermore, it shows the research on computing fluid dynamics (CFD) simulation of the bubbles system with Lagrangian-Eulerian (L-E) and Eulerian-Eulerian (E-E) approaches. In the L-E approach, the mathematical process that represents one bubble's behavior is taken as representative of a bubble set. On the other hand, in the E-E approach, a bubble set is considered in control volumes, meaning the equations represent all the bubbles, not one in particular.

The bubbles have been studied in different research fields, such as separation liquid-gas processes, wastewater, and electrochemical reactors. However, the electrolytic cell phenomena are more complex and difficult to study due to the dangerous conditions prevailing in electrolytic processes, especially in molten salt electrolysis. Thus, researchers have sought to develop

numerical methods to obtain enough information and resolve the main problems. The review of the literature has brought to light the use of different softwares to simulate those numerical methods in an electrolytic cell. Multiphysics simulation software has become one of the main tools for solving process problems in electrochemical reactors. The experimental data are important to validate the simulation of the numerical model developed. Therefore, it is important to know the different assumptions and boundary conditions made in those numerical methods to get accurate results. Table 2.1 shows some research works to let us develop the objective of this project.

Table 2.1. The main literature reviews.

Literature Review	Ref.	Field of Research	Exp. Data	CFD	Software
Riegel *et al*. (1998)	[17]	Alkaline water electrolysis	Developed	Bubble dynamics	Not used
Zhang *et al*. (2012)	[34]	Alkaline water electrolysis	Developed	Forces on bubble.	Not used
Liu *et al*. (2015)	[35]	Magnesium electrolysis	Developed	E-E approach	Comsol Multiphysics
El-Askary *et al*. (2015)	[16]	Alkaline water electrolysis	Developed	E-E approach	FORTRAN
Nouri *et al*. (2017)	[36]	PEM water electrolysis	From other article	Bubble dynamics	Direct CFD
Liu *et al*. (2017)	[37]	Numerical simulation	Developed	L-E approach	Comsol Multiphysics
Oliaii *et al*. (2017)	[8]	Lithium electrolysis	From other article	E-E approach	Comsol Multiphysics
Oliaii *et al*. (2018)	[9]	Lithium electrolysis	From other article	E-E approach	Comsol Multiphysics
Martinez *et al*. (2018)	[38]	Electroflotation	Developed	Not developed	Not developed
Litrico *et al*. (2018)	[10]	Lithium electrolysis	From other article	E-E approach	OpenFoam
Mahvelati *et al*. (2018)	[39]	CFD of a water electrolysis cell	From other article	Population balance	OpenFoam
Zhao *et al*. (2020)	[15]	Lithium electrolysis	From other article	E-E approach	Comsol Multiphysics
Takamure *et al*. (2020)	[18]	Water electrolysis	Developed	E-E approach	OpenFoam
Pan *et al*. (2020)	[19]	CFD of the water	Developed	E-L approach	ANSYS Fluent

Table 1.1 shows the main contributions of this project compared to the published articles on lithium electrolysis cell (Oliaii *et al.* 2017-18, Litrico *et al.* 2018 and Zhao *et al.* 2020) [8], [9], [10], [15]. It also shows the articles used for the validation of the fluid dynamics of the molten salt LiCl-KCl, such as the research works of Riegel *et al.* 1998, El-Askary *et al.* 2015, Takamure *et al.* 2020 and Pan *et al.* 2020 [17], [16], [18], [19].

In this work, the validation of electrochemical results is based on Oliaii et al. (2017-18) [8], [10] using an anode-cathode distance (ACD) of 0.0635 m. The main difference between their works and this research comes from the assumptions made and the physics that is taken into account. For example, in their first article, empirical equations (Bruggeman and Vogt correlations) were added to the transfer equations to represent the resistance caused by the bubbles at the anode surface, with a one-phase fluid dynamic mimicking bubble flow buoyancy through the vertical movement of the anode. In their second article, a two-phase system was simulated with a porous diaphragm. In both papers, fluid dynamics at the cathode surface was neglected and a turbulent Reynolds for bubbles was assumed.

We proposed a model closer to the real application, representing a two-phase flow with the bubble resistances locally, either on the anode surface or in the electrolytic solution. This model also has improved the representation of the multiphase flow inside the cell by accounting for liquid-gas flow at the anode and liquid-liquid flow at the cathode. The mathematical model accounted for charge and mass transfer using a tertiary current density distribution (TCD), including electrochemical kinetics at the electrodes and multicomponent mass transfer in a molten salt. Furthermore, we proposed a new and more accurate approach to represent the two-phase boundary layer that forms on the anode surface. For the boundary layer validation, we took experimental data from Riegel *et al.* 1998 [17], and simulation data from El-Askary *et al.* 2015 [16].

The new mathematical model proposed has been developed through a simulation using Comsol Multiphysics®. That simulation was based on an Euler-Euler approach including turbulence $k - \varepsilon$ model, and it allowed to predict the concentrations of gaseous Cl_2 and liquid Li in the cell and to estimate the risks of secondary reaction between these products. The initial data for the CFD simulation were taken from the articles of Mahvelati *et al.* 2018 [39], the bubble nucleation process on the anodic surface was taken from the work of Nouri *et al.* 2017 [36], and finally, the change of the contact angle as a function of time was taken from the research work of Zhang *et al.* 2012 [34] and Martinez *et al.* 2018 [38].

Validation of our results of the fluid dynamics developed in the molten salt due to the bubble effect was performed using water electrolysis data. The results of the fluid dynamics of this project were compared with the results published by El-Askary *et al.* 2015 [16], Takamure *et al.* 2020 [18] and Pan *et al.* 2020. The simulation of El-Askary *et al.* (2015) [16] was based on a turbulent k-ε model, an approach also used by Takamure *et al.* (2020) [18], and Pan et al. (2020) [19]. El-Askary *et al.* [16] studied the bubble hydrodynamics of the hydrogen evolution

process through water electrolysis in a square cell. They used a cathode and anode with a vertical surface area 0.1 m high and 0.05 m wide. The experimental electrolytic process was carried out with a continuous flow of KOH-electrolyte between the electrodes, using a square electrolytic cell with a membrane in the middle of the distance between the two electrodes. El-Askary *et al*. [16] assumed no-slip conditions at the electrodes' surface and applied a current density of 6250 A/m^2. Takamure *et al*. [18] made an experimental study on the effect of bubble fluid dynamics in a square electrolytic water cell adding transversal cylindrical bars to bubble flow, and they got the same behaviour velocity results as El-Askary *et al*. [16] in their experiment. Finally, Pan *et al.* [19] studied turbulence induced by buoyancy forces in bubble plumes in a bubble column.

The novelty of this research work is in the combination of several physical phenomena developed in the lithium electrolytic cell, which allows to obtain results closer to reality, though with the limitation of the high demand of computational resources.

CHAPITRE 3 : AVANT-PROPOS

Auteurs et affiliation:

• Juan Manuel Melendez: étudiante au doctorat, Université de Sherbrooke, Faculté de génie, Département de génie chimique et de génie biotechnologique.

• Martin Désilets: professeur, Université de Sherbrooke, Faculté de génie, Département de génie chimique et de génie biotechnologique.

• Gaétan Lantagne: professeur associé, Université de Sherbrooke, Faculté de génie, Département de génie chimique et de génie biotechnologique.

• Elaheh Oliaii: chercheuse, Nouveau Monde Graphite Inc.

Titre français: Effet de la dynamique des fluides des bulles et des gouttes de liquide sur la recombinaison du lithium à l'intérieur d'une cellule électrolytique au lithium avec diaphragme.

Contribution au document:

La contribution principale de cet article scientifique est basée sur la combinaison des phénomènes électrochimiques avec le transfert de masse et de momentum sans l'utilisation d'équations empiriques. À partir de cette combinaison découlent les autres contributions, soit : la simulation des étapes de la formation des bulles sur la surface anodique; les différentes méthodes de validation de la dynamique des fluides dans la solution électrochimique; et enfin, l'effet de la dynamique des fluides des bulles de chlore et des gouttelettes de lithium sur la recombinaison et la consommation d'énergie des différents processus électrochimiques.

Résumé français

Le lithium métallique, qui est un métal critique et stratégique pour la production mondiale de dispositifs de stockage d'énergie, est principalement produit par électrolyse en sels fondus. Pour augmenter l'efficacité du processus, il est de la plus haute importance d'empêcher la recombinaison du lithium pendant le processus afin d'éviter le gaspillage d'énergie. Cette

recherche étudie le comportement des principales variables impliquées dans la réaction à l'intérieur d'une cellule expérimentale de production de Li du point de vue du transfert de masse, de l'électrochimie et de la dynamique des fluides. Les simulations ont été effectuées pour un intervalle de temps total d'électrolyse de 600 s en utilisant une approche turbulente (k-ε) pour résoudre l'écoulement biphasique couplé au processus d'électrolyse du lithium. Pour analyser l'influence de la dynamique des fluides cathodiques en relation avec la quantité de lithium recombiné, deux configurations du diaphragme ont été évaluées, notamment l'incorporation d'une chicane au fond de la cellule et l'inclinaison du diaphragme. Le déflecteur a réduit la quantité de lithium recombiné de 7 %, et le diaphragme avec une inclinaison < 90° a réduit la masse totale recombinée de 77 %, bien qu'il ait augmenté la consommation d'énergie de 10 % par rapport au cas de base d'un diaphragme vertical.

3 Article 1: Effect of Bubbles and Liquid Drops Fluid Dynamics on the Lithium Recombination inside a Lithium Electrolytic Cell with Diaphragm.

Juan Meléndez [a], Martin Désilets [a], Gaétan Lantagne [a], Elaheh Oliaii [a].

[a] Department of Chemical and Biotechnological Engineering, Université de Sherbrooke, Sherbrooke, Qc J1K 2R1, Canada.

Abstract: Metallic lithium, which is a critical and strategic metal for the world's production of energy storage devices, is mainly produced from molten salt electrolysis. To increase the efficiency of the process, it is of utmost importance to prevent lithium recombination during the process to avoid energy waste. This research studies the behavior of the main variables involved in the reaction inside a *Li*-production experimental cell from the mass transfer, electrochemical and fluid dynamics standpoints. Simulations were done for a total electrolysis time interval of 600 s using a turbulent (k-ε) approach to solve the two-phase flow coupled to the lithium electrolysis process. To analyze the influence of cathode fluid dynamics in relation with the amount of recombined lithium, two configurations of the diaphragm were evaluated including the incorporation of a baffle at the bottom of the cell and the inclination of the diaphragm. The baffle reduced the amount of recombined lithium by 7 %, and the diaphragm with an inclination < 90° reduced the total recombined mass by 77 %, although it increased the energy consumption by 10 % with respect to the base case of a vertical diaphragm.

Keywords: Bubble fluid dynamic, electrochemical process, momentum transfer validation, fluid dynamics on the cathode surface, lithium liquid recombined.

3.1 Introduction.

The production of metallic lithium is getting attention and importance due to the world growing demand and increasing number of applications. In particular, new generations of batteries such as lithium-air, lithium-sulfur and more generally all-solid-state batteries strongly depend on a metallic lithium anode. This trend might induce a significant demand for metallic lithium as stated in a recent IEA report on the role of critical minerals in clean energy transitions [2]. Due to these considerations, there has been a particular interest in developing new techniques and designs for lithium production electrolytic cells in the last years [10], [15], [41]–[43]. Fig. 3.1 shows a simplified schematic of a *Li*-experimental electrolysis cell.

One way to produce metallic lithium is through its electrolysis in molten salts. This technology comes with important challenges related to chlorine bubble production at the anode, which in turn creates a resistance to mass transfer, resulting in high energy consumption and dangerous toxicity for the environment [8], [44]–[47].
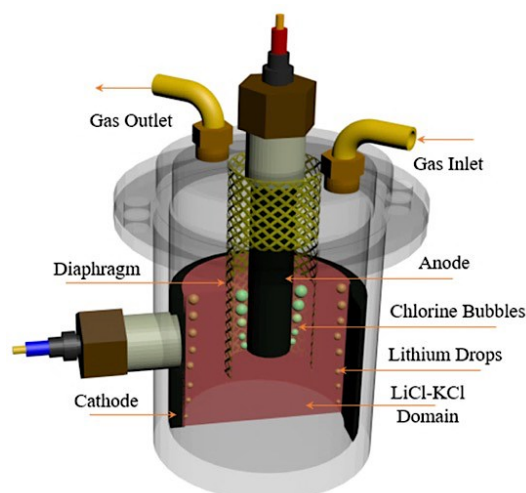
Fig. 3.1 Lithium electrolytic cell and its numerical domain.

Despite the importance of models' validation, very scarce experimental data is available on lithium electrolysis to assess the simulation results, because the majority of the data comes from patents, a consequence of the economic importance of lithium. Recently, Oliaii et al. (2017-18), Litrico et al. (2018) and Zhao et al. (2020) have achieved to provide numerical results showing the main fields inside lithium electrolysis cells [8]–[10]. In this work, the validation of electrochemical results is based on Oliaii et al. (2017-18) using an anode-cathode distance (ACD) of 0.0635 m. The main differences between their works and this research comes from the assumptions made and the physics notions that are considered.

Similarly, scarce experimental data complicated the validation of bubble fluid dynamics in molten salt electrolysis reactors. Despite this limitation, the presented work is validated based on the fluid dynamics of bubbles in water, an approach already taken by Liu et al. (2015) who have validated their modeling results with experimental data from the air bubble-water system [47]. In the same way, the simulations of El-Askary et al. (2015), Takamure et al. (2020) and Pan et al. (2020) were taken for the validation of this work research. Their simulations are based on a turbulent k-ε model in water-air bubbles systems [16]–[19]. El-Askary et al. (2015) studied the bubble hydrodynamics of the hydrogen evolution process through water electrolysis in a square cell. The experimental electrolytic data was taken from Riegel et al. (1998) who used a continuous flow of KOH electrolyte and applied a current density of $6250 \ A/m^2$ between the electrodes. Takamure et al. (2020) made an experimental study on the effect of bubble fluid dynamics in a square electrolytic water cell, adding transversal cylindrical bars between electrodes to modify bubble fluid dynamics. Finally, Pan et al. (2020) studied turbulence induced by buoyancy forces in bubble plumes in a bubble column. The main differences of last research works are underlined in Table 3.1.

The main objective of this research work is to analyze the impact of cell design on lithium production and energy costs through the chlorine bubbles and lithium liquid drops fluid dynamics. This analysis is relying on the intimate coupling of the conservation equations

(momentum, mass, and charges) representing the most important phenomena occurring inside the molten salt lithium.

Table 3.1. Literature review comparison with 2D geometry.

Literature Review	Electrolysis and Phases	Diaphragm	Anode Surface Phenomena			Electrolyte Solution			Cathode Surface Phenomena		
			ECH	BFor	VEL	ABL	MAT	MOT	ECH	DFor	VEL
Oliaii et al. (2017) [8]	Li - One	Non porous	Tafel	VOC	Flat Plate	BRC	NPE	NS k-ε	LBV	No	No
Oliaii et al. (2018) [9]	Li - Two	Porous	Tafel	VOC	FAL	BRC	NPE	NS k-ε	LBV	No	No
Litrico et al. (2018) [10]	Li - Two	No	Tafel	VOC	FAL	No	NPE	NS k-ε	LBV	No	No
Zhao et al. (2020) [15]	Li - Two	No	PCD	CMB	FAL	No	NPE	NS k-ε	PCD	No	No
El-Askary et al. (2015) [16]	H₂O - Two	No	BV	HBM	FAL	MLB	HBM	NS k-ε	BV	No	No
Riegel et al. (1998) [17]	H₂O - Two	No	BV	HBM	EMC	No	HBM	NS k-ε	BV	No	No
Takamure et al. (2020) [18]	H₂O - Two	No	PCD	FAL	EMC	EMC	HBM	NS k-ε	PCD	No	No
Pan et al. (2020) [19]	H₂O -Air	No	No	No	No	NS k-ε Fluid Dynamics			No	No	No
This Project	Li - Two	Non porous	Tafel	CMB	CMB	No	NPE	NS k-ε	LBV	LMB	LMB

ECH : Electrochemical Field; **BFor - DFor** : Bubble and Drop Formation; **VEL** : Flow Velocity; **ABL** : Anode Boundary Layer; **MAT - MOT** : Mass and Momentum Transfer; **VOC** : Vogt Correlation; **BRC** : Bruggeman Correlation; **NPE** : Eq. Nernst-Planck; **NS k-ε** : Turbulent k-ε Navier-Stokes Equation; **BV - LBV** : Butler-Volmer and Linearized Equation; **FAL** : Faraday Law; **PCD** : Primary Current Distribution; **HBM - CMB - LMB** : Mass Balance of Water, Chlorine and Lithium; **MLB** : Mixing Length Boundary; **EMC** : Empirical Correlation.

The simulations were validated on the work of Oliaii et al. and Zhao et al., who looked at the same subject without considering the fluid dynamics of lithium liquid drop at the cathode surface. The lithium recombination was predicted by the interaction between the electrolyte movement produced by the chlorine bubbles at the anode surface, in addition to the lithium liquid drops induced movement at the cathode surface and the electrochemical reactions at both electrodes.

3.2 Simulation.

Lithium electrolysis simulations were conducted with Comsol Multiphysics® using the Eulerian Bubbly Flow Model to represent the momentum transfer produced by the bubbles inside the electrolytic solution at the anode [48], and the Eulerian Mixture Model to predict the fluid dynamics of lithium liquid droplets produced at the cathode surface [49]. The Electrochemical Model with Tertiary Current Distribution (TCD) was used to simulate the electrochemical reactions at the surface of the electrodes and the ions mass transfer inside the electrolyte [50].

3.2.1 General information.

The geometry of the lithium electrolytic diaphragm cell was taken from Oliaii et al. (2017) as shown in Fig. 3.2. According to Lovering (1982), it is very important to take into account the presence of the diaphragm, which is used to separate the chlorine gas from the liquid lithium

and to prevent the recombination of these products [51]. In this simulation, it takes the form of a non-porous smooth flat surface that is located in the anode-cathode gap and extends below the bottom of the anode.
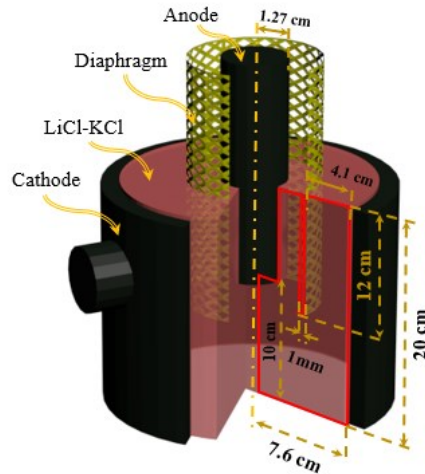
Fig. 3.2 Geometry of the computational domain.

Fig. 3.3 illustrates the main physical and chemical phenomena (the bubbles, fluid dynamics, electrochemical reactions, and mass transfer) that were considered in the model developed. The transitory state of the conservation equation was used to analyze the different stages of the process during a period of 10 min, a sufficient time to capture the main effects. The initial parameters of Oliaii et al. (2017) and Zhao et al. (2020) were used. The following general assumptions have been considered: 1. the reactor is operated at a constant temperature of 723 K, 2. the hydrodynamic properties of the $LiCl - KCl$ molten salt solution at 723 K are close to those of water, with no significant change in its volume during the reactions, 3. the chlorine gas density is estimated using ideal gas behavior.
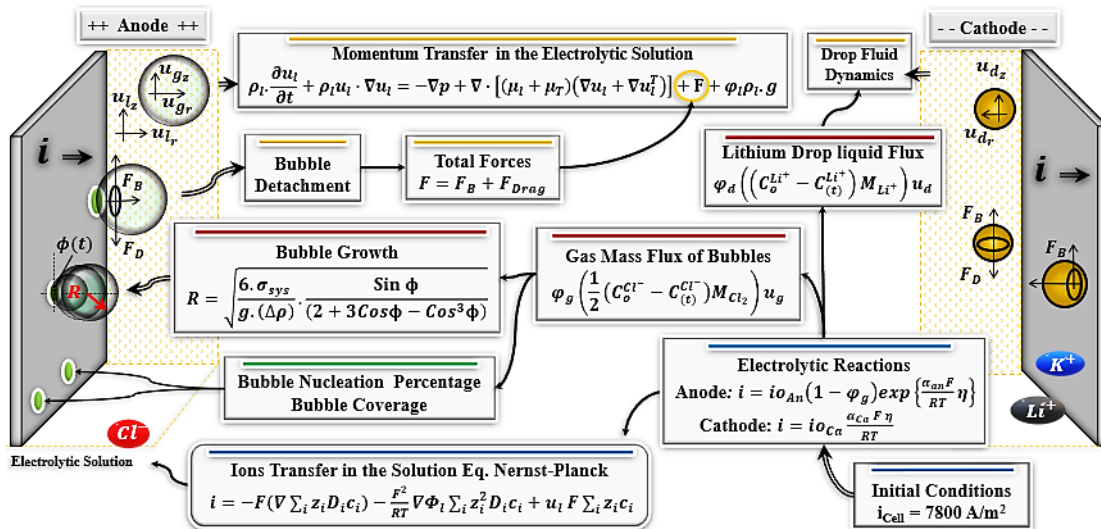
Fig. 3.3 Diagram of the main phenomena considered in this work.

3.2.2 Electrochemical model.

Momentum and mass transfer are intimately coupled to electrode kinetics and electric field through the mass fluxes and generation/consumption source terms that are determined using the Nernst-Planck equation (Eq. 3.2.1) and the simplified Butler-Volmer equation (Eq. 3.2.5). The electrochemical process is simulated as a TCD assuming electroneutrality in the solution, which means that $\sum_i (z_i c_i) = 0$ everywhere and at all times. The electrochemical double is considered as a part of the electrode. The lithium electrolysis reactions considered in this paper are shown below:

$$\text{Anode (Oxidation): } 2Cl^- \rightleftharpoons Cl_{2\,(g)} + 2e^-$$

$$\text{Cathode (Reduction): } 2Li^+ + 2e^- \rightleftharpoons 2Li_{(l)}$$

$$\text{Total Reaction: } 2Li^+ + 2Cl^- \rightleftharpoons 2Li_{(l)} + Cl_{2\,(g)}$$
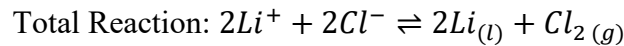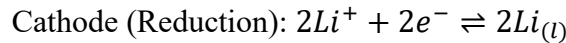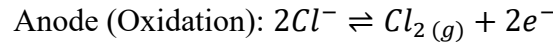
The simulation starts when a current density of $7800 \; A/m^2$ is applied to the cell. The electrochemical parameters are taken from Table 3.2.

Table 3.2. Electrolytic parameters [8], [15].

$E_{eq_{An}}$	3.6 V	Anode equilibrium potential
$i_{o_{An}}$	10 A/m²	Anode exchange current density
α_{An}	0.5	Anode transfer coefficient
σ_l	157 S/m	Electrolyte conductivity
$E_{eq_{Ca}}$	0 V	Cathode equilibrium potential, ref potential
$i_{o_{Ca}}$	1000 A/m²	Cathode exchange current density
α_{Ca}	0.5	Cathode transfer coefficient
i_{Anodic}	7800 A/m²	Anodic current density
$i_{Cathodic}$	625 A/m²	Nominal cathodic current density
$C_{o_{Li^+}}$	19.2 kmol/m³	Initial Li^+ concentration
$C_{o_{K^+}}$	10.8 kmol/m³	Initial K^+ concentration
$C_{o_{Cl^-}}$	30.0 kmol/m³	Initial Cl^- concentration

The ions mass transfer in the electrolytic solution is peculiar because an additional transfer mechanism is present: ions can be transferred due to migration, charged species being influenced by the electrical field inside the cell. The mass transfer equation (Nernst-Planck equation) expressed in terms of current density and it is shown in the Eq. 3.2.1 [52]–[54]:

$$i = -F\left(\nabla \sum_i (z_i D_i c_i)\right) - F^2 \sum_i (z_i^2 u m_i c_i)\,\nabla \Phi_l + u_l F \sum_i (z_i c_i) \qquad 3.2.1$$

According to Eq. 3.2.1, the unknown variables are the concentration of each species, the electric potential, and the electrolyte velocity. The ion mobility (um_i) in the electrolytic solution is calculated using Eq. 3.2.2 (Stoke-Einstein correlation) and depends on the concentration of each ion. Eq. 3.2.3 was used to compute the mixture conductivity.

$$um_i = \frac{D_i}{R.T} \qquad \text{3.2.2}$$

$$\sigma_{C_i} = F^2 . \sum_{i=1}^{k} (z_i)^2 . um_i . c_i \qquad \text{3.2.3}$$

Tafel equation (Eq. 3.2.4) was used at the anode due to the sluggishness of the reaction. In a multiphase electrolytic system, the bubbles create a hyperpolarization, an overpotential caused by the gas bubbles coverage on the anode surface. The bubble coverage φ_{Bc} is representing the fraction of the electrode surface covered by bubbles. Thus, only the rest of the electrode surface $(1 - \varphi_{gas})$ is available for electrochemical reactions. The next equation represents the current density on the anode surface considering the bubble coverage overpotential.

$$i_{An} = i_{0_{An}} (1 - \varphi_{Bc}) \, exp\left(\frac{\alpha_{An}.F}{R.T} \eta\right) \qquad \text{3.2.4}$$

The Linearized Butler-Volmer (LBV) equation (Eq. 3.2.5) was applied at the cathode surface.

$$i_{Ca} = i_{0_{Ca}} \frac{\alpha_{Ca}F\eta}{RT} \qquad \text{3.2.5}$$

3.2.3 Mass transfer.

The equation of mass transfer inside the electrolytic solution produced by the electrochemical reaction was defined by Eq. 3.2.6. During bubbles and drops formation, it is assumed that there is no gas and lithium diffusion into the electrolyte solution. Also, the homogeneous reactions represented by the term R_i', which is taken as zero assuming that only electrochemical reactions are taking place.

$$\frac{\partial c_i}{\partial t} = \nabla . N_i + R_i' \Rightarrow \partial c_i = (\nabla . N_i)\partial t \qquad \text{3.2.6}$$

$$N_i = c_i V - D_i \nabla c_i - \frac{z_i F}{RT} D_i c_i \nabla \Phi \qquad \text{3.2.7}$$

$$D_i = D_{i,eff} + D_T \qquad \text{3.2.8}$$

$$D_{i,eff} = \frac{1 - x_i}{\sum_{\substack{i=1 \\ i \neq j}} \frac{x_j}{D_{i,j}}} \qquad \text{3.2.9}$$

Three mass transfer mechanisms were considered in Eq. 3.2.7: migration, diffusion, and convection. N_i represents the total molar flux of each i species in an electrochemical cell, z_i and c_i are the charge and concentration respectively, and Φ the potential field. The diffusivity D_i is

composed of its molecular ($D_{i,eff}$), taken by Wilke's correlation that includes the non-ideal effects of the solution and the turbulent (D_T) components [9], [10], [35]. The molecular diffusivity of each ion in the electrolytic solution mixture was estimated using Wilke's correlation [8], Eq. 3.2.9. The turbulent diffusivity was taken from the turbulent viscosity of the electrolyte, assuming a Schmidt number equal to one. The diffusivity used in the simulation of lithium electrolysis was taken from Table 3.3.

Table 3.3. Mass transfer parameters [8], [15].

$D_{Li^+_{LiCl}}$	$3.0\text{x}10^{-9}$ m²/s	Binary diffusion coefficient of Li^+ ions in $LiCl$
$D_{Li^+_{KCl}}$	$2.0\text{x}10^{-9}$ m²/s	Binary diffusion coefficient of Li^+ ions in KCl
$D_{Cl^-_{LiCl}}$	$3.0\text{x}10^{-9}$ m²/s	Binary diffusion coefficient of Cl^- ion in $LiCl$
$D_{Cl^-_{KCl}}$	$1.5\text{x}10^{-9}$ m²/s	Binary diffusion coefficient of Cl^- ion in KCl
$D_{K^+_{LiCl}}$	$2.0\text{x}10^{-9}$ m²/s	Binary diffusion coefficient of K^+ ions in $LiCl$
$D_{K^+_{KCl}}$	$1.5\text{x}10^{-9}$ m²/s	Binary diffusion coefficient of K^+ ions in KCl

It is assumed that the volumes of chlorine bubbles and Li liquid drops are constant and of spherical form, as shown in Fig. 3.4. The radius of those spheres is a function of constant contact angle (ϕ) as determined in Eq. 3.2.12.
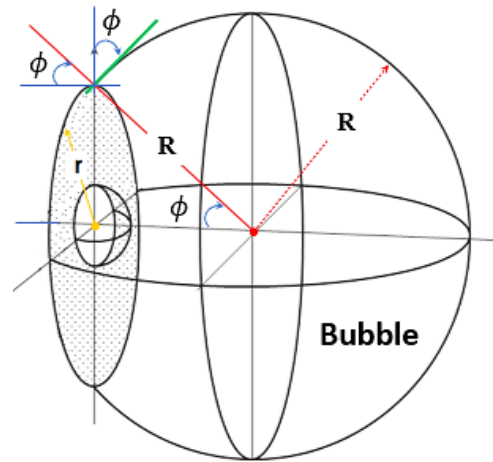
Fig. 3.4 The bubble and drop geometry.

A force balance was computed on the bubble using Eq. 3.2.10 - 3.2.12.

$$V_{gas} = \frac{\pi}{3}R^3(2 + 3Cos\phi - Cos^3\phi) \qquad 3.2.10$$

$$F_{Bouyancy} + F_{Interfacial} = W_{bubble} \Rightarrow \rho_{Liq}gV_{gas} + \sigma_{sys}2\pi\,r = \rho_{gas}V_{gas}g \qquad 3.2.11$$

$$\Rightarrow V_{gas} = \frac{\sigma_{sys}2\pi(RSin\,\phi)}{g(\Delta\rho)} \qquad 3.2.12$$

Combining Eqs. 3.2.10 and 3.2.12, the bubble radius is a function of the contact angle (see Eq. 3.2.13). A similar equation has been obtained by Zhang and Zeng (2010-12) [34].

$$R_{Bubble} = \sqrt{\frac{6.\sigma_{sys}}{g.(\Delta\rho)} \frac{Sin\,\phi}{(2 + 3Cos\phi - Cos^3\phi)}} \qquad 3.2.13$$

3.2.4 Momentum transfer.

According to Tomiyama et al. (2002), the velocity field produced in the electrolytic solution is due to the displacement of chlorine bubbles and lithium liquid drops to the top of the electrolyte surface and can be described through the momentum equation [55], [56]. The main objective of this section is to define the mixture momentum and continuity equations as a function of liquid and gas velocities. The parameters to simulate these phenomena are shown in Table 3.4.

Table 3.4. Fluid dynamic parameters [8], [15].

u_o	1 mm/s	Initial electrolyte velocity
ρ_g	1.77 kg/m³	Cl_2 gas density
Ts	723 K	System temperature
Ps	1 atm	System pressure
ρ_l	1648 kg/m³	Electrolyte density
μ_l	7.5x10⁻³ Pa.s	Electrolyte viscosity
$\rho_{Li(liq)}$	512 kg/m³	Lithium density
$\mu_{Li(liq)}$	4.6x10⁻³ Pa.s	Lithium viscosity

The flow regime in the electrolyte solution was determined through the Grashof number. In the development of the general momentum transfer, gas density was considered negligible compared to liquid density. Also, the motion of gas bubbles relative to the liquid was determined by a balance between viscous drag and pressure forces and it was assumed that the two phases share the same pressure field. Based on these assumptions, the momentum and continuity equations of the two phases can be combined. The general momentum equation is [32], [57], [58]:

$$\varphi_l\rho_l.\frac{\partial u_l}{\partial t} + \varphi_l\rho_l u_l \cdot \nabla u_l = -\nabla p + \nabla \cdot [\varphi_l(\mu_l + \mu_T)(\nabla u_l + \nabla u_l^T)] + \varphi_l\rho_l.g + F \qquad 3.2.14$$

In Eq. 3.2.14, u_l is the liquid velocity vector, p the pressure, φ_l the liquid volume fraction, ρ_l the electrolyte density, g the gravity vector. F stands for any additional volume force, μ_l the dynamic viscosity of the liquid, and μ_T the turbulent viscosity.

$$u_g = u_l + u_{slip} + u_{drift} \text{ with } u_{slip} = 0 \text{ on the anode surface} \qquad 3.2.15$$

$$\boldsymbol{u}_{drift} = -\frac{\mu_T \, (\nabla \varphi_g)}{\rho_l \, \varphi_g} \qquad\qquad 3.2.16$$

where $\boldsymbol{u}_{drift}$ is the drift velocity and μ_T is a turbulent viscosity causing the drift. The $k - \varepsilon$ turbulence model was used to find μ_T as described in the next equations [19], [56]. The variables k and ε represent the turbulent kinetic energy and dissipation rate, respectively.

$$\mu_T = \rho_l C_\mu \frac{k^2}{\varepsilon} \qquad\qquad 3.2.17$$

$$\rho_l \frac{\partial \varepsilon}{\partial t} + \rho_l (\boldsymbol{u}_l \cdot \nabla)\varepsilon = \nabla \cdot \left[\left(\mu_l + \frac{\mu_T}{\sigma_\varepsilon}\right)\nabla\varepsilon\right] + C_{\varepsilon 1}\frac{\varepsilon}{k}P_k - C_{\varepsilon 2}\frac{\varepsilon^2}{k} + C_\varepsilon \frac{\varepsilon}{k}S_k \qquad\qquad 3.2.18$$

$$\rho_l \frac{\partial k}{\partial t} + \rho_l (\boldsymbol{u}_l \cdot \nabla)k = \nabla \cdot \left[\left(\mu_l + \frac{\mu_T}{\sigma_k}\right)\nabla k\right] + P_k - \rho_l \varepsilon + S_k \qquad\qquad 3.2.19$$

with $S_k = -C_k(\varphi_g \nabla p)(\boldsymbol{u}_g - \boldsymbol{u}_l)$ and $P_k = \mu_l[\nabla\mu_l : (\nabla\mu_l + (\nabla\mu_l)^T)]$ $\qquad\qquad 3.2.20$

$C_\mu = 0.09, C_k = 0.505, C_\varepsilon = 1.46, C_{\varepsilon 1} = 1.44, C_{\varepsilon 2} = 1.92, \sigma_\varepsilon = 1.3, \sigma_k = 1.3$

The pressure gradient in the S_k term of Eq. 3.2.20 was determined by using the drag force [59]–[61], f_D, as shown in the next equation:

$$\varphi_g \nabla p = f_D \qquad\qquad 3.2.21$$

Here f_D can be written as:

$$f_D = -\frac{3}{4}\frac{C_D}{d_{Bub}} \, \varphi_g \rho_l |\boldsymbol{u}_l - \boldsymbol{u}_g|(\boldsymbol{u}_l - \boldsymbol{u}_g) \qquad\qquad 3.2.22$$

where d_{Bub} is the bubble diameter, and C_D the viscous drag coefficient. Given C_D and d_{Bub}, Eq. 3.2.15 was used to calculate the slip velocity between the bubble surface and the electrolytic solution. The Hadamard-Rybczynski model [62] was used to evaluate the drag coefficient, an adequate approach for spherical bubbles with a diameter of less than 2 mm:

$$C_D = \frac{16}{Re_{Bubble}} \quad \text{and} \quad Re_{Bubble} = \frac{d_{Bub} \cdot \rho_L |\boldsymbol{u}_l - \boldsymbol{u}_g|}{\mu_l} \qquad\qquad 3.2.23$$

The liquid volume fraction (φ_l) was computed from the gas volume fraction (φ_g):

$$\varphi_l = 1 - \varphi_g \qquad\qquad 3.2.24$$

The continuity equation is

$$\frac{\partial}{\partial t}\left(\varphi_l \rho_l + \varphi_g \rho_g\right) + \nabla \cdot \left(\varphi_l \rho_l \boldsymbol{u}_l + \varphi_g \rho_g \boldsymbol{u}_g\right) = 0 \qquad\qquad 3.2.25$$

The liquid density change with time is caused by the mass transfer rate of gas into the liquid phase, as $m_{gl} = \frac{\partial}{\partial t}(\varphi_l \rho_l)$. Considering that $m_{gl} = 0$, $\nabla \cdot (\varphi_l \rho_l \boldsymbol{u}_l) = 0$ in Eq. 3.2.25. Finally, the gas phase transport equation can be defined as:

$$\frac{\partial(\varphi_g \rho_g)}{\partial t} + \nabla \cdot \left(\varphi_g \rho_g \boldsymbol{u}_g\right) = 0 \qquad\qquad 3.2.26$$

$$\varphi_g \rho_g \boldsymbol{u}_g = \varphi_g \left(\frac{1}{2} \left(C_o^{Cl^-} - C_{(t)}^{Cl^-} \right) M_{Cl_2} \right) \boldsymbol{u}_g \qquad \text{3.2.27}$$

where $C_o^{Cl^-} - C_{(t)}^{Cl^-}$ represents the chlorine ions consumed by the reaction, M_{Cl_2} the chlorine molecular weight.

To evaluate the volume fraction the gas phase φ_g on the anode surface, the interfacial area is needed to define the bubble number density (the number of bubbles per liquid volume). This momentum model assumes that the gas bubbles can expand or shrink but not completely vanish, merge, or split. Thus, the conservation of the number density n, gives:

$$\frac{\partial n}{\partial t} + \nabla \cdot (n \boldsymbol{u}_g) = 0 \qquad \text{3.2.28}$$

The forces such as the drag force of (Eq. 3.2.22), with a drag coefficient based on the Schiller-Naumann correlation (see Eq. 3.2.29), and the Buoyancy force (f_B), are included in the additional force term ($\boldsymbol{F}$) of the momentum equation [36], [59], [63].

$$C_D = \frac{24}{Re_{Bubble}} (1 + 0.15(Re_{Bubble}{}^{0.687})) \text{ with } Re_{Bubble} < 1000 \qquad \text{3.2.29}$$

$$f_B = \frac{1}{3} \pi R^3 (2 - 3Cos\phi + Cos^3\phi)(\rho_l - \rho_g)g \qquad \text{3.2.30}$$

where ϕ is the contact angle between the solid surface and the bubble interface.

The equations representing the lithium liquid drop fluid dynamics on the cathode surface are the same as those for the bubble fluid dynamics (Eqs. 3.2.14 - 3.2.30), with the following differences. The liquid velocity vector in Eq. 3.2.14 is the total velocity ($\boldsymbol{j}$) which is defined as the sum of the velocity to each phase multiplied by its volume fraction.

$$\boldsymbol{j} = \boldsymbol{j}_c + \boldsymbol{j}_d \text{ with } \boldsymbol{j}_c = \varphi_c \boldsymbol{u}_c \text{ and } \boldsymbol{j}_d = \varphi_d \boldsymbol{u}_d \qquad \text{3.2.31}$$

where $\boldsymbol{j}_c, \boldsymbol{j}_d$ are the continuous (electrolyte) and the dispersed (lithium drops) phase mixture velocities respectively, $\boldsymbol{u}_c, \boldsymbol{u}_d$ are the continuous and the dispersed phase velocity vectors, and φ_c, φ_d denote the volume fractions of the continuous and dispersed phases.

The Grashof number is used to define the flow regime in the electrolyte solution, and it is defined by Eq. 3.2.32:

$$Gr = \frac{g(L_c)^3 \left[\rho_l - \left(\frac{m_{Cl_2}}{V_{Cl_2}} \right) \right]}{(\mu_l/\rho_l)^2 \rho_l} \qquad \text{3.2.32}$$

where L_c is the characteristic anode length, frequently chosen as the vertical distance where buoyancy occurs [64].

3.3 Results and discussion.

In this section, validation results are first analyzed. The main contributions are then presented, such as the impact of important phenomena, including fluid dynamic effects at the electrodes and chemical recombination of the reaction products, all of which impact the energy performance of the electrochemical cell. Some general assumptions are made as follows: 1. No-slip conditions on all wall surfaces, 2. The detachment of contact angle is taken as $\phi = 23°$, a

value also used by Zhang and Zeng (2010-12) to represent the dynamic of bubbles, 3. Assuming a rapid reaction between Cl_2 and Li, the quantity of recombined lithium is determined from the mass flux of liquid lithium to the anode domain.

3.3.1 Geometry mesh validation.

Cell geometry arrangement greatly influences the fluid dynamics, which in turn strongly affects the recombination of the products inside the electrochemical cell. The different boundary conditions are shown in Table 3.5.

Table 3.5. Domain and boundary conditions parameters.

	Boundary conditions		Phenomena		
			TCD	Mass Transfer	Fluid Dynamics
	1	Symmetry Axis	*Insulated*	$dNi/dr = 0$	$dv_r/dr = 0$ $dv_z/dr = 0$
	2	Anode Surface	$i{=}7800$ A/m^2	$-Ni = i/(zF)$	$\dot{m}_{Cl2\,(in)}$
	3				
	4	Anode Outlet	*Insulated*	$dNi/dt ={-}m_{out}$	$(\rho.v_{out}.A)_{Cl_2}$ $= -\dot{m}_{Cl_2(out)}$
	5	Diaphragm		*Insulated*	
	6				
	7	Cathode Outlet	*Insulated*	$dNi/dt ={-}m_{out}$	$(\rho.v_{out}.A)_{Li}$ $= -\dot{m}_{Li_{(out)}}$
	8	Cathode Surface	$\Phi{=}0\ V$	$-n\ Ni = i/zF$	$(\rho.v_{in}.A)_{Li}$ $= \dot{m}_{Li_{(in)}}$

The inter-domain boundary (boundary 9 and 10) allows the separation between the anode and cathode domains which helps in the analysis of the results, more specifically the post-processing of the velocity profiles induced by the bubbles and lithium liquid drops. The three domains (D_1, D_2 and D_3) were used to validate the mesh. The anode and cathode surfaces were evaluated with six different types of mesh, which are described in Table 3.6.

Table 3.6. Mesh with different element sizes as predefined by Comsol®.

Element sizes	Coarser	Coarse	Normal	Fine	Finer	Extra fine
Maximum (m)	0.00661	0.00509	0.00342	0.00266	0.00213	9.88e-4
Minimum (m)	3.04e-4	2.28e-4	1.52e-4	7.6e-5	3.04e-5	1.14e-5
Density (Elem./m³)	1.20e6	1.488e6	1.956e6	2.288e6	2.834e6	5.032e6

Fig. 3.5 is showing the prediction of the cell potential obtained with different mesh sizes. The validation of electrochemical results is based on Oliaii et al. (2017-18) using an anode-cathode distance (ACD) of 0.0635 m with a mesh density of 6.98e6 Elem./m³. Results obtained by Oliaii et al. (2017) are similar although a difference in the cell voltage magnitude was found due to the approach used to represent the additional resistance caused by the anode bubble layer. On the other hand, the predicted cell voltage in the present research is in the $8 - 9\ V$ range, a result also reported by Lovering (1982).
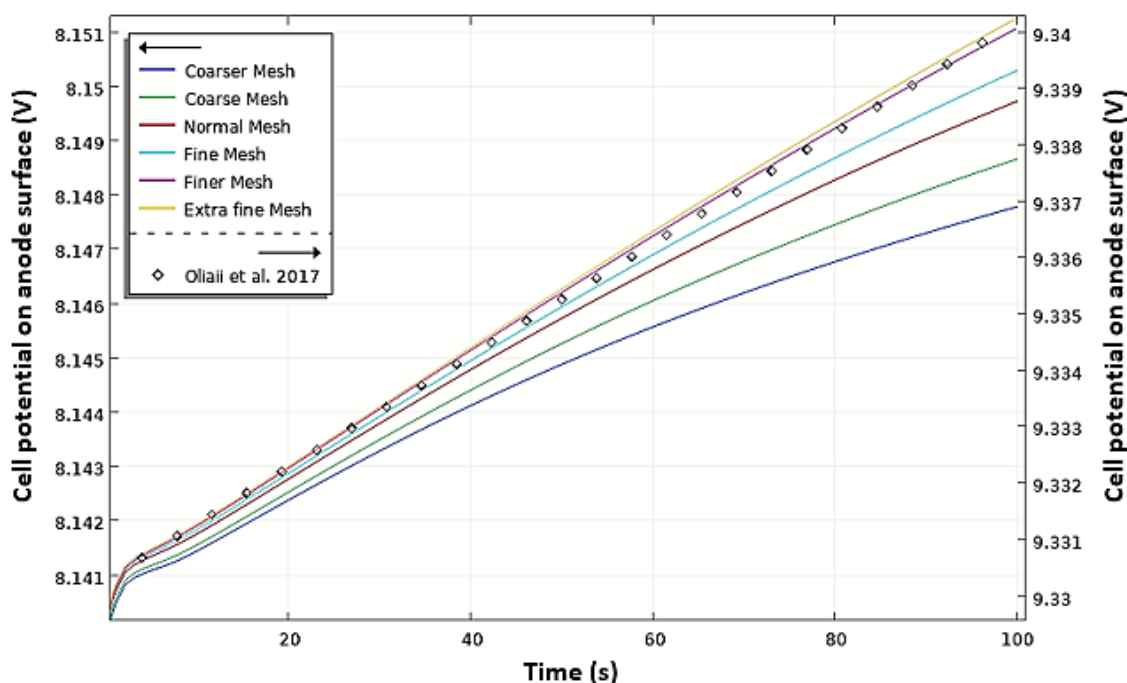
Fig. 3.5 Mesh validation to different mesh sizes.

3.3.2 Electrochemical Validation

In Fig. 3.6, one can observe the current density distribution on the electrodes. At the anode, a rapid decrease of the current density with height is caused by the diaphragm, which is acting as an insulator, a barrier for the passage of the ions between anode and cathode. The effect of the diaphragm is also seen at the cathode, the peak is the current distribution corresponding to the tip of the diaphragm. The similarity between the current distribution obtained in this work with the results presented by Oliaii et al. (2017-18) indicates that the effect of the bubble resistance layer is limited. It also shows that there is no significant difference between considering the diaphragm as an insulation wall or as a porous material, as simulated by Oliaii et al. (2017-18). It can be concluded that the current transport through the diaphragm is low with respect the current transport by migration and diffusion in the main body of the solution.
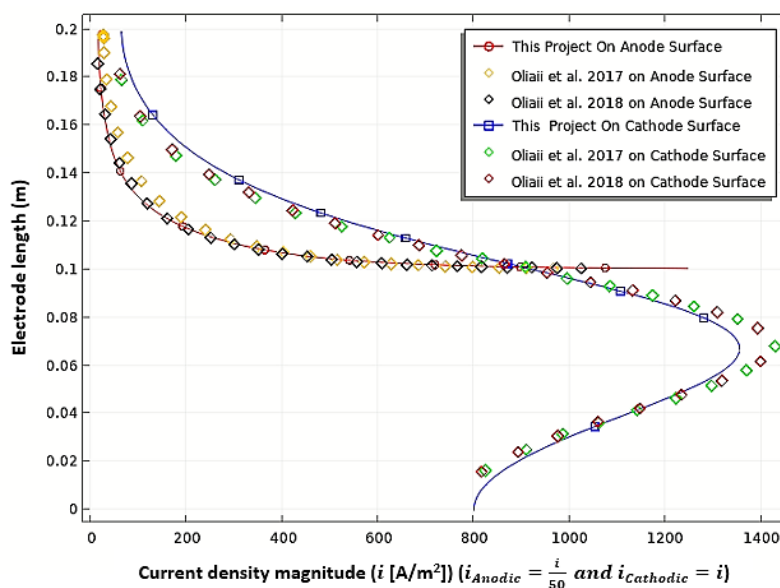
Fig. 3.6 Current density distribution on the cathode and anode surfaces.

3.3.3 Mass Transfer Validation

Fig. 3.7 is showing the consumption of ions (in %) as a function of time, which represents a global validation of mass conservation in the electrochemical reactor. As expected, K^+ ions are conserved, this species being electro-inactive. The 1:1 stoichiometry of the electrochemical reactions involving Li^+ and Cl^- ions and their initial concentrations explain the ratio of about 3/2 between the Li^+ and the Cl^- consumptions (in %). Moreover, the linear relationship of the Li^+ and Cl^- concentration curves with time represents the constant rate of the electrochemical reaction, no surprise since the imposed current density is constant and fixed to 7800 A/m^2.
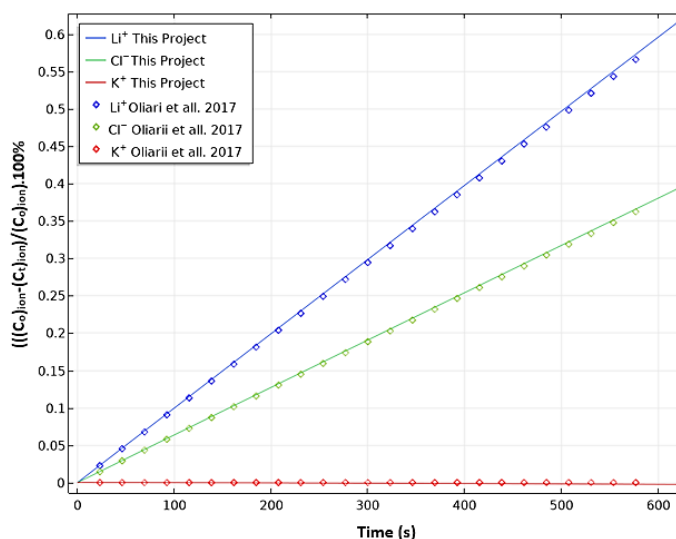
Fig. 3.7 Percentage of mole consumed over time for different ions in the cell.

3.3.4 Fluid Dynamic Validation

As proposed by Oliaii et al. (2017), Litrico et al. (2018) and Zhao et al. (2020), a $k - \varepsilon$ turbulence model with no-slip conditions is used to represent the fluid dynamics and to compute the fluid viscous stresses. The Cl_2 and metallic Li volume fractions near the anode and cathode surface respectively at the beginning of the electrolysis ($t = 0.5\,s$) are represented on the left pane of Fig. 3.8. This time has been chosen to illustrate the behaviour of the species at the start-up, before the accumulation of bubbles in the anode zone. It shows that the bubble volume fraction is higher at the bottom of the anode, a consequence of higher current densities at this location. Note that at 0.5 s, no chlorine accumulation is yet observed at the top of the cell. On the other side, at the cathode surface, higher lithium production is observed at the vertical position of the diaphragm ($z = 0.07\,m$) where the cathodic current density magnitude is highest.

Now the velocity profiles shown on the right pane can be explained by the effect of the diaphragm on the fluid dynamics, a similar result obtained by Oliaii et al. (2017). The diaphragm separates the cell into two regions, an anodic and a cathodic compartment, where the momentum is respectively produced by the Cl_2 bubbles and by the liquid Li drops movement to the top of the cell. As seen in Fig. 3.8, the highest velocity profile is located close to the corner of the anode, due to the magnitude of the current density at this particular point and the importance of buoyancy forces created by the gas and electrolytic solution density differences.
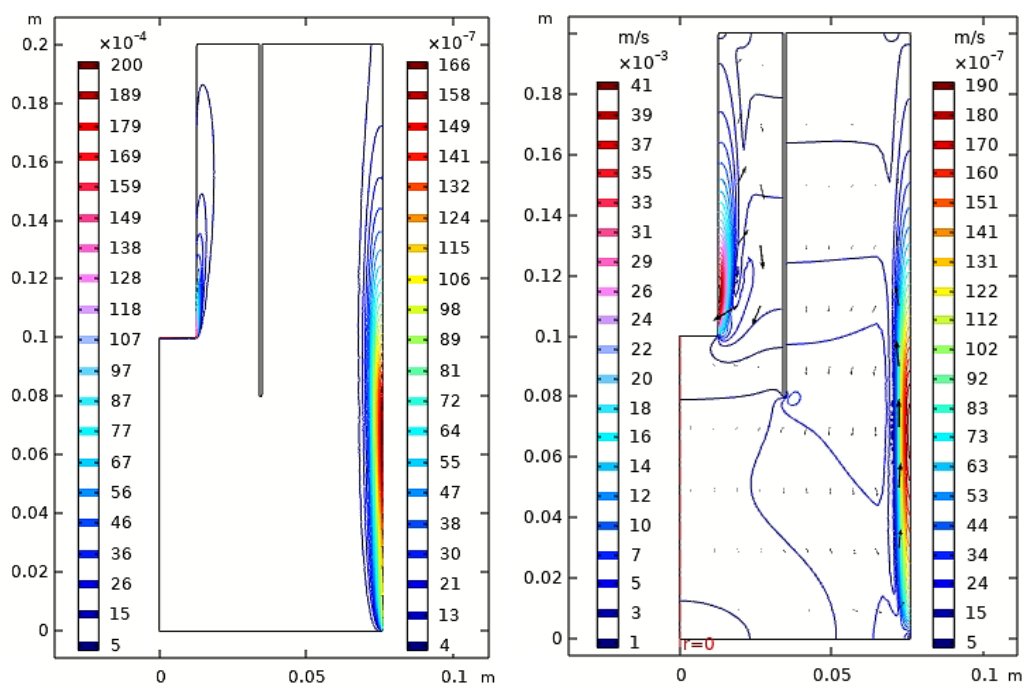
Fig. 3.8 Cl_2 bubbles and Li liquid drops volume fractions (left) and velocity profiles (right) at 0.5 s.

The momentum equation depends on the amount of chlorine bubble produced on the anode surface, which is determined by the bubble number density (n) and its mass flow rate. The velocity and gas volume fraction magnitude presented in this section were nondimensionalized to facilitate the comparison with literature results. Fig. 3.9 shows the gas volume fraction as a function of the adimensionalized distance to the anode, at different heights. The thickness of the uprising gas layer, estimated by $\delta_{max} = r_{max} - r_{min} = 5.3\ mm$, the difference between the position of the gas boundary and the position of the anode, is used to get dimensionless results that were compared to results obtained by El-Askary et al. (2015) and by Riegel et al. (1998).

In Fig. 3.9, one can observe the bubble volume fraction increases with the anode height, an expected behavior considering bubbles accumulation at the top of the reactor. At steady state, Riegel et al. (1998) experimental data and El-Askary et al. (2015) turbulent simulation results both show that gas volume fraction goes to zero outside of boundary layer, a prediction also obtained our model. This behavior can be explained because of the importance of the kinetic energy in turbulent dynamic flows causing a rapid outflow of the electrolytic solution. Conversely, in laminar flows, the bubble is more uniformly distributed along the r axis due to their lower kinetic energy. Moreover, gas volume fractions at $z = 40\ mm$ and $z = 80\ mm$ are closer to Riegel et al. (1998) experimental data, which shows that the thickness of the gas layer formed along the anode surface reaches its stationary state.
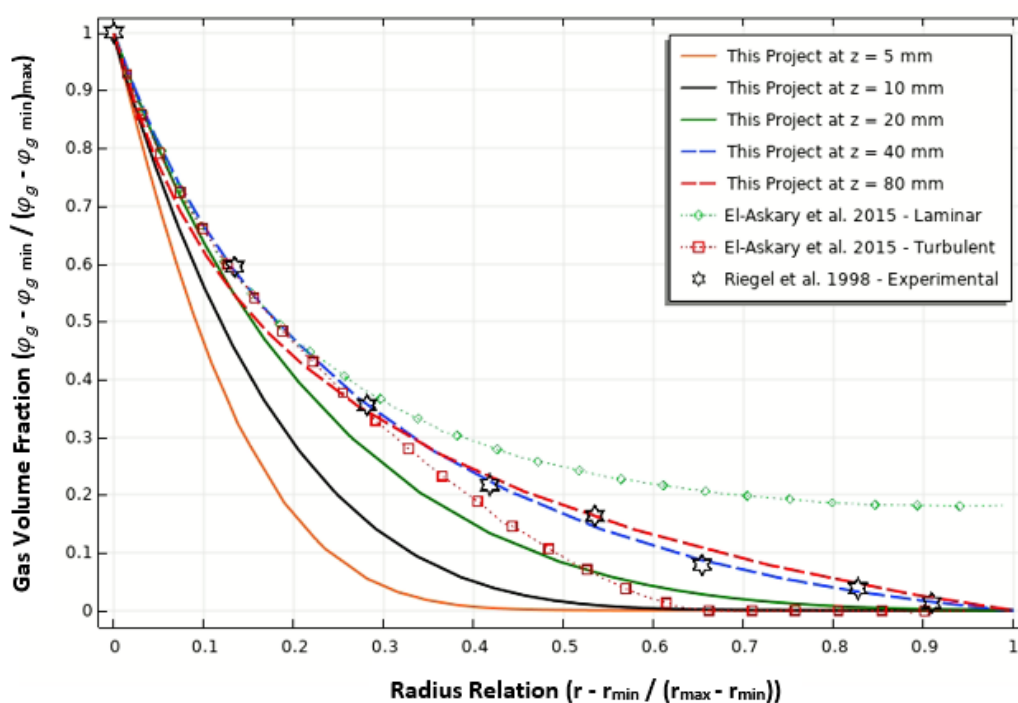
Fig. 3.9 Gas volume fraction at different heights after 600 s.

In Fig. 3.10, the bubble velocity predicted in this work was compared to the results obtained by Takamure et al. (2020) and by Pan et al. (2020). In both research works, the gas injection

system was located at the center of their experimental setup. Their data were taken from the center of each gas injection system to the wall of the reactor or tank. The velocity was taken at different heights of the vessel, from the bottom to the top. Pan et al. (2020) also studied bubble fluid dynamics with $k - \varepsilon$ turbulence model using a no-slip velocity condition. Fig. 3.10, furthermore shows the velocity bubble profile obtained at $z = 10$ and $20\ mm$ after 600 s, a time sufficient to reach the steady-state condition. The gas velocity behavior for both heights ($z = 10$ and $20\ mm$) is highest at the anode surface. After that, the velocity begins to decrease asymptotically as the radius increases.
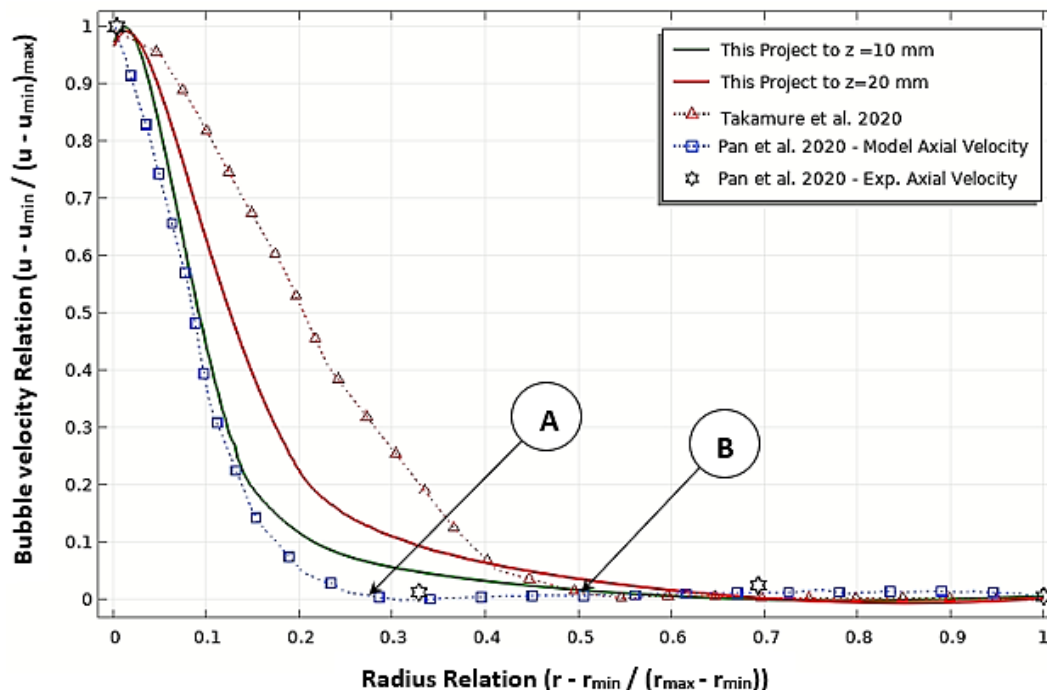
Fig. 3.10 Bubble velocity validation.

Points A and B indicate the radial position where the gaseous phase velocity is zero in Pan et al. and Takamure et al. respectively. The difference between those points is most probably a consequence of their different gas injection configurations. The result at $z = 10\ mm$ fit very well to Pan et al. experimental and modeling results. It can also be observed that as the height increases ($z = 20\ mm$), the behavior of the velocity ratio obtained in this work approaches the results of the velocity ratio obtained by Takamure et al., consistent with the fact that the result reported by Takamure et al. were taken at higher values on the z-axis

3.3.5 Contributions of this research

Relying on the validation of the model developed in this work, this section presents the original results of this research. To the knowledge of the authors, it is the first time that cell design and operating conditions are studied with their impact on the recombination of Cl_2 and

Li through back reactions ($m_{Li}^{Recombined} = \varphi_{Li}^{D_2} \, m_{Total}^{D_2}(\rho_{Li_{(Liq)}}/\rho_l)$), as well as the fluid dynamics induced by lithium drops in the electrolytic cell.

3.3.5.1 Characterization of electrolyte fluid dynamics

The momentum transfer in the electrolytic solution is caused by natural convection driven by the bubbles upward movement. Therefore, the Grashof number best characterizes the type of flow in the anode domain. It was taken that the density changes depend on the electrolytic reaction as well as on the gas produced. Fig. 3.11 shows the behavior of the Grashof number with respect to the reaction time. The decreasing behavior of the Grashof number is caused by the consumption of Cl^- and Li^+ ions from the electrolyte solution during the reaction, inducing a density decrease of the liquid electrolyte with time.
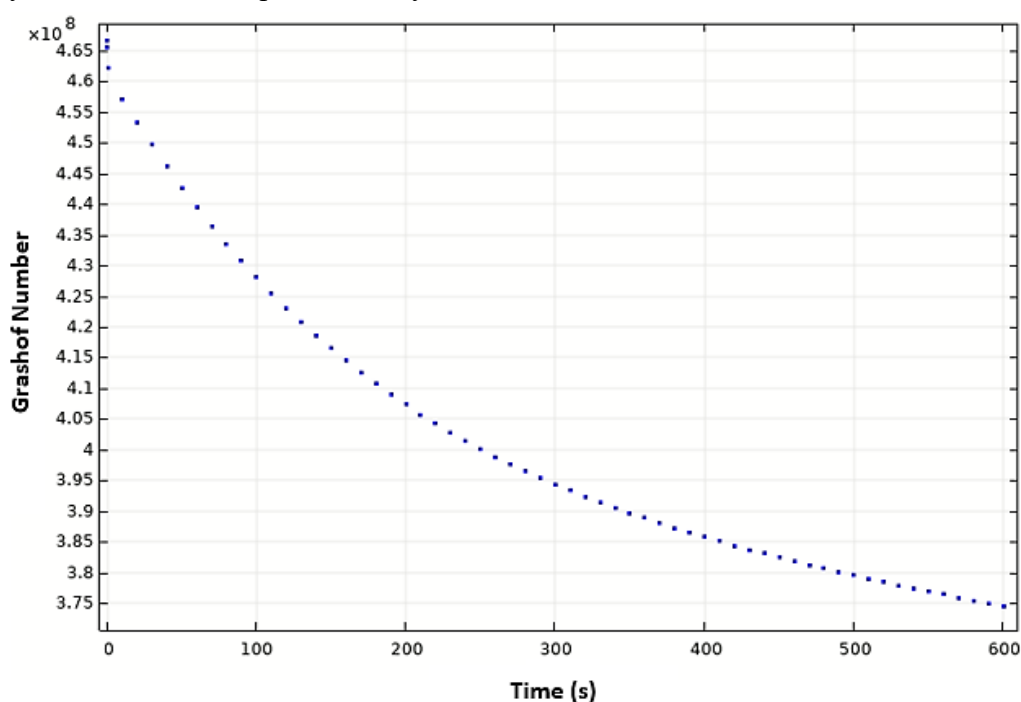
Fig. 3.11 The evolution of Grashof number with time in the D$_2$ domain.

It can also be observed that at 600 s, the Grashof number gets to an asymptotic value close to $3.74x10^8$, which indicates that the flow reached a steady state and can be considered as turbulent.

Fig. 3.12 illustrates the average velocity evolution for the liquid and gas phases. The steady state regime is reached at 600 s with an average gas velocity of $0.36 \, m/s$, Oliaii et al. (2017) has reported a relative value of $0.29 \, m/s$. The average velocity of the electrolyte solution reaches a value of $0.22 \, m/s$. The gas volume fraction in the electrolytic cell reached a value of 0.1 in the steady stated of fluid dynamic.
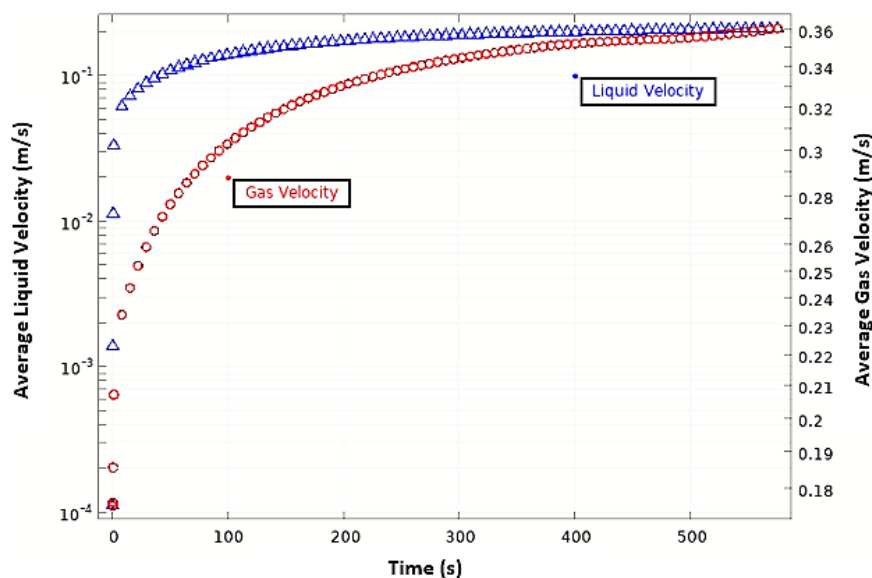
Fig. 3.12 The gas and liquid velocity vs time in the D$_2$ domain.

3.3.5.2   Bubble overpotential

Fig. 3.13 shows the evolution of the average ohmic voltage drop in the electrolyte (η_{Ohm}) and the sum of anodic overpotential (η_{An}), equilibrium potential (E_{eq}) and the bubble overpotential (η_{Bub}). The predicted potential of the electrolytic solution increases almost linearly with the volume fraction of chlorine gas. The anodic overpotential behavior is not linear due to the resistance of the bubbles formed on the anode surface. The sum of both values at steady state results in a total potential of $8.72\ V$ also reported by Lovering (1982).
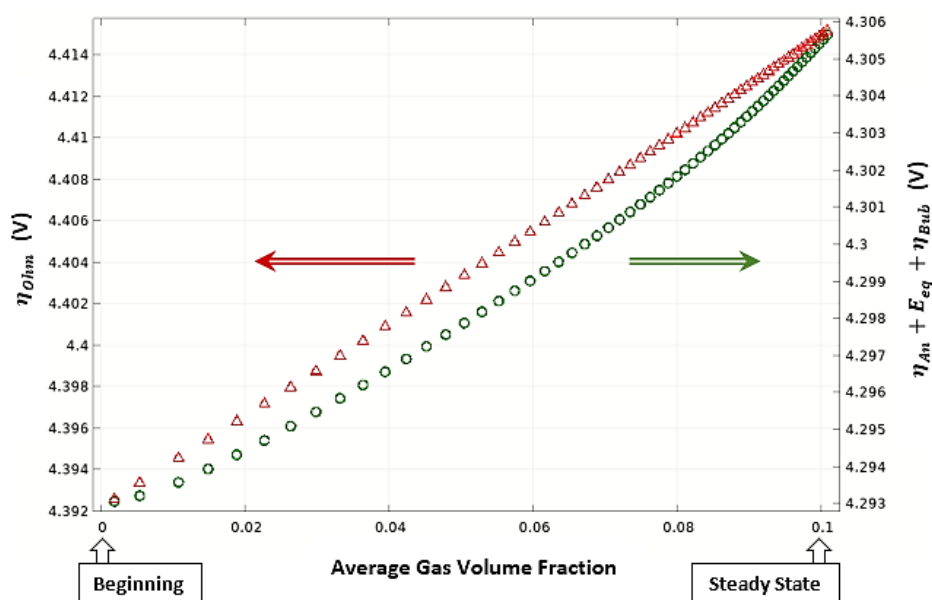
Fig. 3.13 Potential with as volume fraction relation at 600 s.

3.3.5.3 Cathode fluid dynamics

Lovering (1982) underlined the importance of using a diaphragm to avoid the recombination of the products inside a lithium electrolytic cell. In this simulation, it takes the form of a non porous smooth flat surface that is located in the anode-cathode gap and extends below the bottom of the anode. On the other hand, Oliaii et al. (2017-18) reported a higher energy consumption needed in such configurations due to a higher ACD, although neglecting the influence of the velocity field in the cathode domain.

 Another problem related to the fluid dynamics of such a cell can be illustrated with the model developed in this research work. The liquid Li upward movement is responsible for a recirculation zone in the cathode domains (D_1 and D_3 in Table 3.5), which favors the back reaction between Cl_2 and Li, increasing the energy expenditure. The velocity profiles in the anode (D_2) and cathode domains are shown in the left part of Fig 14. The liquid velocity is higher in the D_2 domain because of the bubble buoyancy, as the density difference between Cl_2 gas and liquid electrolytic is much higher than the difference between liquid Li and electrolyte. However, the momentum produced by the liquid Li drops is enough to create a circular movement in the D_3 domain, which in turn brings Li at the bottom of the anode domain. Lithium in this area is carried by the upward electrolyte flow in D_2 and ends up at the top of the cell, where it accumulates or reacts back to $LiCl$, as shown in Fig. 3.14 at the right.
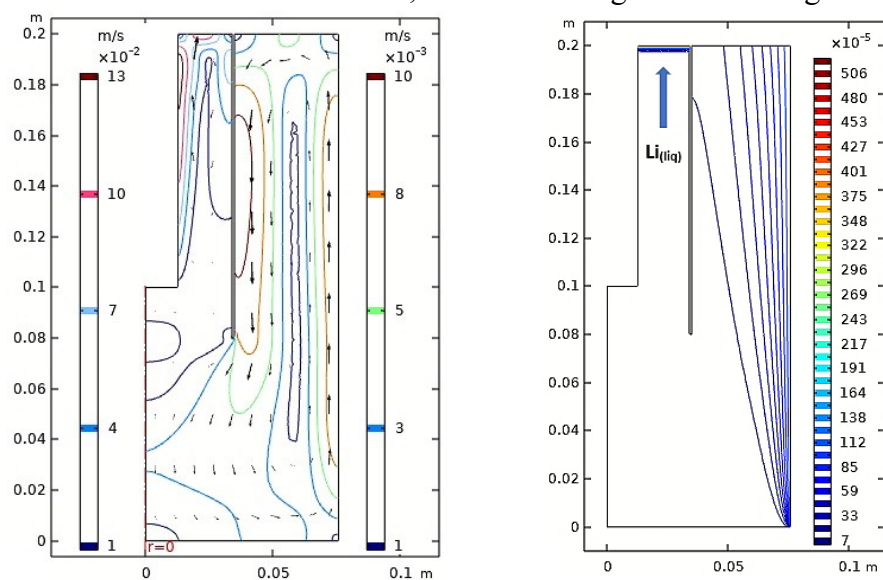
Fig. 3.14 Velocity and lithium liquid phase profiles at 600 s.

Despite the presence of the diaphragm, which should help to avoid Li recombination, the presence of Li in a zone where Cl_2 concentration is highest seems unavoidable, which causes detrimental effects on the energy consumption and yield of the reactor.

Two new configurations of the diaphragm were proposed and evaluated in order to analyze the influence of the cathode fluid dynamics on the amount of recombined lithium and energy consumption. As shown in the of Fig. 3.15: 1) a conical configuration with a bottom

diaphragm radius (R_{DB}) of 39 mm, designated as the configuration > 90° (left), and 2) with $R_{DB} = 29\ mm$, designated as the configuration < 90° (right). To optimize the fluid dynamics of the cathode domain, a small baffle was also added at the bottom of the electrolytic cell at a fixed position: 10 mm high and with a distance of 10 mm between the two points of the baffle base.

In the Fig. 3.15 the fluid dynamics of anode and cathode domain is shown in steady state. The bubble and Li liquid drop velocity vectors (black arrows) are also indicated. All diaphragm configurations have a circular movement in the anode (D_2) and cathode (D_1) domains, caused by the bubbles and liquid drops velocities. Furthermore, an important swirl is found at the inter-domain boundary 9 (Table 3.5) as consequence of the coupling of the fluid dynamics of the anode and cathode. The swirl size for the configuration > 90° is the biggest, followed by the configuration = 90° and finally by < 90°.
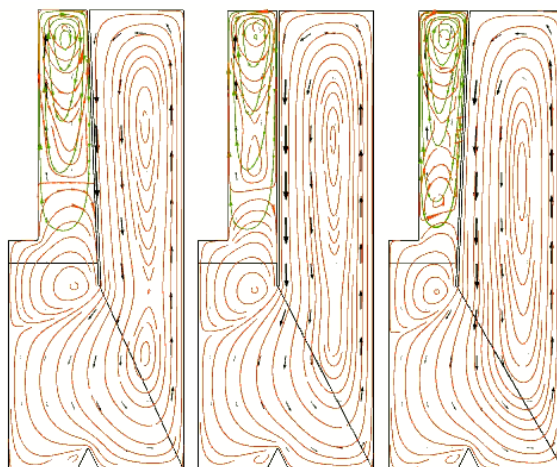
Fig. 3.15 The 3 different diaphragm configurations with their bubbles (green) and Li drops (orange) streamlines at 600 s.

The cathode electrolyte average velocity of Fig. 3.16 was computed in the domain D_3, a region that relates the cathode domain (D_1) to the anode domain (D_2). According to Fig. 3.16, the electrolyte velocity increases with time for all electrolytic cell configurations. Comparing configurations with diaphragm at 90° without and with baffle, we found that the baffle at the bottom of the cell reduces the velocity from 0.0034 m/s to 0.0028 m/s in the domain D_3. The conical configuration > 90° has the lowest velocity of the three configurations analysed, followed by the configuration = 90° and finally by < 90°.

The momentum of the electrolytic solution in the cathode domain (D_1 and D_3) is produced by the upward movement of the lithium droplets to the cell surface. The difference in momentum is solely produced by the different angles of inclination in the diaphragm, which induces a pressure difference between the top and bottom. As a qualitative example, the volumetric flow of lithium (Q_1, Q_2, and Q_3) for the > 90° configuration is described in the upper

left of Fig. 3.16, where it can be observed that the amount of electrolyte movement in the upper region of the cathode (Q_2) is higher than in the lower part (Q_3). This occurs because the conical geometry of the diaphragm reduces the transversal area for the lithium droplet flow at its bottom, thus increasing the resistance for momentum transfer. Moreover, the pressure is lower at the top of the diaphragm than at the bottom. These two conditions make it favorable for an increased amount of movement at the top of the diaphragm. On the other hand, for the $< 90°$ configuration, the situation is reversed. In that case, the geometry produces a lower momentum transfer at the top of the diaphragm and a higher one at the bottom.
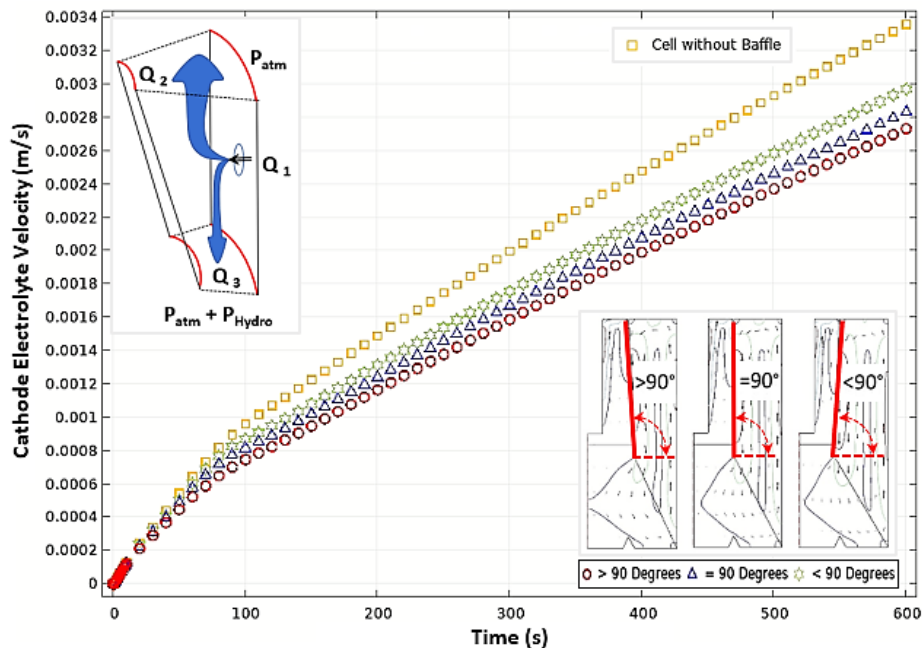
Fig. 3.16 Electrolyte velocity in the cathode domain (D_3).

Using a total current of 60 A during 600 s, the electrochemical simulation yielded a total mass of liquid lithium of 2.87 g. Fig. 3.17 shows that the total production of lithium is a linear function of time, coherent with the global mass balance and Faraday's law.

The amount of lithium recombined as a function of time is also shown for configuration with and without baffle. The small baffle has the effect of redirecting Li to the D_1 domain at the cell bottom thus keeping separate the anode and cathode fluid dynamics. Consequently, this little design modification is responsible for a 7 % reduction in the mass of recombined lithium. The effect of the cathode fluid dynamics on the mass of recombined Li is shown in the upper left of Fig. 3.18. The configuration $> 90°$ was found to present the highest amount of recombined lithium, a consequence of a lower velocity in the D_3 domain. In that region, the buoyant force (f_B) is greater than the drag force (f_D), which causes the lithium droplets to be entrained into the D_2 domain. The configuration $< 90°$ has the lowest Li back reaction with a 77 % less than with configuration $= 90°$, due to the higher velocity of Li droplets. The second effect of the fluid

dynamics on the *Li* recombination is the formation of the eddy between the anode and D₃ domain.
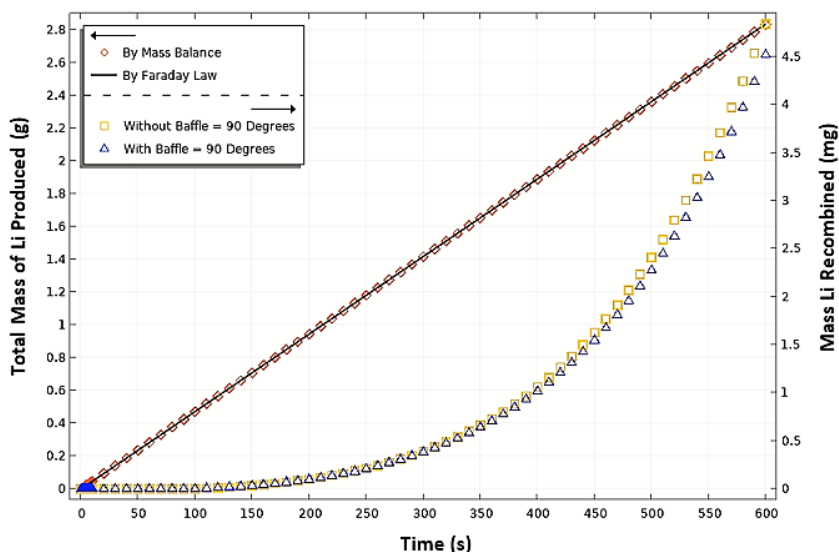
Fig. 3.17 Total mass of *Li* produced and mass of recombined lithium.

As can be seen in Fig. 3.15, the size of the eddy is proportional to the increase of the R_{DB} value. The eddy with the larger size increases the possibility of the lithium droplets to be entrained to the anode domain.
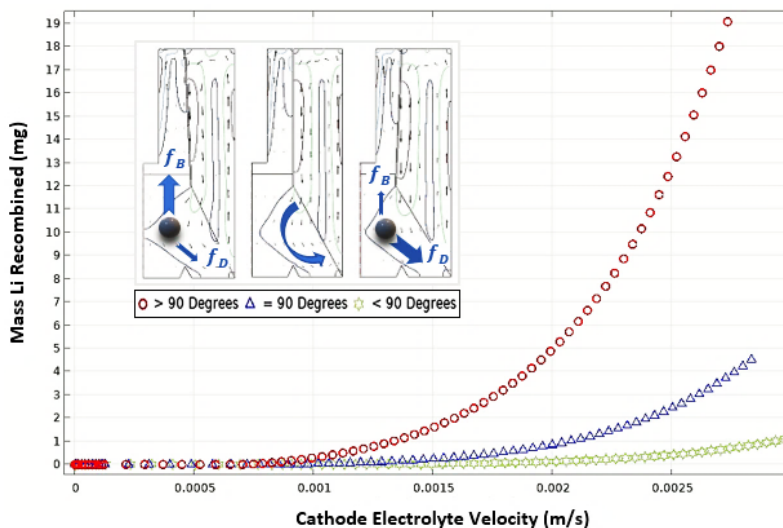
Fig. 3.18 The electrolyte velocity (D₃) vs mass of *Li* recombined.

3.3.5.4 The total cell potential and energy consumed

Fig. 3.19 shows the variation of the total cell potential as a function of time, for each configuration studied. The total cell potential for the configurations with and without baffle at the bottom of the cell is practically the same, the small baffle does not hinder the transfer of ions in the electrolytic solution. On the other hand, the total potential for the > 90° configuration is

the lowest because the resistance of the diaphragm to the transfer of ions is the lowest in that configuration. This angle opens up the view angle between anode and cathode and increases mass transport between electrodes thus reducing the ohmic voltage drop.
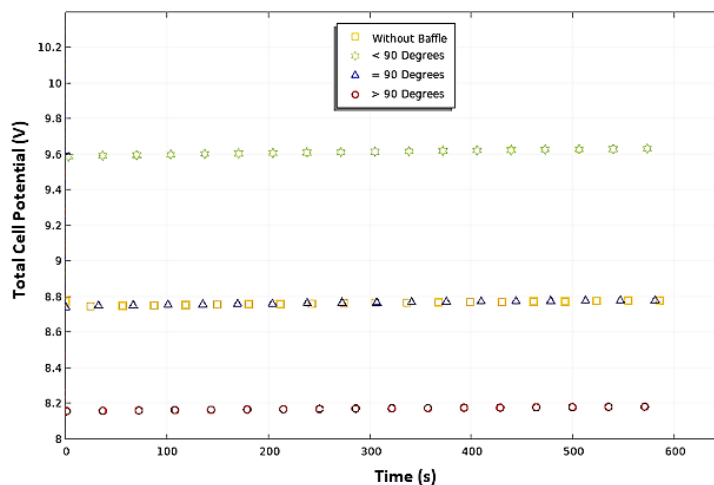
Fig. 3.19 Total cell potential in function of time.

The total energy consumed in the electrolytic cell was computed using the total current and cell potential, divided by the net mass flow of the lithium produced ($E_{cell} \, I_{cell}/(\dot{m}_{Li}^{Total} - \dot{m}_{Li}^{Recombined}$)) [16]. In Fig. 3.20 shows the total specific energy consumption in the process where values of 31, 34, and 37 kWh/kg_{Li} are obtained with each diaphragm configuration. This parameter was also analyzed by Lovering (1982), Sadoway et al. (1998) and Zhao et al. (2020), who obtained values between $31 - 43 \, kWh/kg_{Li}$, which are close to the values estimated with our model. The differences in the energy consumed between each configuration is essentially caused for the total cell potential obtained with the model.
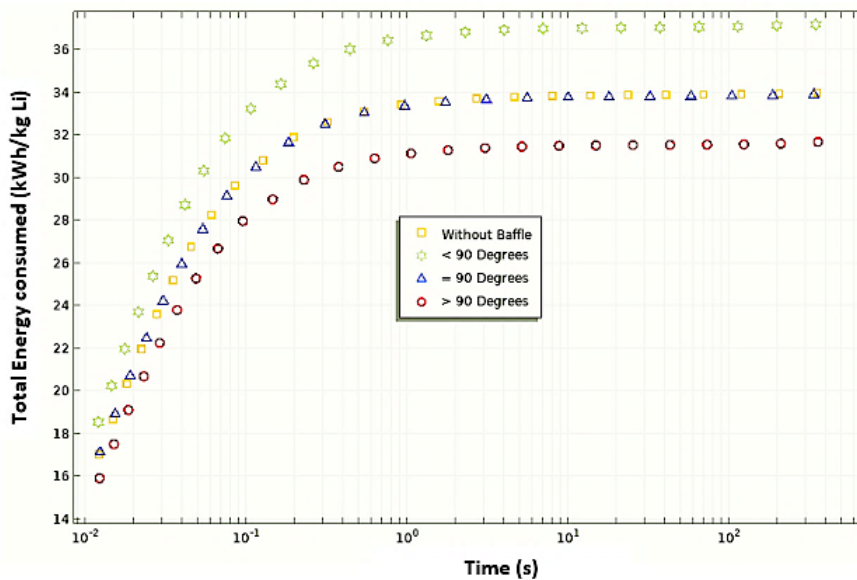
Fig. 3.20 Total energy consumed in the process.

3.4 Acknowledgments

3.5 Conclusion

The authors have presented an original model representing the production of metallic lithium inside a molten salt electrolysis cell. The efficiency of this process, which is the only commercial route to produce this critical and strategic metal in the world's production of energy storage devices, is sensitive to operational parameters and cell design that both impact on energy consumption and lithium production. This new mathematical model includes important and original features such as 1- the prediction of Li liquid drop production and its related fluid dynamics, 2- the prediction of Cl_2 bubbles produced on anode surface. It has been used to study the impact of cell design on fluid dynamics and on Li recombination with Cl_2. Simulations were conducted for a sufficient electrolysis time to reach steady state using a turbulent (k-ε) approach to solve the two-phase flow coupled to the lithium electrolysis process.

This model greatly helps to improve the understanding of basic chemo-physical processes inside the electrolysis cell and reveals the link between anode and cathode fluid dynamics, electrolytic reactions and two phases mass transport. It was used here to show the impact of four cell configurations (diaphragm at 90° with or without bottom baffle, diaphragm at > 90° with bottom baffle, diaphragm at < 90° with bottom baffle) on cathode fluid dynamics and lithium recombination with Cl_2 at the anode. The baffle reduced the amount of recombined lithium by 7 % with no additional energy cost. The diaphragm with an inclination < 90° reduced the total recombined mass by 77 %, although it increased the energy consumption by 10 % with respect to the base case of a vertical diaphragm. This last case illustrates that certain design modifications can lead to a reduction of Li recombination but at a high energy cost. The model can be used to guide industrial producers to optimize their development efforts and identify parameters that lead to improvement of Capex and Opex.

In the future, the authors propose to improve the reliability of the model by predicting the generation of Cl_2 nuclei on the anode surface based on the Classical Nucleation Theory using the local chlorine concentration as predicted by the electrochemical reaction. It would also be interesting to assess the robustness of the model by studying the impact of scaleup (industrial designs) and different flow configurations on the performance of the cell.

CHAPITRE 4 : AVANT-PROPOS

Auteurs et affiliation:

- Juan Manuel Melendez: étudiante au doctorat, Université de Sherbrooke, Faculté de génie, Département de génie chimique et de génie biotechnologique.

- Martin Désilets: professeur, Université de Sherbrooke, Faculté de génie, Département de génie chimique et de génie biotechnologique.

- Gaétan Lantagne: professeur associé, Université de Sherbrooke, Faculté de génie, Département de génie chimique et de génie biotechnologique.

Titre français: Réduction de la consommation d'énergie dans les cellules électrolytiques au lithium en améliorant la conception et les conditions de fonctionnement.

Contribution au document:

Les contributions de cet article sont : la simulation de la résistance au transfert de masse et de courant dans la couche limite, au moyen du développement mathématique d'une équation empirique qui dépend de la fraction volumique du chlore gazeux; l'effet de l'inclinaison d'un diaphragme avec rainure sur la recombinaison du lithium métalique et sur la consommation d'énergie du processus; et enfin, l'effet de rotation de la surface de l'anode et de la cathode sur les paramètres de recombinaison et sur la consommation d'énergie.

Résumé français

L'électrolyse en sels fondus est un procédé efficace pour obtenir du lithium métallique, mais nécessite une quantité considérable d'énergie. L'utilisation d'un diaphragme rainuré et d'électrodes rotatives a été étudiée, à travers l'utilisation d'un modèle numérique avancé représentant une cellule d'électrolyse du lithium expérimentale avec pour finalité de réduire l'énergie requise. Les simulations ont été menées en utilisant un modèle turbulent (k-ε) pour résoudre l'écoulement biphasique, couplé au transport de masse transitoire à l'intérieur d'une cellule d'électrolyse axisymétrique 2D. Le diaphragme vertical avec rainures permet une

réduction de 26,7 % de la consommation d'énergie par rapport à la conception sans rainures, mais augmente de quatre fois la quantité de lithium recombiné dans le processus. Pour diminuer cette recombinaison, le diaphragme rainuré a été incliné vers l'anode. Un angle vertical de 85° permet de réduire la consommation d'énergie de 23,5 %, avec approximativement la même masse de lithium recombiné par rapport à la conception verticale non rainurée. L'utilisation d'une cathode rotative à une vitesse angulaire de 0,25 rad/s entraîne une diminution de 40 % de la consommation d'énergie, ainsi qu'une diminution de 87,4 % de la reconversion du lithium métallique, par rapport à la conception de diaphragme non rainuré non poreux.

4 Article 2: Reduction of Energy Consumption in Lithium Electrolytic Cell by Improving Design and Operating Conditions

Juan Manuel Meléndez, Martin Désilets and Gaétan Lantagne

Sherbrooke University, Chemical Engineering Department, 2500 Boul. de l'Université Sherbrooke (Québec) J1K 2R1, E-mail juan.manuel.melendez@usherbrooke.ca.

Abstract. Molten salt electrolysis is an efficient process to obtain metallic lithium but requires a considerable amount of energy. The use of a grooved diaphragm and rotating electrodes were studied using an advanced numerical model representing an experimental lithium electrolytic cell with the finality to reduce the required energy. Simulations were conducted using a turbulent (k-ε) model to solve the two-phase flow coupled to the transient mass transport inside a 2D axisymmetric electrolysis cell. The model also considers the recombination of Li with chlorine gas (Cl_2), a backreaction that is detrimental to efficiency and energy consumption. The vertical diaphragm with grooves produces a reduction of 26.7 % in energy consumption in comparison with the ungrooved design but increases by four times the amount of recombined lithium in the process. To decrease that recombination, the grooved diaphragm was inclined toward the anode. A vertical angle of 85° helps to reduce the energy consumption by 23.5 % with approximately the same recombined lithium mass when compared to the vertical ungrooved design. The use of a rotating cathode with at an angular velocity of 0.25 rad/s results in a 40 % decrease in energy consumption in addition to a decrease of 87.4 % in metallic Li reconversion, in comparison with non-porous ungrooved diaphragm design.

Keywords: Grooved diaphragm, rotating electrodes, anode and cathode fluid dynamics, recombined lithium, total energy consumption.

4.1 Introduction

According to the Conference of the Parties (COP26), the world needs to rapidly replace fossil fuel with clean energy to reduce the amount of CO_2 in the atmosphere and thus reduce global warming [1]. One of the main sources of CO_2 emissions are internal combustion engines (ICE) vehicles, which are being replaced by electric vehicles (EVs). However, the substitution has been difficult due to the limitations and problems caused by the storage of electric energy. On one hand, the battery with the highest storage capacity is the lithium ion. On the other hand, this technology is dangerous because of the use of flammable electrolyte apart from lithium iron phosphate batteries which are inherently safe [2]. A solution to this problem is to develop solid-state batteries (SSBs), where the anode is composed of metallic lithium. Furthermore, the SSBs can achieve a volumetric energy density up to 70 % greater than today's lithium-ion batteries

that use conventional graphite anodes, making them the ideal batteries for future EVs [2]–[4]. One advantage of SSBs is that they do not require expensive cooling systems due to the absence of a flammable electrolyte. They have displayed better functionality at higher temperatures due to the increased conductivity of the electrolyte. Placke et al. (2017) have predicted that the current lithium-ion batteries could reach a maximum energy density of 300 Wh/kg after 2025, while metallic lithium SSBs would reach a maximum of 480 Wh/kg [5]. In 2021, St-Onge et al. have developed improved lithium SSBs, proving that batteries of the same size could contain much more energy in the future [6].

From the above considerations, it is important to produce solid lithium with environment-friendly processes where energy usage can be optimized. Amouzegar et al. (1996) studied the production of metallic lithium from the molten salts using an experimental electrolytic cell (EEC) [7], based on the following electrochemical reactions:

$$\text{Anode (Oxidation): } 2Cl^- \rightleftharpoons Cl_{2\,(g)} + 2e^-$$

$$\text{Cathode (Reduction): } 2Li^+ + 2e^- \rightleftharpoons 2Li_{(l)}$$

$$\text{Total Reaction: } 2Li^+ + 2Cl^- \rightleftharpoons 2Li_{(l)} + Cl_{2\,(g)}$$
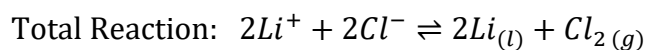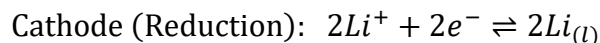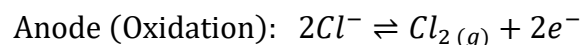
The design of such EEC was developed by Hydro-Quebec (see Fig. 4.1), and it was partially simulated by Oliaii et al. (2017-18) and Litrico et al. (2018) [8]–[10]. They all have taken into account the detrimental effect of chlorine bubble production that brings an additional resistance to the mass and charge transfer taking place in the electrolyte solution and limits the electrochemical reactions on the anode surface. Recently, Melendez et al. (2022) studied the effects of chlorine bubbles and liquid lithium fluid dynamics on the recombined lithium mass and the energy consumption[40]. They used an electrolytic cell with a non-porous diaphragm, with the particular interest to develop new designs for efficient production of lithium with industrial applications. Previous studies have shown that the effect of mass transfer across the anodic boundary layer, where Cl2 is produced, has to be improved in order to optimize the electrolytic cell.

Vogt et al. (1983-2017) have developed several empirical equations to relate the boundary layer thickness to electrochemical parameters like local current density, while Liu et al. (2015) have defined the thickness layer using linear approximations [35], [66]–[68]. Oliaii et al. (2017-18) have simulated the behaviour of a lithium electrolysis cell using an empirical equation to represent the electrolyte film resistance assuming a constant boundary layer thickness. On the other hand, Riegel et al. (1998) measured experimentally the boundary thickness inside a water electrolysis cell in steady state for turbulent and laminar regimes. These data were used by Melendez et al. (2022) to further study the anodic boundary layer thickness in their steady-state fluid dynamics model.

The previous studies have also shown that the management of lithium droplets circulation flow inside the cell is paramount to reducing lithium loss by recombination reactions. However, this has to be done with the lowest possible energy consumption.
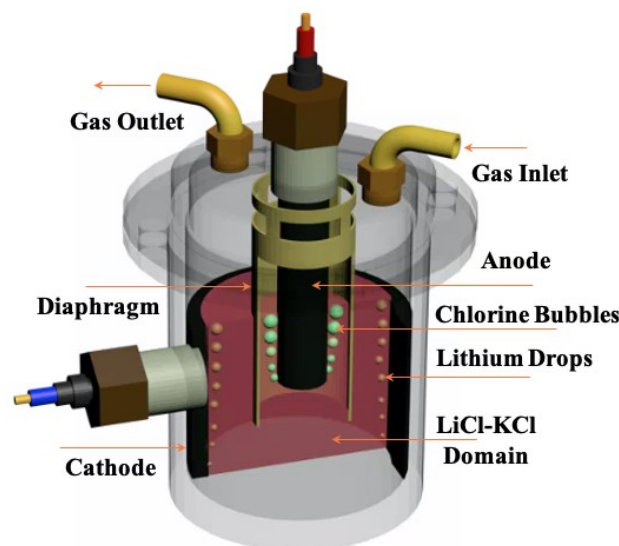
Fig. 4.1 Experimental lithium electrolytic cell.

Introducing a well-designed barrier such as an inclined grooved diaphragm and assessing the use of a rotating electrode (cathode) are innovative ways to achieve both targets: reducing recombination reaction and optimizing the energy consumption for a specific production level.

As such, the main objectives of this research work are:

1- to improve the prediction of the anodic film resistance due to the transient electrochemical production of chlorine bubbles.
2- to analyze the impact of the diaphragm design (grooved diaphragm);
3- to study the impact of specific operating conditions like rotating electrodes on the lithium production and its specific energy consumption.

The grooved diaphragm design presented below decrease the amount of energy consumed by improving mass transfer namely the migration transport mechanism. Furthermore, it separates the anolyte and catholyte fluid dynamics reducing the recombination back reaction between Li and Cl_2. The electrolytic cell with rotating electrodes also presents industrial benefits, reducing the amount of energy consumed and maximizing the mass of lithium produced, mimicking a similar technology used in water electrolysis [69]–[72].

This is the first time such results are presented for lithium electrolysis giving detailed information on the specific fluid dynamics related to molten salt electrolysis. In the first part, our contributions on the analysis of electrochemical film resistance will be presented. In the second part, the grooved diaphragm results will be compared with the ungrooved design. Finally, in the last part, a new operation mode using rotating electrodes and its effects on fluid dynamics inside the cell and the resulting energy consumption will be presented. This analysis will be done using an improved model coupling the bubble gas and liquid lithium drop fluid dynamics in the electrolyte solution.

4.2 Numerical Model

The numerical model integrates the most important transport phenomena occurring in each component of the electrolytic cell. All parameters and properties found in the equations describing the model are taken from Melendez et al. (2022). Transient simulations of the lithium electrolysis cell were fixed to 600 s, a period long enough to reach a pseudo steady state regime and were conducted using Comsol Multiphysics®. The temperature and pressure of the system were considered constants at 723 K and 1 atm, respectively.

4.2.1 Geometry

The computational domain is shown in Fig. 4.2, with a description of the main parameters in Table 4.1. The diaphragm is divided into two sections. The limit between the upper ungrooved section and the lower grooved section were taken from the intersection point between 1) the line defining the diaphragm and 2) a line drawn from the corner of the anode (point A) to the top of the cathode (point B). Six grooves are evenly distributed in the bottom section of the diaphragm.

Fig. 4.2 Computational domain.

Table 4.1. Parameters of the computational domain.

Parameters		
R_{An}	12.7 mm	Anode Radius
GH	1 to 4 = 0.5 mm, 5 and 6 = 1 mm	Groove Height
RB	34 mm (90°), 29 mm (87°) and 25 mm (85°)	Bottom Radius
GT	1 mm	Groove Thickness
BH	10 mm	Baffle Height
L_1	21.3 mm	Length
L_2	78 mm	Length
BB	10 mm	Baffle Base

The insertion of Fig 4.2 is showing the details of the last three grooves of the diaphragm, which have been designed to optimize the specific energy consumption. Due to their lower vertical location, the last 2 grooves have been enlarged to improve mass transport in this zone where liquid lithium droplets are found in lower concentration. This project was carried out with a constant diaphragm thickness (GT) of 1 mm. The inclination angle of the diaphragm (β)

changes according to the value of the bottom radius (RB). The diaphragm was removed from the geometry for the rotating electrodes simulations.

4.2.2 Anodic phenomena

Phenomena simulated on the anode surface are shown in Fig. 4.3. The current density was calculated using a Tafel equation that takes into account the effect of bubble coverage. Consequently, the volume fraction of gas produced on the surface and in the electrolyte was simulated. Finally, the film resistance was linked to the transient amount of gas produced by the oxidation reaction.
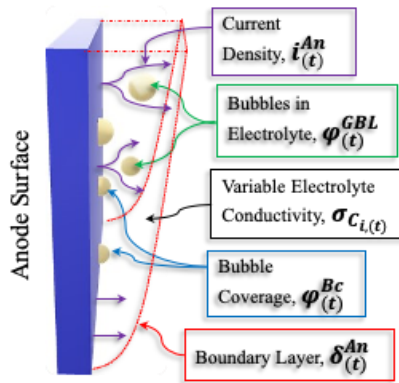
Fig. 4.3 Phenomena simulated characterizing the electrochemical film resistance.

The electrochemical reaction starts when a current density of 7800 A/m² is applied to the anode surface. The simplified Butler-Volmer equation (Eq. 4.2.1) defines the reaction kinetics including a bubble coverage, $\varphi_{(t)}^{Bc}$. In such a multiphase electrolytic system, the bubbles create a hyperpolarization caused by a reduction of the effective electrolytic surface, $(1 - \varphi_{(t)}^{Bc})$ being the only fraction available for electrochemical reactions.

$$i_{(t)}^{An} = i_{o\,An}\,(1 - \varphi_{(t)}^{Bc})\,\exp\left(\frac{\alpha_{An}.\,F}{R.\,T}\,\eta_{(t)}^{An}\right) \qquad 4.2.1$$

where $\mathbf{i_{o\,An}} = \mathbf{10\ A/m^2}$ is the anodic exchange current density and $\boldsymbol{\eta_{(t)}^{Bc}}$ the anodic overpotential. When the reaction begins, the concentration of chlorine ion ($\boldsymbol{Cl^-}$) decreases in the electrolyte solution. The variation in the $\boldsymbol{Cl^-}$ concentration allows the estimation of the mass of chlorine gas produced at each instant of time, which enables to compute the total volume fraction of gas in the solution.

$$\varphi_{(t)}^{gas} = \frac{m_{(t)}^{Cl_2}}{m_{Sol}}\,\frac{\rho_{Sol}}{\rho_{Cl_2}} \quad \text{where } m_{(t)}^{Cl_2} = \left[\frac{1}{2}\left(C_o^{Cl^-} - C_{(t)}^{Cl^-}\right)\right]V_{Sol}\,M_{Cl_2} - m_{Out}^{Cl_2} \qquad 4.2.2$$

where $\boldsymbol{V_{Sol}}$ **is** the volume of the electrolyte solution and $\boldsymbol{m_{Out}^{Cl_2}}$, the outlet mass of chlorine, a value that was calculated from the outlet conditions.

According to the results found by Melendez et al. (2022) and by Oliaii et al. (2017), a new empirical equation was developed to represent the electrochemical film resistance (Eq. 4.2.3). The boundary layer equation ($\delta_{(t)}^{An}$) that forms on the anode is a consequence of the natural convection that occurs due to local chlorine gas production. $\delta_{(t)}^{An}$ is a function of the average gas volume fraction ($\varphi_{(t)}^{GBL}$) in the electrolyte, on the anode surface ($\varphi_{(t)}^{Bc}$) and of the vertical position along the anode (z).

$$\delta_{(t)}^{An} = \left(\varphi_{(t)}^{GBL} + \varphi_{(t)}^{Bc}\right)\left[\left(\frac{1}{6}\right)(z_{An} - z_1) + C\right] \qquad 4.2.3$$

where $z_1 = 0.1\ m$ is the height of the anode, and $C = 34\ mm$ is a constant determined with steady-state fluid dynamics results.

The solution conductivity ($\sigma_{C_{i,(t)}}$) of the boundary layer, is calculated from in Eq. 4.2.4.

$$\sigma_{C_{i,(t)}} = F^2 . \sum_{i=1}^{k}(v_i)^2 . um_{i,(t)} . C_{i,(t)} \quad \text{where} \quad um_{i,(t)} = \frac{D_{i,(t)}}{R.T} \qquad 4.2.4$$

where v_i is the valence of each i species, $um_{i,(t)}$, the ion mobility, $c_{i,(t)}$, the nominal concentration of ions in the cell, $D_{i,(t)}$, the diffusivity. Eq. 4.2.5 is used to estimate the molecular diffusivity, including the effective diffusivity ($D_{i,(t)}^{eff}$), taken from Wilke's correlation which includes the non-ideal effects of the solution, and the turbulent diffusivity component (D_T) [9], [10], [35]. The D_T was taken from the turbulent viscosity of the electrolyte, assuming a Schmidt number equal to one.

$$D_{i,(t)} = D_{i,(t)}^{eff} + D_T \quad \text{where} \quad D_{i,(t)}^{eff} = \frac{1 - x_{i,(t)}}{\sum_{i \neq j}^{i=1} \frac{x_{j,(t)}}{D_{i,j}}} \qquad 4.2.5$$

where the molar fractions of $x_{i,(t)}$ and $x_{j,(t)}$ depends on the nominal concentration of each ion [8], [10], [35].

For simulations conducted with a rotating anode, a constant radial velocity of the moving wall ($V_{\theta\ An}$) is used as represented by the next equation.

$$V_{\theta\ An} = (2\pi)\ r.\text{n} \qquad 4.2.6$$

where n is the angular velocity (rad/s), and r the radius of the rotating surface.

4.2.3 Electrolyte phenomena

The Nernst-Planck equation was used to represent the ions mass transfer inside the electrolytic solution, taking into account the diffusion, migration, and convection transport mechanisms, as shown in Eq. 4.2.7 [8], [32], [57]:

$$i_{(t)} = -F\left(\nabla \sum_i (v_i D_{i,(t)} C_{i,(t)})\right) - F^2 \sum_i (v_i^2 um_{i,(t)} C_{i,(t)}) \nabla \Phi_l + u_{(t)}^l F \sum_i (v_i C_{i,(t)}) \qquad 4.2.7$$

where Φ_l is the potential field and $u_{(t)}^l$ the electrolyte velocity computed from the momentum transfer equation.

In the development of the general momentum transfer, the gas density was neglected as compared to the liquid density. Also, the motion of gas bubbles relative to the liquid was determined by a balance between viscous drag and pressure forces. Additionally, it was assumed that the two phases share the same pressure field. Based on these assumptions, the momentum and continuity equations of the two phases can be combined and the general momentum equation becomes [32], [57], [58]:

$$\rho_l \cdot \frac{\partial \boldsymbol{u}_{(t)}^l}{\partial t} + \rho_l \boldsymbol{u}_{(t)}^l \cdot \nabla \boldsymbol{u}_{(t)}^l = -\nabla \cdot \boldsymbol{p} + \left[\left(\mu_l + \mu_{(t)}^T \right) \left(\nabla \boldsymbol{u}_{(t)}^l + \left(\nabla \boldsymbol{u}_{(t)}^l \right)^T \right) \right] + \varphi_{(t)}^l \rho_l \cdot \boldsymbol{g} + \boldsymbol{F} \qquad 4.2.8$$

In Eq. 4.2.8, $\boldsymbol{u}_{(t)}^l$ is the electrolyte velocity vector, p the system pressure, $\varphi_{(t)}^l$ the liquid volume fraction, ρ_l the electrolyte density, $\boldsymbol{F}$ the additional volume forces. The electrolyte dynamic viscosity is $\mu_l = 7.5 \times 10^{-3}$ Pa $\cdot$ s and $\mu_{(t)}^T$ represents the turbulent viscosity computed through the $k - \varepsilon$ turbulence model [19], [56]. The liquid volume fraction $(\varphi_{(t)}^l)$ was computed from the gas volume fraction $(\varphi_{(t)}^l = 1 - \varphi_{(t)}^{gas})$. The continuity equation assumes that the electrolyte is saturated with chlorine. Consequently, the mass transfer of chlorine gas into the electrolyte solution by dissolution was neglected, as shown in Eq. 4.2.9.

$$\frac{\partial \left(\varphi_{(t)}^{gas} \rho_g \right)}{\partial t} + \nabla \cdot \left(\varphi_{(t)}^{gas} \rho_g \boldsymbol{u}_{(t)}^{gas} \right) = 0 \qquad 4.2.9$$

$$\left(\varphi_{(t)}^{gas} \rho_g \right) \boldsymbol{u}_{(t)}^{gas} = \varphi_{(t)}^{gas} \left[\frac{1}{2} \left(C_o^{Cl^-} - C_{(t)}^{Cl^-} \right) M_{Cl_2} \right] \boldsymbol{u}_{(t)}^{gas} \qquad 4.2.10$$

The mixture model was used to represent the liquid lithium drops fluid dynamics in the electrolyte solution. The velocity term was computed according to the effect provided by each phase, as shown in Eq. 3.2.13. The mixture momentum Eq. 4.2.11, coupled with the bubble momentum (Eq. 4.2.8), was used to represent the fluid dynamics of the liquid lithium drops as shown in the next equations:

$$\rho \cdot \frac{\partial \boldsymbol{j}}{\partial t} + \rho (\boldsymbol{j} \cdot \nabla) \boldsymbol{j} = -\nabla \cdot \boldsymbol{p} + \left[\left(\mu + \mu_{(t)}^T \right) \left[\nabla \boldsymbol{j} + (\nabla \boldsymbol{j})^T \right] + \rho \cdot \boldsymbol{g} + \boldsymbol{F} \qquad 4.2.11$$

$$\rho = \varphi_{(t)}^l \rho_l + \varphi_{(t)}^{drop} \rho_d \quad \text{and} \quad \varphi_{(t)}^l = 1 - \varphi_{(t)}^{drop} \qquad 4.2.12$$

$$\boldsymbol{j} = \boldsymbol{j}_c + \boldsymbol{j}_d \quad \text{with} \quad \boldsymbol{j}_c = \varphi_{(t)}^l \boldsymbol{u}_{(t)}^l \quad \text{and} \quad \boldsymbol{j}_d = \varphi_{(t)}^{drop} \boldsymbol{u}_{(t)}^{drop} \qquad 4.2.13$$

Where $\boldsymbol{j}$ is the velocity field of the mixture phase (see Eq. 4.2.13), $\boldsymbol{j}_c, \boldsymbol{j}_d$ are the continuous (electrolyte) and the dispersed (lithium drops) phase velocity flux respectively. $\boldsymbol{u}_{(t)}^l, \boldsymbol{u}_{(t)}^{drop}$ are the electrolyte and the lithium drop mass-averaged velocity field, while $\varphi_{(t)}^l, \varphi_{(t)}^{drop}$ denote the volume fractions of the continuous and dispersed phases [15].

The continuity equation (Eq. 4.2.14) also assumes that the electrolyte was saturated in lithium and so, the mass transfer from the lithium drops to the electrolyte solution was neglected.

$$\frac{\partial}{\partial t}\left(\varphi_{(t)}^{drop}\rho_d\right) + \nabla \cdot \left(\varphi_{(t)}^{drop}\rho_d \boldsymbol{u}_{(t)}^{drop}\right) = \nabla \cdot \left(\rho_d D_{md}\nabla\varphi_{(t)}^{drop}\right) \text{ with } D_{md} = \frac{\mu_{(t)}^T}{\rho\sigma_T} \qquad 4.2.14$$

$$\varphi_{(t)}^{drop}\rho_d \boldsymbol{u}_{(t)}^{drop} = \varphi_{(t)}^{drop}\left[\left(C_o^{Li^+} - C_{(t)}^{Li^+}\right)M_{Li^+}\right]\boldsymbol{u}_{(t)}^{drop} \qquad 4.2.15$$

where D_{md} is the turbulent dispersion coefficient, accounting for extra diffusion due to turbulent eddies, σ_T is the turbulent Schmidt number.

4.2.4 Cathodic phenomena

The linearized Butler-Volmer (LBV) equation (Eq. 4.2.16) was applied at the cathode surface.

$$i_{(t)}^{Ca} = i_{o_{Ca}}\frac{\alpha_{Ca}.F}{R.T}\,\eta_{(t)}^{Ca} \qquad 4.2.16$$

where the cathodic exchange density current is $i_{o_{Ca}} = 1000\ A/m^2$, and $\eta_{(t)}^{Ca}$ stands for the cathodic overpotential.

For the cathode rotating cases, the surface velocity ($V_{\theta\,Ca}$) was simulated using Eq. 4.2.17.

$$V_{\theta\,Ca} = (2\pi)\,r.\,(-\,\text{n}) \qquad 4.2.17$$

4.2.5 External electrolytic potential (E_{Cell}) and energy consumption (E_{Cons})

The cell potential was calculated through the Eq. 4.2.18 considering the additional bubble overpotential in the anodic boundary layer ($\eta_{(t)}^{ABL}$). The anodic equilibrium potential was further fixed at 3.6 V and the cathode was considered as an ideally depolarized reference electrode, E_{eq}^{Ca} = 0 V. The recombined lithium mass, representing all lithium drops entrained into the anode domain (D$_2$, see Table 4.2) is described in Eq. 4.2.19.

$$E_{cell} = E_{eq}^{An} - E_{eq}^{Ca} + \eta_{(t)}^{An} + \eta_{(t)}^{Ca} + \eta_{(t)}^{ABL} + \eta_{(t)}^{Ohmic} \qquad 4.2.18$$

$$\dot{m}_{Li}^{Recombined} = \varphi_{Li}^{D_2}\,m_{Total}^{D_2}\,\left(\rho_{Li_{(Liq)}}/\rho_l\right) \qquad 4.2.19$$

Finally, the specific energy consumption (in kWh/kg of Li) depends on the predicted mass of recombined lithium in the anode domain (D$_2$), as shown in Eq. 4.2.20.

$$E_{Cons} = E_{cell}\,I_{cell}/(\dot{m}_{Li}^{Total} - \dot{m}_{Li}^{Recombined}) \qquad 4.2.20$$

4.3 Results and discussion

This section is divided in two parts:

1. The validation of the mathematical model including the definition of calculation domain, mesh density and appropriate boundary conditions, are briefly described in Table 4.2. The validation of the fluid dynamics was done using a lithium electrolytic

cell with a non-porous (ungrooved) cylindrical diaphragm with a radius of 34 mm and a thickness of 1 mm.

2. The contributions of this work, where results are shown on the effect of the anodic film resistance, on the impact of the grooved diaphragm design and on the influence of a rotating electrode on the performance of the electrochemical cell.

4.3.1 Geometric mesh validation

Cell geometry arrangement with boundary conditions for electrochemical (Tertiary Current Distribution model, TCD), mass and momentum transfer, is shown in Fig. 4.4 with its parameters in Table 4.2.
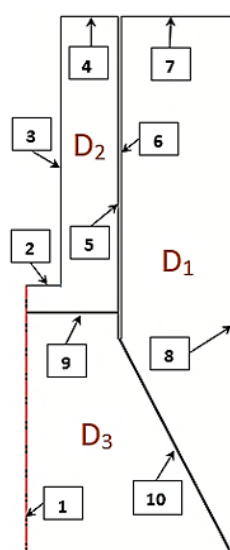

Fig. 4.4 Boundary conditions.

Table 4.2. Domain and boundary conditions parameters.

	Boundary conditions	Phenomena		
		TCD	Mass Transfer	Fluid Dynamics
1	Symmetry Axis	Insulated	$dNi/dr = 0$	$du_r/dr = 0$ $du_z/dr = 0$
2	Anode	$I = 7800$	$-N_{Cl_2}$	$\dot{m}_{Cl2(in)}$
3	Surface	A/m^2	$= i_{(t)}^{An}/(vF)$	
4	Anode Outlet	Insulated	dN_{Cl_2}/dt $= -\dot{m}_{Cl2(Out)}$	$\dot{m}_{Cl2(Out)}$
5	Cylindrical		Insulated (non-porous)	
6	Diaphragm			
7	Cathode Outlet	Insulated	dN_{Li}/dt $= -\dot{m}_{Li(out)}$	$\dot{m}_{Li(out)}$
8	Cathode Surface	$\Phi = 0\,V$	$-N_{Li}$ $= i_{(t)}^{Ca}/(vF)$	$\dot{m}_{Li(in)}$

Boundaries 9 and 10, which represent interdomain boundaries were used to divide the cell into three domains which facilitates data treatment and interpretation of mass transport effects on the lithium recombination and energy consumption. These three domains (D_1, D_2 and D_3) were also used to validate the mesh. The model was evaluated with six different types of mesh, which are described in Table 4.3.

Table 4.3. Meshes with different element sizes as predefined by Comsol®.

Element sizes	Coarser	Coarse	Normal	Fine	Finer	Extra fine
Maximum (m)	0.00661	0.00509	0.00342	0.00266	0.00213	9.88e-4
Minimum (m)	3.04e-4	2.28e-4	1.52e-4	7.6e-5	3.04e-5	1.14e-5
Density (Elem./m³)	1.20e6	1.488e6	1.956e6	2.288e6	2.834e6	5.032e6

The effect of the different mesh sizes on the calculation of bubble velocity is shown on the of Fig. 4.5-A. It can be concluded that mesh independency is obtained with a mesh density of $5.032e6\ Elem/m^3$, a value close to the Oliaii et al. (2017) mesh density ($6.98e6\ Elem/m^3$). Also shown in Fig. 4.5-A, close to the top of anode length, when the mesh density increases, the value of the gas velocity approaches a constant value of $0.37\ m/s$, reached with finer to extra-fine meshes, confirming mesh independency of the results. Also, in the length interval between 0.18-0.19 m, the gas velocity curve presents less fluctuations when the mesh elements number increases.

To explain the behaviour of the avg. gas velocity (Fig. 4.5-B), the liquid velocity produced by the bubbles in the anode domain (D$_2$) is shown on the right of Fig. 4.5, where a swirl (orange streamline) is also illustrated. The liquid velocity close to the anode surface where $r = 12.7\ mm$ starts with a minimum value of $5x10^{-3}\ m/s$ at $z = 0.1\ m$, caused by the buoyancy force exerted by the bubbles that begin to detach from the anode. Subsequently, the liquid velocity increases until it reaches its maximum ($190x10^{-3}\ m/s$) at $z = 0.185\ m$. Beyond this point, the liquid velocity starts to decrease due to the presence of the eddy at the top of the anode surface, which entrains the bubbles outside the system (boundary condition # 4).

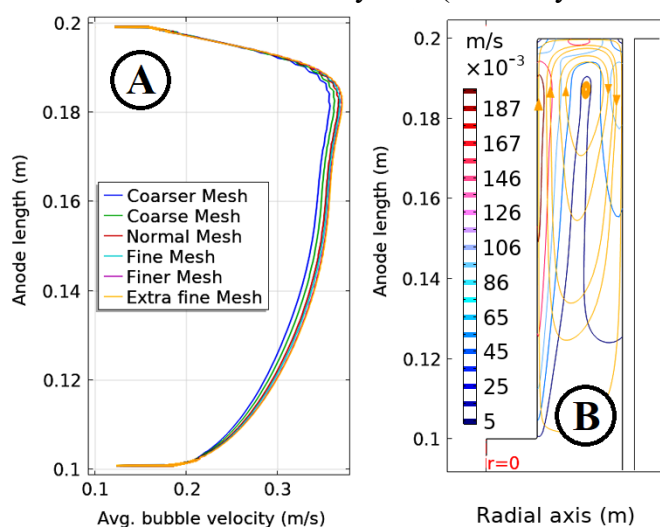Fig. 4.5 Mesh validation for different mesh density (A) electrolyte velocity behaviour in anode domain (B).

4.3.2 Contributions of this research

As stated previously, the contributions of this research project are presented in three sections:

1. The transient behavior of boundary layer and film resistance are analyzed.
2. The design of an original grooved diaphragm between anode and cathode is studied.

3. The influence of the use of rotating electrodes is evaluated as a particular operating condition.

4.3.2.1 Boundary layer of electrochemical and fluid dynamics fields

To estimate the electrochemical film resistance, it was assumed that the fluid dynamics boundary layer is the same as for electrochemical field. The variation along the anode height of different components of the anodic potential at t = 600 s is shown in Fig. 4.6, using Eq. 4.2.3 to represent the film resistance overpotential.

The electrolyte potential (EP) is the voltage resulting from the migration of ions within the electrolyte solution. The kinetic potential (KP) represents the overpotential due to the electrochemical reaction responsible for the production of chlorine gas. Finally, the film overpotential (FO) describes the resistance to the charge and mass transfer caused by the bubble in the boundary layer. The results obtained in this project were compared with those of Oliaii et al. (2017). The effect of diaphragm resistance can be seen from the potential and overpotential evolution along the anode height, at $z \approx 0.1$ m. The diaphragm acts as a barrier between the anode and cathode surfaces, allowing the reaction to occur with greater intensity in the bottom part of the anode, where one can find the shortest path between the anode and cathode and where FO and KP get to their peak value. These two curves show a similar behavior, which is linked to the quantity of bubble produced in the boundary layer by the electrochemical reaction. On the other hand, the EP results presents the opposite behavior, as a consequence of the resistance to the current transfer of the electrolyte solution, which is minimal close to the anode tip, where the shortest anode to cathode distance is found. The results of this project are slightly different from those of Oliaii et al. results, due to different approaches taken for the effect of bubble coverage on electrolyte conductivity.
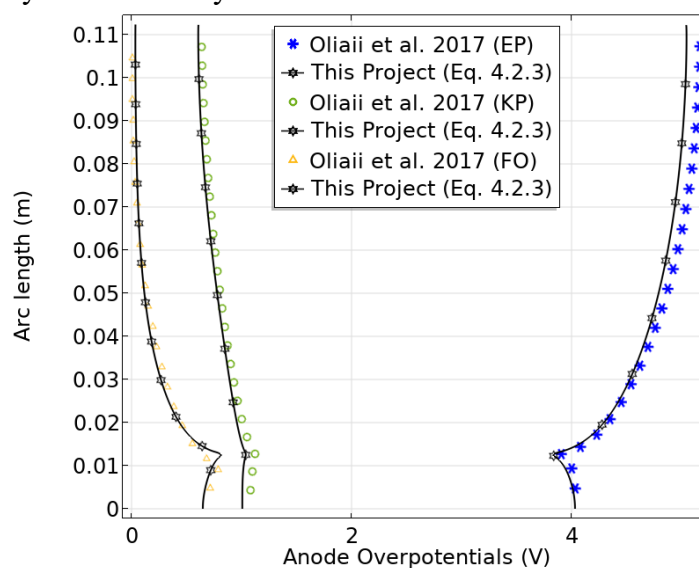

Fig. 4.6 Potential and overpotentials vs the anode height, at 600 s.

The close relationship between the electrochemical and fluid dynamics fields can be linked to the behavior of the boundary layer. The evolution of the boundary layer (A) and the variation of the film overpotential (B) along the anode surface can be seen in Fig. 4.7, for every dt = 50 s.
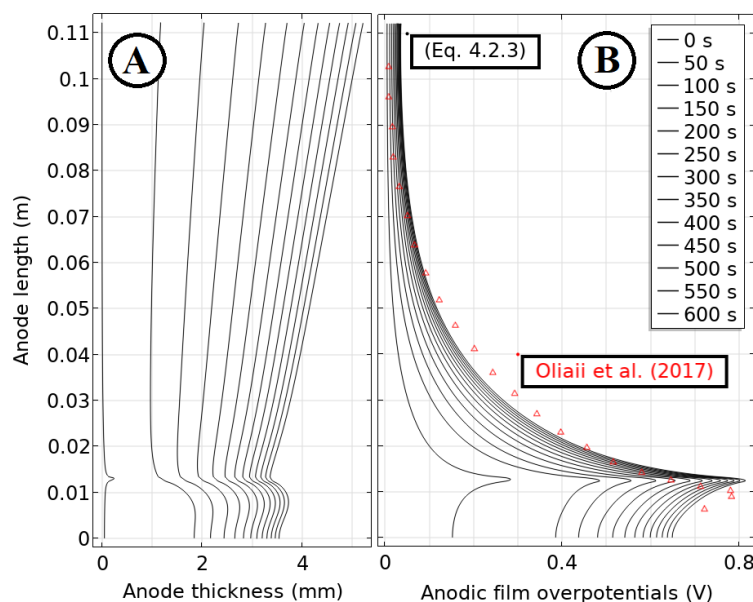

Fig. 4.7 Boundary thickness (A) and anodic film overpotential (B) vs the height of the anode.

In both figures, the curves approach to steady state conditions after 600 s. In the figure on the left, the results obtained between the interval of z = 0 and 0.0127 m correspond to the boundary layer formed at the bottom of the anode (horizontal section), while those obtained from z = 0.0127 m to 0.11 m corresponds to the anode sidewall (vertical section). The transient evolution of anodic film overpotential captures the accumulation of higher amounts of gas with time in the upper section of the cell, thanks to the new equation (Eq. 4.2.3) representing the variation of the boundary layer as a function of gas production at the anode.

4.3.2.2 Vertical diaphragm with a non-porous and grooved design.

In this section, the electrochemical and fluid dynamics fields obtained with ungrooved (non-porous) and grooved vertical diaphragms (RB = 34 mm, β=90°) are compared. Their effects on recombined lithium mass and energy consumption are also analyzed. The premises were that grooved diaphragms would help to keep the fluid dynamics of each domain separated and to reduce to minimum the charge and mass transfer barriers, thus increasing the efficiency of the cell with minimum amount of recombined lithium mass and specific energy. The results of this research work are also compared to those of Melendez et al. (2022), who studied the effect of diaphragm inclination on the recombined lithium mass and energy consumed. Fig. 4.8 shows the chlorine bubbles, and the liquid lithium drops fluid dynamics, coupled with the electrochemical field of an ungrooved (A) and grooved (B) diaphragms.
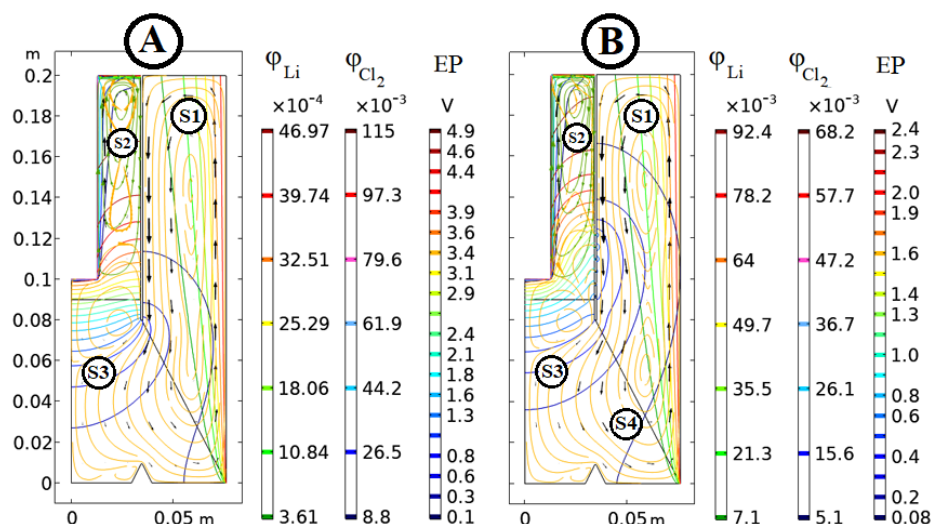
Fig. 4.8 Electrolytic cell with a ungrooved (A) and grooved diaphragm (B) at 600 s.

In general, the grooves (Fig. 4.8-B) allow the current, mass and momentum transfer without change notably the fluid dynamics to each domain. The isocontours close to the surfaces of the anode and cathode represent the volume fractions of chlorine gas (φ_{Cl_2}) and liquid lithium (φ_{Li}), respectively. One can also see that the electrolyte potential (EP) field is quite different for the two cases. The EP shows a maximum value of 4.9 V in the electrolytic cell with an ungrooved diaphragm (Fig. 4.8-A), while this value reduces to 2.4 V for the grooved diaphragm (Fig. 4.8-B), grooves improving the ion transfer between the electrodes and thus reducing the ohmic losses. The fluid dynamics shown in Fig. 4.8-A is characterized by three main eddies, one formed along the cathode surface (domain D_1) due to the momentum of liquid lithium rising up (S1), another formed at the top of the anode domain (D_2) due to the momentum of the chlorine bubbles (S2), and finally a third one formed at the bottom of the anode between the D_2 and D_3 domains (S3). Those eddies can be seen through the green and orange streamlines representing the velocity of bubbles and lithium drops, respectively. On the other side, the grooved diaphragm (Fig. 4.8-B) has a momentum transfer from D_2 to D_1 where grooves are located. The formation of two eddies along with cathode surface (S1 and S4) can also be observed. These additional momentum transfer mechanisms explain the differences between chlorine (φ_{Cl_2}) and lithium (φ_{Li}) volume fractions in each electrolytic cell and the increased entrainment of the dispersed phase caused by momentum transport from the eddies.

Fig. 4.9 shows the average velocity inside the D_1 and D_2 domains as a function of time. The average velocity curves for both domains increase with time, due to the increase of chlorine bubbles and liquid lithium production during the electrochemical reaction. The momentum in the anode domain is more important than in the cathode domain, the buoyancy force of the chlorine bubbles being higher than the buoyancy force of the liquid lithium. Furthermore, the simulations show a decrease in the anode average velocity when a grooved diaphragm is used. The opposite effect is seen in the cathode domain, where the average velocity increases for the

with the use of grooved diaphragm design. This can be easily explained by the additional momentum transfer from anodic to cathodic domain with grooved diaphragm design.
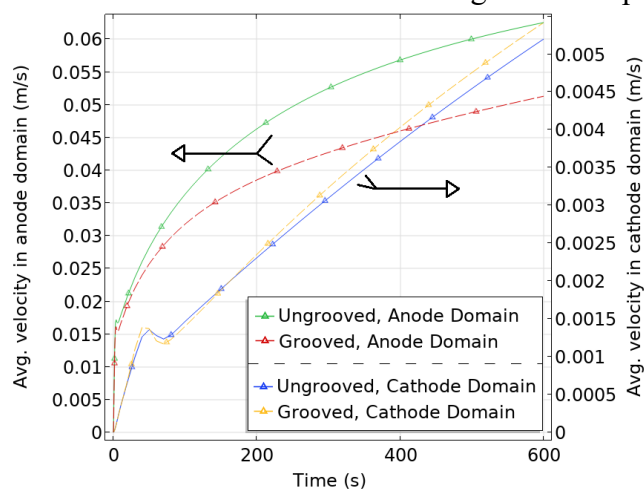

Fig. 4.9 Average velocity in the cathode and anode domains.

Fig. 4.10 shows the mass of lithium and chlorine close to each side of the diaphragm for both cell designs, after 600 s of operation. The surface of the diaphragm that is in contact with the D_2 domain is called the anode domain, while the surface that is in contact with the D_1 domain is called the cathode domain. One can observe that the lithium mass for both designs increases with the height of the diaphragm.

In general, the transfer of chlorine to the cathode domain through the grooves is not important because chlorine bubbles are quickly leaving the reactor due to the action of the high buoyant force. For both designs, the chlorine concentration is very low between $0 < z < 0.08$ m, where the grooves are located. When $z > 0.05$ m, the lithium concentration on the surface of the grooved diaphragm is higher than that of ungrooved design, due to the higher kinetic energy (momentum) of the S1 eddy found in grooved design. For the same reason, the amount of chlorine is lower for the grooved design. Also, the influx of Li into the anode domain, a quantity used to estimate the recombined Li mass, can be seen on the Fig. 4.10 for the groove # 1.

As shown in Fig. 4.11, the current density at the diaphragm level transported by ions in the electrolyte is clearly affected by the presence of grooves. The ungrooved diaphragm has its highest current density of 97×10^3 A/m^2 at the bottom ($z = 0$ m), a value that decreases with the diaphragm height. On the other hand, the current density over the surface of the grooved diaphragm does not reach such a peak and shows ripples at the level of each groove. The maximum current density increases with the position of the groove: a value near 20×10^3 A/m^2 is obtained for groove N° 6 (close to the bottom) and 60×10^3 A/m^2 for groove N° 1 (close to the top of the cell).
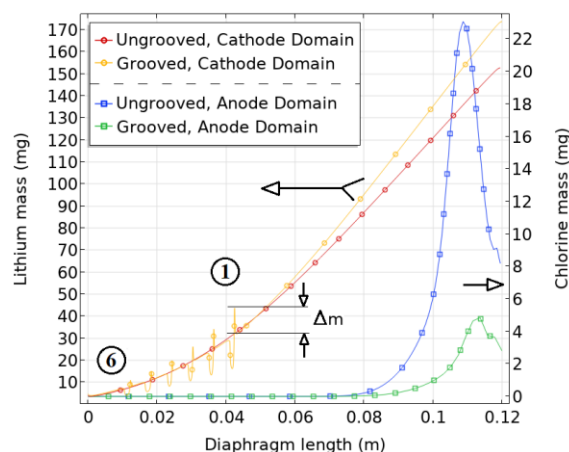
Fig. 4.10 Lithium and chlorine mass on diaphragm surfaces, at 600 s.

The current density gets higher in the first groove, which takes a more important part of the current load due to the blocking effect of the upper part of the ungrooved diaphragm. Finally, the current density for both designs levels off to zero when reaching the top of the diaphragm.
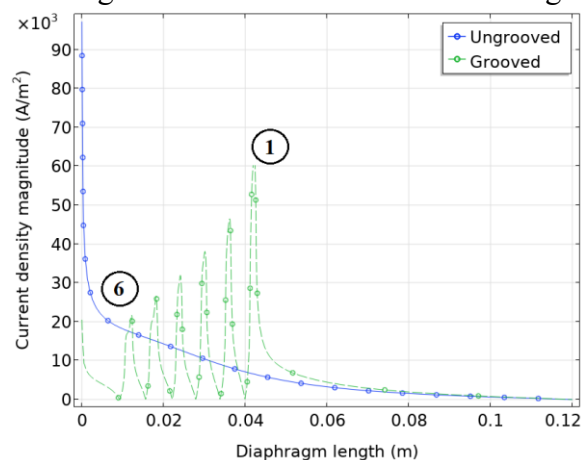
Fig. 4.11 Current density magnitude on diaphragm surfaces at the diaphragm level, after 600 s.

Fig. 4.12 shows the current density along the anode length for the two diaphragm designs studied. The current density profile is similar for both designs, the principal difference being a much more uniform anodic current distribution with grooved design. The blocking effect of the diaphragm on the current transfer can be clearly seen. As expected, the highest current transfer for both designs occurs at the edge of the anode ($z = 0.0127$ m), where the current density peaks at an approximate value of 35000 A/m^2 for the grooved design and 50000 A/m^2 for ungrooved design. Then, the current density starts to decrease until it reaches its minimal value at the top of the anode surface ($z = 0.11$ m). The diaphragm at this height does not barely allow any current to flow (blocking effect). When compared, the grooved diaphragm decreases peak current density by 64 %, ending up with a better distribution on the anodic surface.
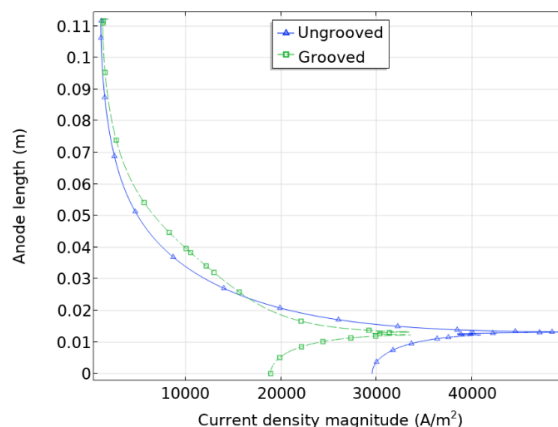
Fig. 4.12 Current density magnitude on the anode surface with a
ungrooved and grooved diaphragms.

In Fig. 4.13, the potential breakdown of grooved and ungrooved diaphragms are compared along the anode length. In this figure, a logarithm scale was taken for the anode length to highlight the differences between the behavior of both designs. The grooves permitted a 50 % reduction in the film overpotential (FO), a 10 % reduction in the kinetic potential (KP) at the bottom surface of the anode, and a 54 % decrease in the electrolyte potential (EP). According to our modeling predictions, the use of grooved diaphragm would lead to a 45 % reduction in the total cell potential.
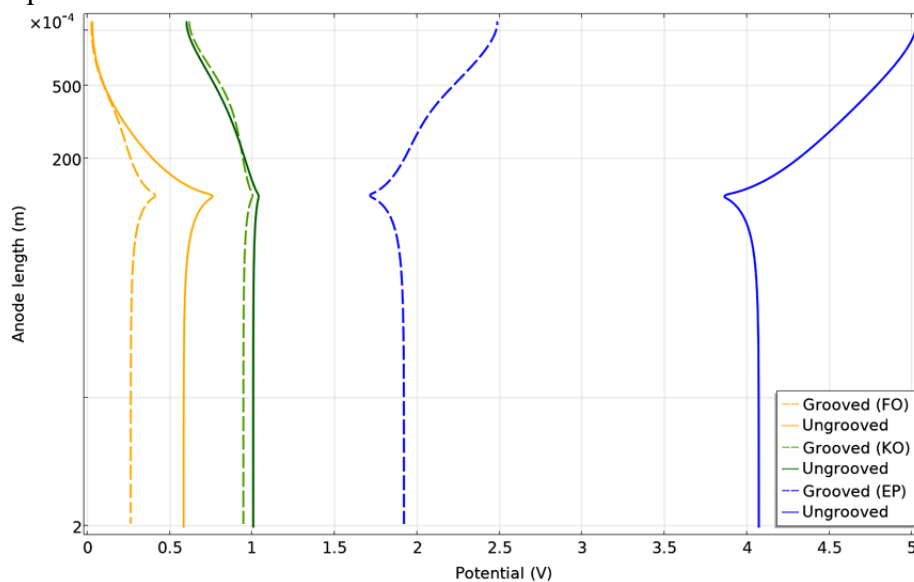
Fig. 4.13 Potential and overpotentials along with the anode height with a ungrooved and grooved diaphragms.

The total mass of lithium produced after 600 s is illustrated in Fig. 4.14 using the mass balance and Faraday equation. It shows the time evolution of the recombined lithium mass for the grooved and ungrooved diaphragms, with or without (Melendez et al. 2022) using the new boundary layer resistance equation. The total lithium mass produced is 2.81 g, a value obtained

either from a global mass balance or by using Faraday's law. The ungrooved diaphragm leads to a recombined lithium mass of 4.5 mg, a value which is almost multiplied by 4 (16.7 mg) with the grooved design. However, this quantity is still very low since it represents only 0.6 % of total lithium produced during this 600 s production period.
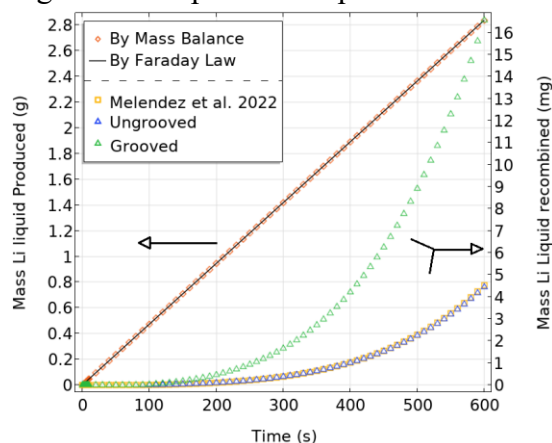
Fig. 4.14 Recombined lithium mass with a non-porous and grooved diaphragm.

The Fig. 4.15 shows the specific energy consumed in the simulated lithium electrolytic cell for both designs. The difference between the energy consumed by the ungrooved diaphragm and the results of Melendez et al. (2022) is coming from the film resistance used in this research work, which leads to a small but more realistic increase of the total cell potential. Moreover, the grooved diaphragm design shows a remarkable potential of reduction of 26.7 % in the energy consumption.
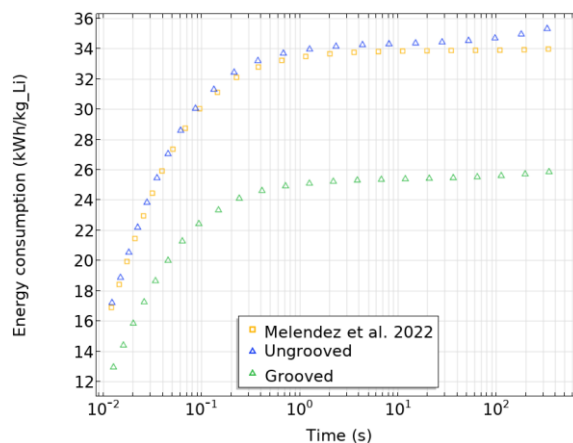
Fig. 4.15 Specific energy consumed using a non-porous and grooved diaphragm.

4.3.2.3   The inclination effects in the grooved diaphragm

In this section, the effect of inclination of the grooved diaphragm on the fluid dynamics and electrochemical behaviour is analyzed using three inclination angles (RB = 25 (85°), 29 (87°),

and 34 mm (90°)). Fig. 4.16 shows the variation of the electrolyte potential and streamlines of chlorine gas, lithium liquid and current density in the electrolytic cell.

The electrolyte potential increases as the angle of inclination of the diaphragm decreases, due to the mass transfer resistance increase with more important inclination between the diaphragm and the anode. Current streamlines (red lines) modifications are also apparent in the electrolyte solution, current distribution getting more uniform for the 90° inclination. Looking at the liquid lithium drops fluid dynamics (orange streamline), one can conclude that the S4 eddy present in the 90° inclination is losing kinetic energy when the angle of inclination of the diaphragm is decreased, leading to its merging with the S1 eddy at the 85° inclination.
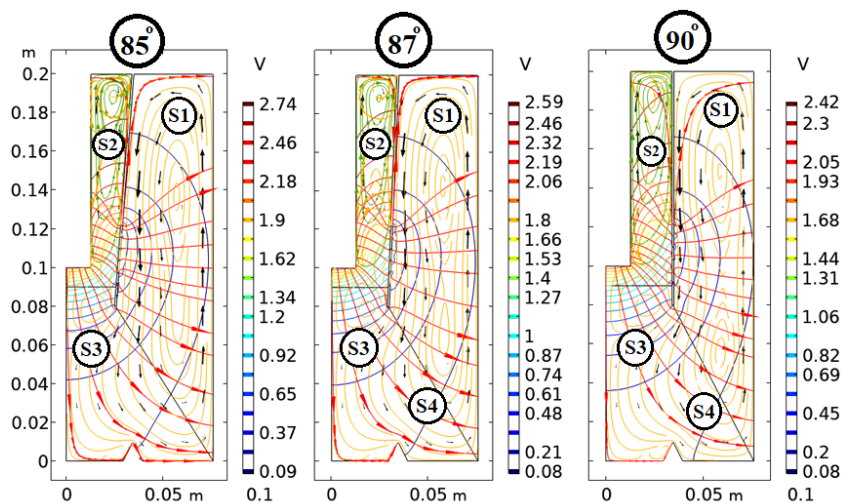
Fig. 4.16 Electrolyte potential and contours of current density (red), bubble (green), and Li drop (orange) streamlines at different inclination angles.

Also, the S3 eddy decreases in size when decreasing the angle of inclination, a sign that it is losing its energy. This also means that the momentum transfer from the anode to the cathode domain gets reduced when the inclination of the diaphragm decreases. On the other hand, S1 and S2 eddies accumulate largest amount of kinetic energy for the 85° inclination, which can in turn leads to a greater accumulation of chlorine and lithium liquid at the top of the anode and cathode domains, respectively. That accumulation inside each domain would represent a risk of recombination or increased energy consumption.

The Fig. 4.17 shows the average velocity inside the anode and cathode domain for the different inclination angles of the grooved diaphragm, after 600 s. When compared to the 90° configuration, the average velocity increases by 10.5 and 24 % in the anode domain, and by 4.26 and 9.26 % in the cathode domain for the inclinations of 87° and 85° respectively. Furthermore, the results of Fig. 4.17 is another illustration of the fluid dynamic behavior explained in Fig. 4.16, where the bottom eddies S3 and S4 lose their kinetic energy at the profit of eddies S1 and S2.
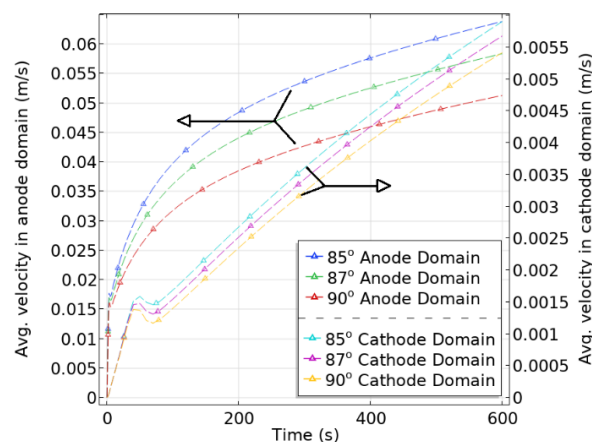
Fig. 4.17 Average velocity in the cathode and anode domains for 85°,
87° and 90° inclination angles of the diaphragm.

The transient evolution of the total cell potential (E_{Cell}) is shown in Fig. 4.18 for the three different values of inclination angles of the grooved diaphragm. While the results obtained previously by Melendez et al. (2022) are showing a steady state behavior, the results of this research work present a slight voltage variation with time, essentially during the first 50 s of simulation time. This difference can be explained by the new approach taken to represent the boundary layer resistance which captures the transient buildup of the bubble layer on anode surface. According to the simulation results, the grooved diaphragm is responsible for a 30 to 40 % reduction of the cell potential depending on the inclination, when compared to the results previously obtained by Melendez et al. for the same inclinations. When compared to the vertical grooved diaphragm (90°), the cell potential increases by 3.7 and 1.5 % for the 85° and 87° inclination angles respectively, the difference being caused by the increased resistance attributed to the ions transfer in the electrolyte solution.
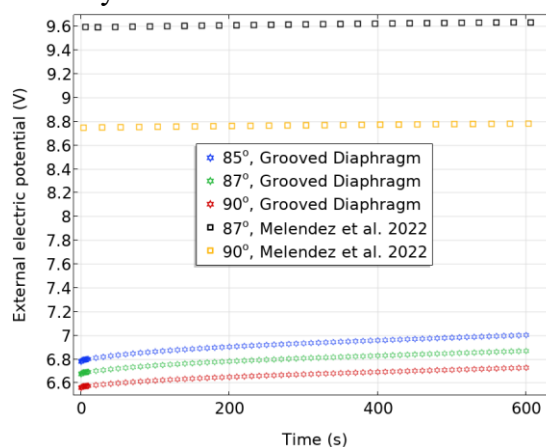
Fig. 4.18 External electric potential (E_{cell}) for 85°, 87° and 90°
inclination angles of the diaphragm.

The variation of recombined mass of lithium with time is shown in Fig. 4.19 for the different inclination angles of the grooved diaphragm. When compared to Melendez et al. (2022), lithium

recombination is increased by 73 and 86.4 % for grooved diaphragms with 87° and 90° inclinations respectively. On a more positive side, the recombined mass is decreased by 51.5 to 71.3 % when the 90° grooved design is replaced by 87° or 85° grooved designs. Still, the mass lost by recombination is very small (< 0.6 %) with respect to the total mass produced.
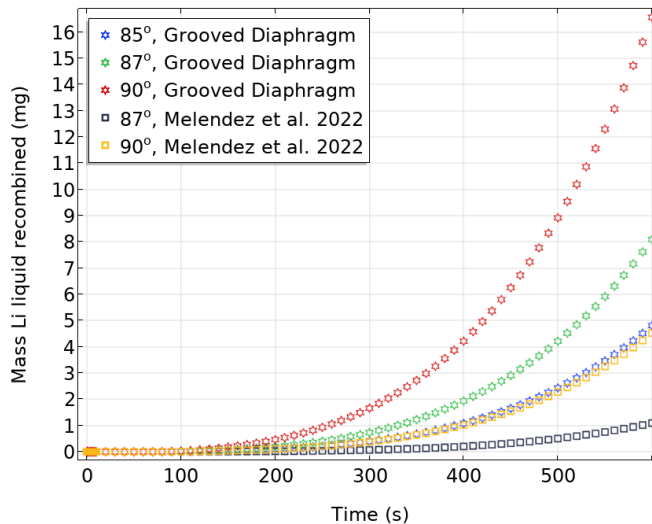
Fig. 4.19 Mass of lithium recombined in the anode domain for 85°, 87° and 90° inclination angles of the diaphragm.

Transient profiles of the energy consumed by the grooved diaphragm cell is illustrated in Fig. 4.20 for the different inclination angles. When compared to Melendez et al. (2022), the energy consumption by the grooved diaphragm is reduced by 27.3 % for the 87° angled design. When compared to the vertical grooved diaphragm (90°), the energy consumed is increased by 4.3 and 2.3 % when 85° and 87° angles are respectively used.
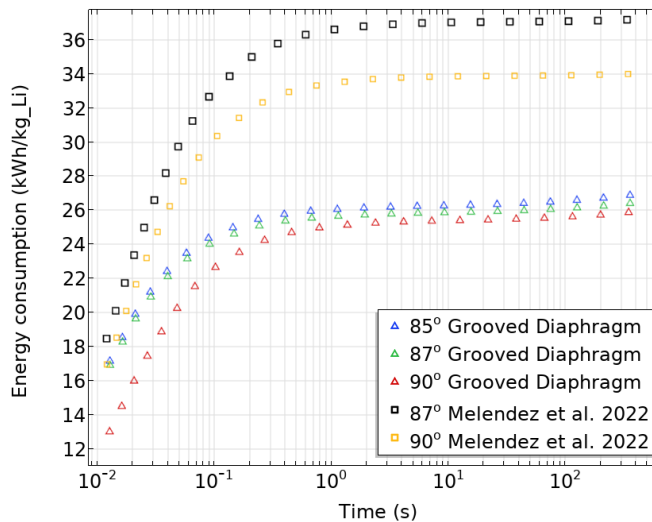
Fig. 4.20 Specific energy consumed in the process for 85°, 87° and 90° inclination angles.

According to Fig. 4.19 and Fig. 4.20, one can observe that there is a direct relationship between the inclination angle and the amount of recombined lithium. The lower angle of inclination allows a reduction of the recombined lithium in spite of higher energy consumption. However, an increase of the height of every groove could lead to a decrease in energy consumption and counteract the negative impact of inclination angle.

4.3.2.4   The results of the electrolyte cell with rotating electrodes.

The objective of simulation with rotating electrodes is to analyse how the lithium production could be affected in a process where a continuous inlet with an angular flow of the electrolyte solution is injected. The effect of using rotating electrodes on electrochemical fields inside the lithium electrolytic cell were studied using five values of electrode angular velocity ($n = 0$, 1/4, 1/2, 1 and 3/2 rad/s). The cathode surface is rotated in the opposite direction of the anode surface ($V_{\theta\,Cat} = -V_{\theta\,An}$) and one electrode is rotated at a time. While in configuration A, only the anode rotates, in configuration B, only cathode surface is in movement. The volume fractions for the chlorine gas and the lithium liquid in proximity of the anode and cathode surfaces are shown in Fig. 4.21 for the 2 configurations. The Cl_2 gas (green) and lithium liquid (orange) streamlines are also added to the figure. In configuration A, the rotating fluid dynamics is more developed in the inter-domain region (D3) where the formation of a bigger eddy L3 can be seen. Also, two eddies (L1 and L2) are created in the cathode domain (D1), one at its top (L1) with the green streamline, and the second along the cathode height with the yellow streamline (L2). On the other hand, for configuration B, only two eddies, L1 and L3, are formed.
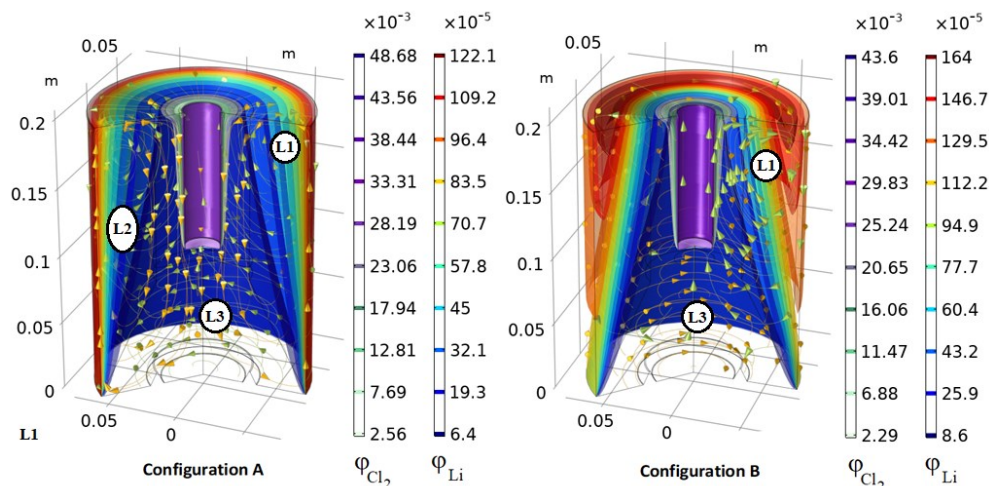
Fig. 4.21 Rotating anode (left) and rotating cathode (right) for $n = 1$ rad/s at 600 s.

The velocity behaviour in the anode and cathode domain for configuration A and B is shown in Fig. 4.22. For both configurations, the yellow line represents the behaviour of the flow close to the electrode without rotation. In general, the cathode rotating surface produces more kinetic energy in the electrolyte because its higher surface area and radius. The resistance to rotational movement is important due to the very viscous (7.5 Pa·s) electrolyte.
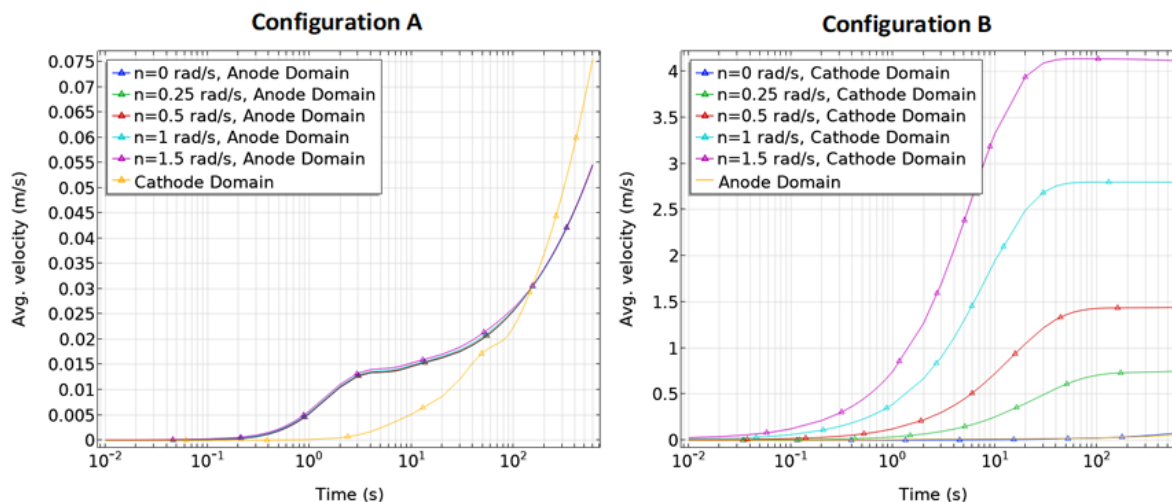
Fig. 4.22 Average velocity with rotating anode (configuration A) and rotating cathode (configuration B).

Fig. 4.23-A shows that the cell electrical potential slightly decreases when the anodic angular velocity is increased, due to easier bubbles detachment with the action of the circular movement. Fig. 4.23-B presents the variation of the boundary layer overpotential with height after 600 s. Again, the circular electrolyte movement leads to a reduction on bubble coverage on the anode which is reducing the boundary layer thickness and the film resistance.
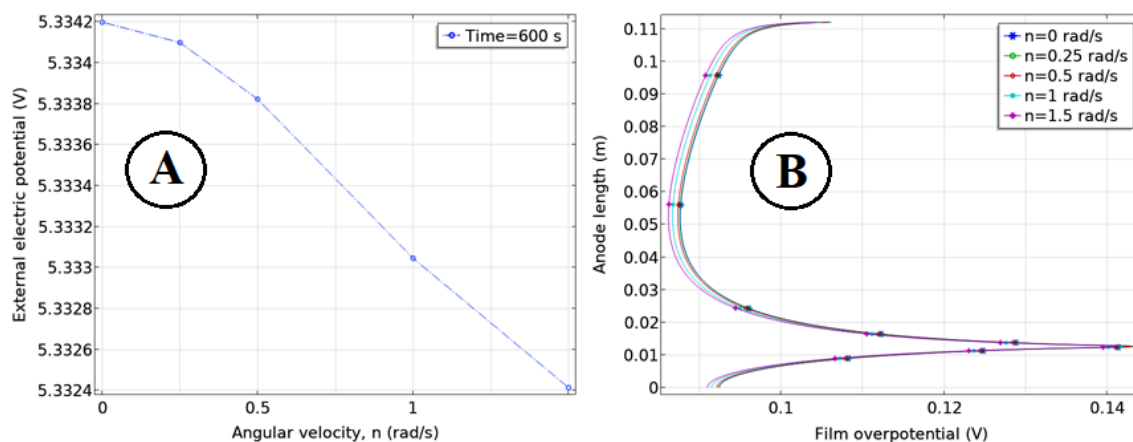
Fig. 4.23 Cell potential (A) and film overpotential (B) for different anodic angular velocity, at t = 600 s.

Fig. 4.24 presents the current density along the anode and cathode length for different rotation speeds, after 600 s. The behavior of anodic and cathodic current density is the same for all angular velocities. The simulated current densities on the anode and cathode surfaces does not change much for configuration A or B, since the properties of the electrolyte do not change when rotating electrodes are used. The small film overpotential does not produce a significant change in the anodic current density.
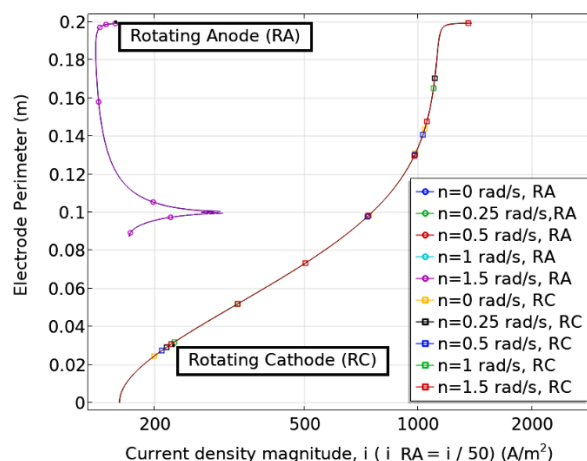
Fig. 4.24 Anode and cathode current density magnitude for different electrode rotation speeds.

The Fig. 4.25 shows the amount of recombined lithium for each configuration with time, the rotational movement of anode having no significant effect on the entrainment of the lithium droplets into the anode domain. When we compared to the results obtained by Melendez et al. (2022) on vertical non-porous diaphragm, one can see different behavior for rotating anode (configuration A), although at 600 s the mass of recombined lithium is very close. In configuration B (Fig. 4.25, right), the difference in the cathode tangential velocities is more pronounced which leads to important changes in the electrolyte fluid dynamics. The mass of recombined lithium decreases by 87.4 % when the angular velocity goes from 0 to 0.25 rad/s. Over that angular velocity, the mass of recombined lithium increases considerably, especially in the 1 to 1.5 rad/s range, caused by the kinetic energy of the L1 eddy that increases with angular velocity.
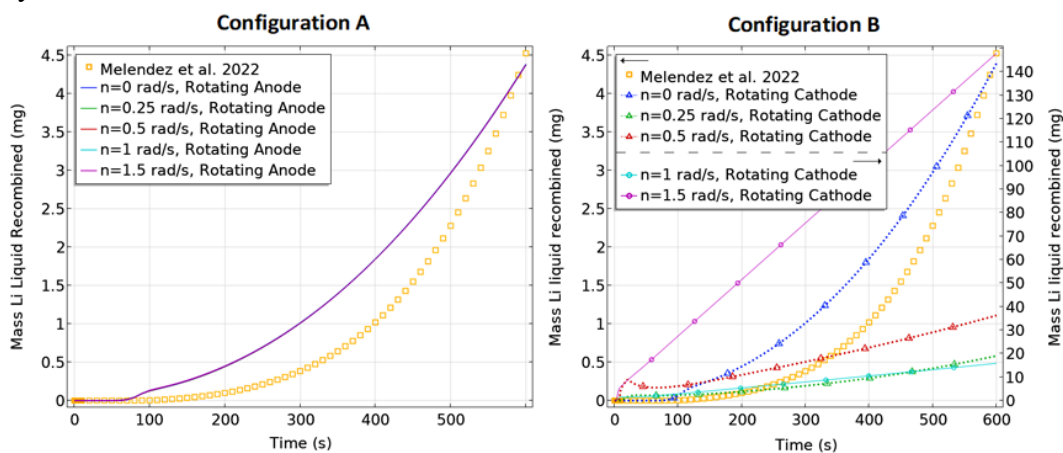
Fig. 4.25 Recombined lithium mass for different electrode rotation speeds.

Fig. 4.26 shows the energy consumption of the process as a function of angular velocity, after 600 s of operation. The energy consumed in configuration A decreases with increasing angular velocity, due to an improved bubbles detachment from the anode surface. Configuration

A decreases the energy consumed by 40 % when compared to the vertical ungrooved diaphragm and by 18.7 % when compared to the grooved design. The energy consumption in configuration B reaches its minimum at the angular velocity of 0.25 rad/s, with a slight reduction (-0.16%) when compared to configuration A.
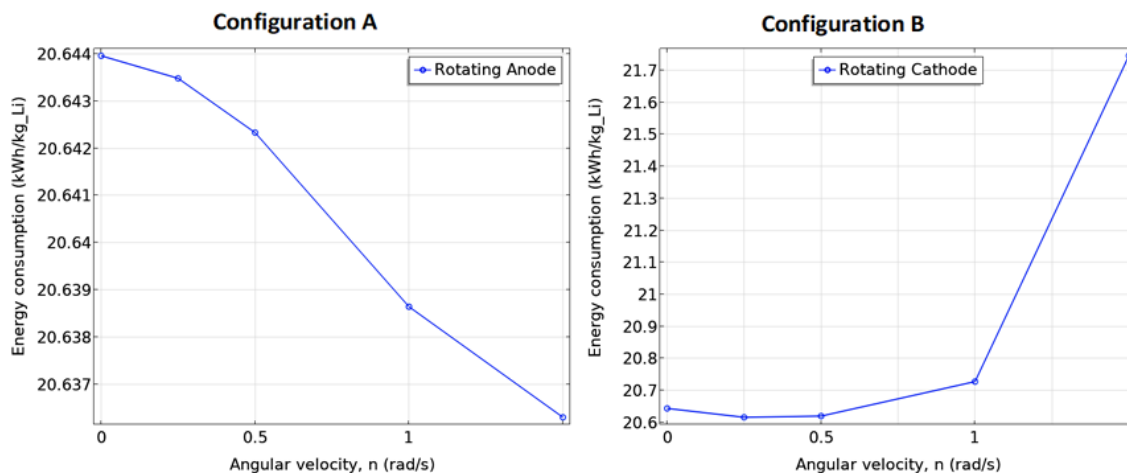
Fig. 4.26 Specific energy consumed for different electrode rotation speeds.

The impact of cathode rotation on the energy consumption (configuration B) is essentially attributed to the recombined metallic lithium, as the cell potential is almost independent to the angular velocity of cathode. This recombination is essentially caused by the rotational fluid dynamics of the cathode which produces two eddies in the electrolyte (L1 and L3). The lithium metal droplets accumulate at the top of the cathode due to the L1 eddy. As this accumulated mass increases with respect to the angular velocity of the cathode, it occupies a bigger volume at the top of the electrolytic cell (see Fig. 4.21). Consequently, the amount of metallic lithium in the anode domain increases, which leads to an increase in the specific energy consumption. When compared to straight ungrooved diaphragm and non-rotating electrode configuration, the best rotating cathode case, found at cathode angular velocity of 0.25 rad/s, presents the lowest energy consumption (-40%) and lithium recombination (-88.6 %). This performance can be explained by the removal of the diaphragm and by the elimination of recirculation zones close to the bottom of the anode.

4.4 Conclusion

An improved version of the model recently published by Melendez et al. (2022) [40] was developed to further refine the impact of lithium production cell design -straight ungrooved diaphragm vs straight grooved diaphragm vs inclined grooved diaphragm- and operating conditions (electrode rotation) on its performance, mainly specific energy consumption and lithium recombination with chlorine.

Comparing the non-porous ungrooved diaphragm with grooved diaphragm design, the latter design reduces the total cell potential by 45 %. However, the recombined lithium mass increased

by 3.7 times when an ungrooved diaphragm is replaced by a grooved design, a quantity that only represents 0.6 % of total lithium mass produced. By comparison with the Melendez et al. (2022) results, the proposed grooved design leads to a reduction of 26.7 % of the specific energy consumption. The impact of diaphragm inclination toward the anode, a design solution to lithium backreaction, was also assessed. When compared to the vertical grooved diaphragm, the inclined grooved designs show two opposite effects. On one hand, the cell potential increases by 3.7 % and 1.5 % respectively for the 85° and 87° angles. On the other hand, the recombined lithium is decreased by 71.3 % and 51.5 % respectively for the same angles. In the end, the energy consumption of the 85° grooved design, having roughly the same lithium recombination than the straight ungrooved diaphragm, leads to a reduction of 23.5 % of the specific energy.

The influence of electrode rotation on the cell fluid dynamics and on its electrochemical performance was also evaluated. Although the anode rotation movement modifies the fluid dynamics of the electrolyte solution, it does not significantly affect the amount of recombined lithium and the energy consumed, partly due to the high viscosity of the electrolyte and to the small anode area. In contrast, the cathode rotation movement can significantly affect the recombination of lithium metal and hence the energy consumed. When compared to straight ungrooved diaphragm and non-rotating electrode configuration, the best rotating cathode case, found at cathode angular velocity of 0.25 rad/s, presents the lowest energy consumption (-40%) and lithium recombination (-88.6 %). This performance can be explained by the removal of the diaphragm and the elimination of recirculation zones close to the bottom of the anode.

As future work, the authors propose to add an energy balance equation to the model. This new feature would help to represent the thermal gradients inside the cell and their impact on the mass transport and electrochemical reactions. Improvements of the model by incorporating a moving mesh at the interface between the electrolyte and the moving electrodes would also be beneficial to better capture the behaviour of the rotating electrodes and to predict the behaviour of the cell at higher rotating speeds. Finally, the developed model could also be advantageously used to assess the performance of new configurations inspired from industrial and patented designs. Further validation work might include the use patents' experimental data, Electrochemical Impedance Spectroscopy (EIS) measurements that can be used to validate kinetic parameters, mass transfer resistance and capacity (double-layer effects) at the interface of both electrode-solution interfaces, and flow visualization techniques. However, considering the harsh conditions prevailing inside such electrochemical system (high temperature, corrosiveness of the electrolyte), the implementation the EIS and flow visualization may be complicated, but it is worth trying in future works.

4.5 Acknowledgments

5 Conclusion

5.1 Conclusion en Français

Les électrolyseurs industriels conçus pour produire des métaux recherchent de nouvelles méthodes et techniques pour réduire leur consommation d'énergie et leur impact environnemental. Dans l'électrolyse du lithium, les bulles représentent un problème opérationnel lors de la production de métaux, en raison de leur effet de résistance au niveau du transfert de masse et de charge. Le lithium métallique peut également réagir avec le chlore gazeux et retourner à son état ionique. La simulation des processus électrolytiques est devenue un moyen privilégié pour rechercher et trouver des solutions aux différents problèmes qui se posent dans la production de métaux, surtout pour les applications où les mesures sont difficiles à obtenir. Les auteurs de ce travail de recherche présente un nouveau modèle mathématique qui comprend des caractéristiques importantes et originales telles que 1- la prédiction de la production de gouttes de Li liquide et la dynamique des fluides qui lui est associée, 2- la prédiction des bulles de Cl_2 produites sur la surface de l'anode. Le modèle a été utilisé pour étudier l'impact du design de la cellule sur la dynamique des fluides et sur la recombinaison du Li avec le Cl_2. Les simulations ont été menées pendant un temps d'électrolyse suffisant pour atteindre l'état d'équilibre en utilisant une approche turbulente (k-ε) pour résoudre l'écoulement diphasique couplé au processus d'électrolyse du lithium.

La validation de ce modèle pour chaque champ montre que le couplage entre le transfert de masse et celui de quantité de mouvement est important pour comprendre la recombinaison de la masse de lithium et l'énergie consommée dans le processus. Le modèle a été utilisé ici pour montrer l'impact de quatre configurations de cellules (diaphragme à 90° avec ou sans déflecteur inférieur, diaphragme à > 90°, diaphragme à < 90°) sur la dynamique des fluides de la cathode et sur la recombinaison du lithium avec Cl_2 dans le domaine anodique. Le déflecteur a réduit la quantité de lithium recombiné de 7 % sans coût énergétique supplémentaire. Le diaphragme avec une inclinaison < 90° a réduit la masse totale recombinée de 77 %, bien qu'il ait augmenté la consommation d'énergie de 10 % par rapport au cas de base d'un diaphragme vertical. Ce dernier cas illustre que certaines modifications de conception peuvent conduire à une réduction de la recombinaison du Li, mais à un coût énergétique élevé. Le modèle peut être utilisé pour guider les producteurs industriels afin d'optimiser leurs efforts de développement et d'identifier les paramètres qui permettent d'améliorer les coûts d'investissement et d'exploitation.

En comparant le diaphragme non rainuré non poreux avec le diaphragme rainuré, ce dernier réduit le potentiel total de la cellule de 45 %. Cependant, la masse de lithium recombiné est multipliée par 4 lorsqu'un diaphragme non rainuré est remplacé par un diaphragme rainuré, une quantité qui ne représente que 0,6 % de la masse totale de lithium produite. La consommation d'énergie spécifique de la conception rainurée entraîne une réduction de 26,7 % par rapport au cas de base d'un diaphragme vertical non poreux. L'impact de l'inclinaison du diaphragme vers l'anode, une solution de conception visant à minimiser la réaction inverse du

lithium, a également été évalué. Par rapport au diaphragme à rainures verticales, les conceptions à rainures inclinées montrent deux effets opposés. D'une part, le potentiel de la cellule augmente de 3,7 % et 1,5 % respectivement pour les angles de 85° et 87°. D'autre part, le lithium recombiné diminue de 71,3 % et 51,5 % respectivement pour les mêmes angles. Au final, la consommation d'énergie du design rainuré à 85°, ayant à peu près la même recombinaison du lithium que le diaphragme droit non rainuré, conduit à une réduction de 23,5 % de l'énergie spécifique.

L'influence de la rotation de l'électrode sur la dynamique des fluides de la cellule et sur ses performances électrochimiques a également été évaluée. Bien que le mouvement de rotation de l'anode modifie la dynamique des fluides de la solution électrolytique, il n'affecte pas de manière significative la quantité de lithium recombiné et l'énergie consommée, en partie à cause de la viscosité élevée de l'électrolyte et de la petite surface de l'anode. En revanche, le mouvement de rotation de la cathode peut affecter de manière significative la recombinaison du lithium métal et donc l'énergie consommée. Comparé à un diaphragme droit non rainuré et à une configuration d'électrode non rotative, le meilleur cas de cathode rotative, trouvé à une vitesse angulaire de la cathode de 0,25 rad/s, présente la plus faible consommation d'énergie (-40%) et la plus faible recombinaison du lithium (-88,6 %). Cette performance s'explique par la suppression du diaphragme et par l'élimination des zones de recirculation proches du fond de l'anode.

L'originalité de ce travail de recherche consiste à simuler pour la première fois les aspects suivants :

1. Le risque de la réaction secondaire entre les gouttes de lithium liquide et les bulles de chlore.
2. Les trois phases présentes dans la cellule électrolytique pour produire du lithium (chlore gazeux, lithium liquide et la solution électrolytique).
3. Le transfert d'ions et de courants au sein de la couche limite formée sur la surface de l'anode, en fonction de la fraction volumique de chlore gazeux et de la hauteur de l'anode.

Le modèle mathématique a comme application industrielle d'identifier les problèmes développés dans la cellule électrolytique qui augmentent la consommation d'énergie et diminuent la production de lithium dans le processus.

5.1.1 Projets proposés

- Nous proposons d'améliorer la fiabilité du modèle en prédisant la génération de noyaux de Cl_2 sur la surface de l'anode sur la base de la théorie classique de la nucléation en utilisant la concentration locale de chlore telle que prédite par la réaction électrochimique.

- Il serait également intéressant d'évaluer la robustesse du modèle en étudiant l'impact de la mise à l'échelle (modèles industriels) et de différentes configurations d'écoulement sur les performances de la cellule.

- De plus, nous proposons d'ajouter une équation de bilan énergétique au modèle. Cette nouvelle fonctionnalité permettrait de représenter les gradients thermiques à l'intérieur de la cellule et leur impact sur le transport de masse et sur les réactions électrochimiques.

- L'amélioration du modèle par l'incorporation d'un maillage mobile à l'interface entre l'électrolyte et les électrodes mobiles serait bénéfique pour mieux capturer le comportement des électrodes en rotation et pour prédire le comportement de la cellule à des vitesses de rotation plus élevées.

- Le diaphragme dans une cellule électrolytique a toujours représenté une résistance au transfert de charge dans la solution d'électrolyte. Les auteurs suggèrent donc de remplacer le diaphragme par une barrière dynamique fluide dans la solution d'électrolyte entre les deux électrodes. La barrière dynamique fluide se formerait avec la vitesse de rotation inverse des électrodes. Elle n'offre pas de résistance supplémentaire au transfert de charge et empêcherait également les gouttes de lithium de passer dans le domaine anodique, empêchant ainsi la recombinaison du lithium avec une quantité minimale d'énergie consommée.

- Enfin, les auteurs ont observé que le transfert de courant le plus élevé se produit à la distance la plus courte entre les deux électrodes, mais que le courant est le plus faible dans les régions les plus éloignées au-dessus de la surface de la cathode. Par conséquent, les auteurs suggèrent un projet pour savoir si les gouttes de lithium formées à la surface de la cathode sont plus petites dans la zone où la densité de courant est plus faible et pour évaluer dans quelle mesure le pourcentage de masse de lithium recombiné serait causé par des gouttes de lithium liquide plus petites. Pour développer ce dernier objectif, il est nécessaire d'utiliser un modèle mathématique basé sur la méthode du bilan massique de population.

5.2 Conclusion in English

Industrial electrolysers designed to produce metals seek new methods and techniques to lower their energy consumption and environmental impact. In the lithium electrolysis, the bubbles represent an operational problem during metal production, due to its resistance effect with regards to mass and charge transfer. Lithium metal can also react back with chlorine gas and return to its ionic state. The simulation of the electrolytic processes has become a privileged way to search and find solutions to the various problems that arise in the metal production, especially for applications where measurements are difficult to obtain. The authors of this research work present a new mathematical model that includes important and original features such as 1- the prediction of Li liquid drop production and its related fluid dynamics, 2- the prediction of Cl_2 bubbles produced on anode surface. It has been used to study the impact of cell design on fluid dynamics and on Li recombination with Cl_2. Simulations were conducted

for a sufficient electrolysis time to reach steady state using a turbulent (k-ε) approach to solve the two-phase flow coupled with the lithium electrolysis process.

The validation of this model for each fields shows that the coupling between mass and momentum transfer is important to understand the recombination of lithium mass and energy consumed in the process. It was used here to show the impact of four cell configurations (diaphragm at 90° with or without bottom baffle, diaphragm at > 90°, diaphragm at < 90°) on cathode fluid dynamics and lithium recombination with Cl_2 in the anode domain. The baffle reduced the amount of recombined lithium by 7 % with no additional energy cost. The diaphragm with an inclination < 90° reduced the total recombined mass by 77 %, although it increased the energy consumption by 10 % with respect to the base case of a vertical diaphragm. This last case illustrates that certain design modifications can lead to a reduction of Li recombination but at a high energy cost. The model can be used to guide industrial producers to optimize their development efforts and to identify parameters that lead to improvement of Capex and Opex.

Comparing the non-porous ungrooved diaphragm with grooved diaphragm design, the latter design reduces the total cell potential by 45 %. However, the recombined lithium mass increased by 4 times when an ungrooved diaphragm is replaced by a grooved design, a quantity that only represents 0.6 % of total lithium mass produced. The specific energy consumption of grooved design leads to a reduction of 26.7 % with respect to the base case of a vertical non-porous diaphragm. The impact of diaphragm inclination toward the anode, a design solution to minimize lithium backreaction, was also assessed. When compared to the vertical grooved diaphragm, the inclined grooved designs show two opposite effects. On one hand, the cell potential increases by 3.7 % and 1.5 % respectively for the 85° and 87° angles. On the other hand, the recombined lithium decreased by 71.3 % and 51.5 % respectively for the same angles. In the end, the energy consumption of the 85° grooved design, having roughly the same lithium recombination than the straight ungrooved diaphragm, leads to a reduction of 23.5 % of the specific energy.

The influence of electrode rotation on the cell fluid dynamics and on its electrochemical performance was also evaluated. Although the anode rotation movement modifies the fluid dynamics of the electrolyte solution, it does not significantly affect the amount of recombined lithium and the energy consumed, partly due to the high viscosity of the electrolyte and to the small anode area. In contrast, the cathode rotation movement can significantly affect the recombination of lithium metal and hence the energy consumed. When compared to straight ungrooved diaphragm and non-rotating electrode configuration, the best rotating cathode case, found at cathode angular velocity of 0.25 rad/s, presents the lowest energy consumption (-40%) and lithium recombination (-88.6 %). This performance can be explained by the removal of the diaphragm and the elimination of recirculation zones close to the bottom of the anode.

The originalities of this research work consist of to simulate for the first time the following aspects:

1. The risk of the secondary reaction between the liquid lithium drops and the chlorine bubbles.
2. The three phases present in the electrolytic cell to produce lithium (chlorine gas, liquid lithium and the electrolytic solution).
3. The transfer of ions and currents within the boundary layer formed on the anode surface, as a function of the volume fraction of chlorine gas and the height of the anode.

The mathematical model has as an industrial application to identify the problems developed within the electrolytic cell that increase the energy consumption and decrease the lithium production in the process.

5.2.1 Proposed projects

- We propose to improve the reliability of the model by predicting the generation of Cl_2 nuclei on the anode surface based on the Classical Nucleation Theory using the local chlorine concentration as predicted by the electrochemical reaction.
- It would also be interesting to assess the robustness of the model by studying the impact of scaleup (industrial designs) and different flow configurations on the performance of the cell.
- Moreover, we propose to add an energy balance equation to the model. This new feature would help to represent the thermal gradients inside the cell and their impact on the mass transport and electrochemical reactions.
- Improvements of the model by incorporating a moving mesh at the interface between the electrolyte and the moving electrodes would be beneficial to better capture the behaviour of the rotating electrodes and to predict the behaviour of the cell at higher rotating speeds.
- The diaphragm in an electrolytic cell has always represented a resistance to charge transfer in the electrolyte solution, so the authors suggest replacing the diaphragm by a fluid dynamic barrier in the electrolyte solution between the two electrodes. The fluid dynamic barrier would be formed with the reverse rotational speed of the electrodes. It does not offer any additional resistance to charge transfer and would also prevent lithium drops passing into the anode domain, thus preventing lithium recombination with the minimal quantity of energy consumed.
- Finally, the authors observed that the highest current transfer occurs at the shortest distance between the two electrodes, but the current is lowest in the farthest regions above the cathode surface. Therefore, the authors suggest a project to know if the lithium drops formed on the surface of the cathode are smaller in the area where the current density is lower and to evaluate how much the percentage of recombined lithium mass

would be caused by smaller liquid lithium drops. To develop the last objective, it is necessary to use a mathematic model based on the method of population mass balance.

- **Nomenclature**
- c Concentration (mol m^{-3})
- D Diffusion coefficient (m^2 s^{-1})
- D_{eff} Effective diffusion coefficient (m^2 s^{-1})
- d Diameter (m)
- F Faraday's constant (A s mol^{-1})
- g Earth gravitational acceleration (m s^{-2})
- i Current density (A m^{-2})
- i_0 Exchange current density (A m^{-2})
- i_m Average current density (A m^{-2})
- k   Turbulent kinetic energy (m^2 s^{-2})
- n   Number of electrons
- N   Mole flux (mol m^{-2} s^{-1})
- R   Gas constant (J mol^{-1} K^{-1})
- R$'$ Production term (mol m^{-3} s^{-1})
- Re Reynolds number
- t Time (s)
- T   Temperature (K)
- um Ions mobility (m^2 s^{-1} V^{-1})
- $u_{g,l}$ Gas and Liquid velocity (m s^{-1})
- x   Mole fraction
- **Greek letters**
- α   Transfer coefficient
- ε Rate of dissipation of kinetic energy (m^2 s^{-3})
- σ Conductivity (S m^{-1})
- ρ   Density (kg m^{-3})
- μ   Viscosity (kg s^{-1} m^{-1})
- γ Surface tension (N m^{-1})
- Φ   Potential field (V)
- $\emptyset_g$ Bubble coverage
- η   Activation overpotential (V)

- **Subscript/ Superscripts**
- An, Ca Anode/ Cathode

- i Species i
- j Species j

6 References

[1] "COP26 declaration on accelerating the transition to 100% zero emission cars and vans.," *UN Climate Change Conference (COP26) at the SEC – Glasgow 2021*, Nov. 10, 2021. https://ukcop26.org/cop26-declaration-on-accelerating-the-transition-to-100-zero-emission-cars-and-vans/ (accessed Nov. 26, 2021).

[2] "The Role of Critical Minerals in Clean Energy Transitions – Analysis," *IEA*, Jul. 06, 2021. https://www.iea.org/reports/the-role-of-critical-minerals-in-clean-energy-transitions (accessed Jul. 05, 2021).

[3] B. Mercier-Guyon, B. Chavillon, E. Mayousse, A. Le Comte, Y. Reynier, and C. Barchasz, "Influence of electrolyte composition on high energy lithium metal cells," *Solid State Ion.*, vol. 350, p. 115321, Jul. 2020, doi: 10.1016/j.ssi.2020.115321.

[4] J. G. Kim *et al.*, "A review of lithium and non-lithium based solid state batteries," *J. Power Sources*, vol. 282, pp. 299–322, May 2015, doi: 10.1016/j.jpowsour.2015.02.054.

[5] T. Placke, R. Kloepsch, S. Dühnen, and M. Winter, "Lithium ion, lithium metal, and alternative rechargeable battery technologies: the odyssey for high energy density," *J. Solid State Electrochem.*, vol. 21, no. 7, Art. no. 7, Jul. 2017, doi: 10.1007/s10008-017-3610-7.

[6] V. St-Onge, M. Cui, S. Rochon, J.-C. Daigle, and J. P. Claverie, "Reducing crystallinity in solid polymer electrolytes for lithium-metal batteries via statistical copolymerization," *Commun. Mater.*, vol. 2, no. 1, pp. 1–11, Aug. 2021, doi: 10.1038/s43246-021-00187-2.

[7] K. Amouzegar and S. Harrison, "Electrolytic Production of Lithium Metal.," Hydro-Quebec, Shawinigan, Quebec, Canada, 1996.

[8] E. Oliaii, M. Désilets, and G. Lantagne, "Numerical analysis of the effect of structural and operational parameters on electric and concentration fields of a lithium electrolysis cell," *J. Appl. Electrochem.*, vol. 47, no. 6, pp. 711–726, Jun. 2017, doi: 10.1007/s10800-017-1073-2.

[9] E. Oliaii, G. Litrico, M. Désilets, and G. Lantagne, "Mass transport and energy consumption inside a lithium electrolysis cell," *Electrochimica Acta*, vol. 290, pp. 390–403, Nov. 2018, doi: 10.1016/j.electacta.2018.09.014.

[10] G. Litrico, E. Oliaii, C. B. Vieira, M. Désilets, and P. Proulx, "Mass Transfer Study inside a Li Production Electrolysis Cell Based on a Rigorous CFD Analysis," *J. Fluid Flow Heat Mass Transf.*, 2018.

[11] K. Zhang *et al.*, "A numerical assessment of bubble-induced electric resistance in aluminium electrolytic cells," *J. Appl. Electrochem.*, vol. 44, no. 10, Art. no. 10, Oct. 2014.

[12] M. Ariana, M. Désilets, and P. Proulx, "On the analysis of ionic mass transfer in the electrolytic bath of an aluminum reduction cell," *Can. J. Chem. Eng.*, vol. 92, no. 11, Art. no. 11, Nov. 2014.

[13] H. Liu, L. Pan, H. Huang, Q. Qin, P. Li, and J. Wen, "Hydrogen bubble growth at micro-electrode under magnetic field," *J. Electroanal. Chem.*, vol. 754, pp. 22–29, Oct. 2015.

[14] J. Haraldsson and M. T. Johansson, "Review of measures for improved energy efficiency in production-related processes in the aluminium industry – From electrolysis to recycling," *Renew. Sustain. Energy Rev.*, vol. 93, pp. 525–548, Oct. 2018.

[15] Q.-W. Zhao, C.-L. Liu, Z. Sun, and J.-G. Yu, "Analysing and optimizing the electrolysis efficiency of a lithium cell based on the electrochemical and multiphase model," *R. Soc. Open Sci.*, vol. 7, no. 1, pp. 191–124, Jan. 2020.

[16] W. A. El-Askary, I. M. Sakr, K. A. Ibrahim, and A. Balabel, "Hydrodynamics characteristics of hydrogen evolution process through electrolysis: Numerical and experimental studies," *Energy*, vol. 90, pp. 722–737, Oct. 2015.

[17] H. Riegel, J. Mitrovic, and K. Stephan, "Role of mass transfer on hydrogen evolution in aqueous media," *J. Appl. Electrochem.*, vol. 28, no. 1, pp. 10–17, Jan. 1998.

[18] K. Takamure, T. Degawa, R. Kano, and T. Uchiyama, "Effect of cylinders on the characteristics of a fine-bubble plume," *J. Fluid Sci. Technol.*, vol. 15, no. 3, pp. 269–280, 2020.

[19] Q. Pan, S. Tore Johansen, J. Erik Olsen, M. Reed, and L. Roar Sætran, "On the turbulence modelling of bubble plumes," *Chem. Eng. Sci.*, p. 116059, Aug. 2020.

[20] T. Siva Sashank, "How to Model Sparging in COMSOL Multiphysics," *COMSOL Multiphysics*, Aug. 22, 2018. https://www.comsol.com/blogs/how-to-model-sparging-in-comsol-multiphysics (accessed Jun. 23, 2021).

[21] J. Schillings, O. Doche, and J. Deseure, "Modeling of electrochemically generated bubbly flow under buoyancy-driven and forced convection," *Int. J. Heat Mass Transf.*, vol. 85, pp. 292–299, Jun. 2015, doi: 10.1016/j.ijheatmasstransfer.2015.01.121.

[22] E. Dickinson, "Theory of Current Distribution," *COMSOL Multiphysics*, Feb. 07, 2014. https://www.comsol.com/blogs/theory-current-distribution/ (accessed Mar. 20, 2019).

[23] D. G. Lovering, Ed., *Molten Salt Technology*. Boston, MA: Springer US, 1982. doi: 10.1007/978-1-4757-1724-2.

[24] K. Zeng and D. Zhang, "Recent progress in alkaline water electrolysis for hydrogen production and applications," *Prog. Energy Combust. Sci.*, vol. 36, no. 3, Art. no. 3, Jun. 2010, doi: 10.1016/j.pecs.2009.11.002.

[25] D. Winter, P. Virnau, and K. Binder, "Monte Carlo Test of the Classical Theory for Heterogeneous Nucleation Barriers," *Phys. Rev. Lett.*, vol. 103, no. 22, Nov. 2010, doi: 10.1103/PhysRevLett.103.225703.

[26] V. I. Kalikmanov, *Nucleation theory*. Dordrecht ; London: Springer, 2013.

[27] M. Horsch, J. Vrabec, and H. Hasse, "Modification of the classical nucleation theory based on molecular simulation data for surface tension, critical nucleus size, and nucleation rate," *Phys. Rev. E*, vol. 78, no. 1, Art. no. 1, Jul. 2008, doi: 10.1103/PhysRevE.78.011603.

[28] D. Kashchiev, "On the relation between nucleation work, nucleus size, and nucleation rate," *J. Chem. Phys.*, vol. 76, no. 10, Art. no. 10, May 1982, doi: 10.1063/1.442808.

[29] H. Vehkamäki, *Classical nucleation theory in multicomponent systems*. Berlin ; New York: Springer, 2006.

[30] P. Van der Linde *et al.*, "Electrolysis-Driven and Pressure-Controlled Diffusive Growth of Successive Bubbles on Microstructured Surfaces," *Langmuir*, vol. 33, no. 45, Art. no. 45, Nov. 2017, doi: 10.1021/acs.langmuir.7b02978.

[31] R. Clift, J. R. Grace, and M. E. Weber, *Bubbles, Drops, and Particles*, Academic Press, INC. 1978, 1978.

[32] R. B. Bird, W. E. Stewart, and E. N. Lightfoot, *Transport Phenomena*, Wiley. Toronto: John Wiley, 2007.

[33] K. B. Oldham, Myland, Jan C., and Bond, Alan M., *Electrochimical Science and Technology*, John Wiley&Sons. Canada: 2013, 2012.

[34] D. Zhang and K. Zeng, "Evaluating the Behavior of Electrolytic Gas Bubbles and Their Effect on the Cell Voltage in Alkaline Water Electrolysis," *Ind. Eng. Chem. Res.*, vol. 51, no. 42, Art. no. 42, Oct. 2012, doi: 10.1021/ie301029e.

[35] C.-L. Liu, Z. Sun, G.-M. Lu, X.-F. Song, and J.-G. Yu, "Experimental and numerical investigation of two-phase flow patterns in magnesium electrolysis cell with non-uniform current density distribution," *Can. J. Chem. Eng.*, vol. 93, no. 3, Art. no. 3, 2015, doi: 10.1002/cjce.22135.

[36] A. Nouri-Khorasani, E. Tabu Ojong, T. Smolinka, and D. P. Wilkinson, "Model of oxygen bubbles and performance impact in the porous transport layer of PEM water electrolysis cells," *Int. J. Hydrog. Energy*, vol. 42, no. 48, Art. no. 48, Nov. 2017, doi: 10.1016/j.ijhydene.2017.09.167.

[37] J. Liu, G. Wang, L. Zhang, Y. Shi, H. Zhang, and S. Yao, "Numerical simulation of single bubble boiling behavior," *Propuls. Power Res.*, vol. 6, no. 2, Art. no. 2, Jun. 2017, doi: 10.1016/j.jppr.2017.05.003.

[38] C. A. Martinez Huitle, M. A. Rodrigo, and O. Scialdone, *Electrochemical Water and Wastewater Treatment*. San Diego, UNITED STATES: Elsevier Science & Technology, 2018. Accessed: Nov. 02, 2018. [Online]. Available: http://ebookcentral.proquest.com/lib/usherbrookemgh-ebooks/detail.action?docID=5406478

[39] E. Mahvelati and P. Proulx, "Development Validation and Application of Population Balance Models in Eulerian Approach for Bubby Flow Reactors.," Thesis, Sherbrooke University, Sherbrooke, Quebec, Canada, 2018.

[40] J. M. Meléndez, M. Désilets, G. Lantagne, and E. Oliaii, "Effect of Bubbles and Liquid Drops Fluid Dynamics on the Lithium Recombination inside a Lithium Electrolytic Cell with Diaphragm," *J. Electrochem. Soc.*, vol. 169, no. 2, p. 026516, Feb. 2022, doi: 10.1149/1945-7111/ac5064.

[41] J. G. Kim *et al.*, "A review of lithium and non-lithium based solid state batteries," *J. Power Sources*, vol. 282, pp. 299–322, May 2015.

[42] S. E. Kesler, P. W. Gruber, P. A. Medina, G. A. Keoleian, M. P. Everson, and T. J. Wallington, "Global lithium resources: Relative importance of pegmatite, brine and other deposits," *Ore Geol. Rev.*, vol. 48, pp. 55–69, Oct. 2012.

[43] D. R. Sadoway, "Toward new technologies for the production of lithium," *JOM*, vol. 50, no. 5, pp. 24–26, May 1998.

[44] M. Ariana, M. Désilets, and P. Proulx, "On the analysis of ionic mass transfer in the electrolytic bath of an aluminum reduction cell," *Can. J. Chem. Eng.*, vol. 92, no. 11, pp. 1951–1964, Nov. 2014, doi: 10.1002/cjce.22047.

[45] J. Haraldsson and M. T. Johansson, "Review of measures for improved energy efficiency in production-related processes in the aluminium industry – From electrolysis to recycling," *Renew. Sustain. Energy Rev.*, vol. 93, pp. 525–548, Oct. 2018, doi: 10.1016/j.rser.2018.05.043.

[46] H. Liu, L. Pan, H. Huang, Q. Qin, P. Li, and J. Wen, "Hydrogen bubble growth at micro-electrode under magnetic field," *J. Electroanal. Chem.*, vol. 754, pp. 22–29, Oct. 2015, doi: 10.1016/j.jelechem.2015.06.015.

[47] K. Zhang *et al.*, "A numerical assessment of bubble-induced electric resistance in aluminium electrolytic cells," *J. Appl. Electrochem.*, vol. 44, no. 10, pp. 1081–1092, Oct. 2014, doi: 10.1007/s10800-014-0721-z.

[48] "How to Model Sparging in COMSOL Multiphysics®," *COMSOL Multiphysics*. https://www.comsol.com/blogs/how-to-model-sparging-in-comsol-multiphysics (accessed Apr. 26, 2020).

[49] S. J., D. O., and D. J. Deseure, "Study of Electrochemically Generated Two-Phase Flows," 2015. https://www.comsol.com/paper/study-of-electrochemically-generated-two-phase-flows-25791 (accessed Jun. 23, 2021).

[50] E. D. E., "Theory of Current Distribution," *COMSOL Multiphysics*, Feb. 07, 2014. https://www.comsol.com/blogs/theory-current-distribution/ (accessed Mar. 20, 2019).

[51] D. G. Lovering, Ed., *Molten Salt Technology*. Boston, MA: Springer US, 1982. doi: 10.1007/978-1-4757-1724-2.

[52] K. B. Oldham, Myland, Jan C., and Bond, Alan M., *Electrochimical Science and Technology*, John Wiley&Sons. Canada: 2013, 2012.

[53] H. Wendt and G. Kreysa, *Electrochemical Engineering*. Berlin, Heidelberg: Springer Berlin Heidelberg, 1999. doi: 10.1007/978-3-662-03851-2.

[54] A. J. Bard and L. R. Faulkner, *Electrochemical methods: fundamentals and applications*, 2nd ed. New York: Wiley, 2001.

[55] A. Tomiyama, H. Tamai, I. Zun, and S. Hosokawa, "Transverse migration of single bubbles in simple shear flows," *Chem. Eng. Sci.*, vol. 57, no. 11, pp. 1849–1858, Jun. 2002, doi: 10.1016/S0009-2509(02)00085-4.

[56] A. Serizawa, T. Fukano, and J. Bataille, Eds., *Multiphase flow 1995*. Amsterdam ; New York: Elsevier Science, 1995.

[57] D. A. Drew and S. L. Passman, *Theory of multicomponent fluids*. New York: Springer, 1999.

[58] J. Murallidharan, G. Giustini, Y. Sato, B. Ničeno, V. Badalassi, and S. P. Walker, "Computational Fluid Dynamic Simulation of Single Bubble Growth under High-Pressure

Pool Boiling Conditions," *Nucl. Eng. Technol.*, vol. 48, no. 4, Art. no. 4, Aug. 2016, doi: 10.1016/j.net.2016.06.004.

[59] A. N. L. Schiller, "A Drag Coefficient Correlation," vol. 77, pp. 318–320, 1935.

[60] M. J. Pang and J. J. Wei, "Analysis of drag and lift coefficient expressions of bubbly flow system for low to medium Reynolds number," *Nucl. Eng. Des.*, vol. 241, no. 6, Art. no. 6, Jun. 2011, doi: 10.1016/j.nucengdes.2011.03.046.

[61] A. Asad, C. Kratzsch, and R. Schwarze, "Influence of drag closures and inlet conditions on bubble dynamics and flow behavior inside a bubble column," *Eng. Appl. Comput. Fluid Mech.*, vol. 11, no. 1, Art. no. 1, Jan. 2017, doi: 10.1080/19942060.2016.1249410.

[62] Å. Ervik and E. Bjørklund, "The transition in settling velocity of surfactant-covered droplets from the Stokes to the Hadamard–Rybczynski solution," *Eur. J. Mech. - BFluids*, vol. 66, pp. 10–19, Nov. 2017, doi: 10.1016/j.euromechflu.2017.05.007.

[63] Y. Nam, E. Aktinol, V. K. Dhir, and Y. S. Ju, "Single bubble dynamics on a superhydrophilic surface with artificial nucleation sites," *Int. J. Heat Mass Transf.*, vol. 54, no. 7, pp. 1572–1577, Mar. 2011, doi: 10.1016/j.ijheatmasstransfer.2010.11.031.

[64] R. L. Smith, H. Inomata, and C. J. Peters, *Introduction to supercritical fluids: a spreadsheet-based approach*. Amsterdam ; Boston: Elsevier, 2013.

[65] J. M. Melendez, M. Desilets, and G. Lantagne, "Reduction of Energy Consumption in Lithium Electrolytic Cell by Improving Design and Operating Conditions," *J. Electrochem. Soc.*, 2022, doi: 10.1149/1945-7111/ac8cb7.

[66] H. Vogt and R. J. Balzer, "The bubble coverage of gas-evolving electrodes in stagnant electrolytes," *Electrochimica Acta*, vol. 50, no. 10, Art. no. 10, Mar. 2005, doi: 10.1016/j.electacta.2004.09.025.

[67] H. Vogt, "The Quantities Affecting the Bubble Coverage of Gas-Evolving Electrodes," *Electrochimica Acta*, vol. 235, pp. 495–499, May 2017, doi: 10.1016/j.electacta.2017.03.116.

[68] H. Vogt, "The incremental ohmic resistance caused by bubbles adhering to an electrode," *J. Appl. Electrochem.*, vol. 13, no. 1, pp. 87–88, Jan. 1983, doi: 10.1007/BF00615891.

[69] D. A. Bograchev and A. D. Davydov, "Estimation of resistance of rotating electrochemical cell associated with gas evolution on the electrode," *Russ. J. Electrochem.*, vol. 45, no. 12, Art. no. 12, Dec. 2009, doi: 10.1134/S1023193509120118.

[70] A. Hartig-Weiss, M. F. Tovini, H. A. Gasteiger, and H. A. El-Sayed, "OER Catalyst Durability Tests Using the Rotating Disk Electrode Technique: The Reason Why This Leads to Erroneous Conclusions," *ACS Appl. Energy Mater.*, Oct. 2020, doi: 10.1021/acsaem.0c01944.

[71] W.-F. Huang and M.-C. Yang, "Electrosynthesis of Adiponitrile with a Rotating Cylindrical Electrode," *Ind. Eng. Chem. Res.*, Aug. 2021, doi: 10.1021/acs.iecr.1c02100.

[72] N. Nippatla and L. Philip, "Performance evaluation of a novel electrolytic reactor with rotating and non rotating bipolar disc electrodes for synthetic textile wastewater treatment," *J. Environ. Chem. Eng.*, vol. 8, no. 2, p. 103462, Apr. 2020, doi: 10.1016/j.jece.2019.103462.